Astronomy Reports, Vol. 45, No. 10, 2001, pp. 751–754. Translated from Astronomicheskiĭ Zhurnal, Vol. 78, No. 10, 2001, pp. 867–870.

The Angular-Momentum Distribution in Axisymmetrical Galaxies

B. P. Kondratyev

Udmurtia State University, Izhevsk, Russia

Received May 15, 2000

Abstract—We investigate the angular-momentum distribution in a classical homogeneous Maclaurin spheroid. An exact formula for the distribution as a function of the mass of a cylindrical column in the spheroid is obtained in both integral and differential forms. This expression is used to calculate the angular-velocity distributions in galaxies evolving from initially spheroidal configurations to steady-state configurations with observed density distributions. © *2001 MAIK "Nauka/Interperiodica".*

1. INTRODUCTION

It is convenient to construct numerical and analytical models for the axisymmetrical figures of equilibrium for gaseous systems and galaxies by specifying the angular momentum $L[M(R)]$ inside the system as a function of the mass enclosed in a cylindrical surface with a specified value of L. This approach is physically more transparent than the frequently used in practice of choosing *a priori* some particular distribution for the angular velocity inside the configuration. Specifying the function $L(R)$ is also justified from the standpoint of evolution. Since $L(R)$ is invariant during the evolution of an isolated, axisymmetrical gravitating system free of turbulence and viscosity, the angular-momentum distributions observed in galaxies can also shed light on the dynamical states of protogalaxies. We note in this connection the study of Crampin and Houle [1], who concluded that the distributions of the specific angular momentum for eight flat galaxies derived from their rotation curves coincided with the specific momentum $l[M(R)]$ for a classical, homogeneous Maclaurin spheroid to within 1% (see also [2]). These results were subsequently confirmed [3].

In his detailed review [4], Antonov notes that many authors adopt as the initial state a Maclaurin ellipsoid, for which

$$l[M(R)] = \frac{5}{2}\frac{L_t}{M_t}\left[1-\left(1-\frac{M}{M_t}\right)^{2/3}\right]. \quad (1)$$

Here, $l[M(R)]$ and $M(R)$ have the same meaning as above, and L_t and M_t are the total momentum and mass of the configuration. Formula (1) is widely known; in addition to the review [4], it is referenced, for instance, in the well-known study by Tassoul [5].

Here, we first derive the formula for the mean distribution of the angular momentum in a classical Maclaurin spheroid (Section 2); in Section 3, the proposed technique is used to calculate the angular-velocity distributions in galaxies with real density distributions. The method of comparing angular momenta is efficient and simple, but has remained little used until now.

2. THE FUNCTION $L[M(R)]$ FOR A MACLAURIN SPHEROID

Let us consider in cylindrical coordinates $R = \sqrt{x^2+y^2}$ and z a homogeneous spheroid with density ρ, semi-axes $a_1 \geq a_3$, and the surface equation

$$\frac{R^2}{a_1^2}+\frac{z^2}{a_3^2}=1. \quad (2)$$

Let a cylindrical surface with radius R separate the volume $V(R)$ in the spheroid (Fig. 1). This volume corresponds to the shaded area in Fig. 1, and is equal to

$$V(R)=\frac{4}{3}\pi a_1^2 a_3\left[1-\left(1-\frac{R^2}{a_1^2}\right)^{3/2}\right]=V_t(1-x^3), \quad (3)$$

where

$$x=\frac{H}{a_3}=\sqrt{1-\frac{R^2}{a_1^2}}, \quad V_t=\frac{4}{3}\pi a_1^2 a_3. \quad (4)$$

Obviously, $0 \leq x \leq 1$. It follows from (3) that the mass of the shaded fraction of the spheroid

$$M(R)=M_t(1-x^3). \quad (5)$$

Further, the rotational momentum of a configuration with a solid-body rotation and angular velocity Ω is

$$L=\Omega I_z; \quad (6)$$

1063-7729/01/4510-0751$21.00

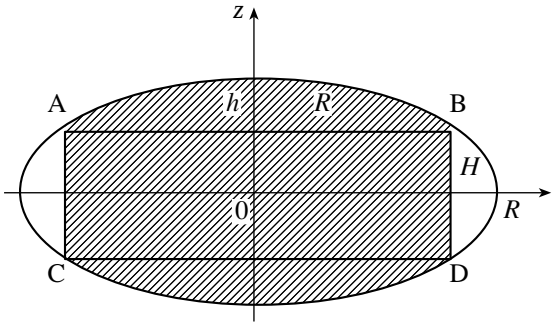

Fig. 1. Oblate spheroid. The shaded cylindrical area consists of the cylinder ABCD with radius R and two spheroidal segments with height h.

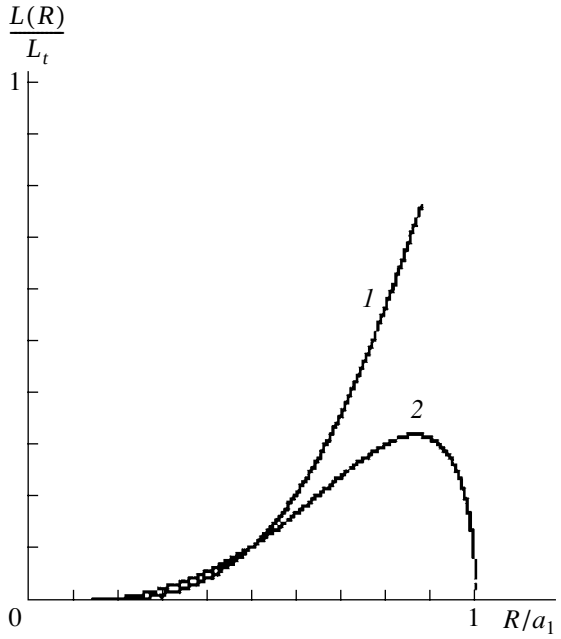

Fig. 2. Angular momentum distribution in a Maclaurin spheroid as a function of R/a_1: curve *1* shows the function $L(R)/L_t$ according to (13), and curve *2* shows the distribution of the specific angular momentum according to (19), $\frac{2}{15}\frac{a_1}{L_t}l(R) = \left(\frac{R}{a_1}\right)^3\sqrt{1-\left(\frac{R}{a_1}\right)^2}$.

where

$$I_z = \iiint_V \rho R^2 dV \tag{7}$$

is the moment of inertia about the axis of rotation Oz. In our case, $\rho = \text{const}$, and the configuration under consideration consists of a cylinder with height $2H$ and two spheroidal segments (Fig. 1). The total moment of inertia of the delineated part of the spheroid I_z is essentially the sum of the moments of inertia of the cylinder and two segments:

$$I_z = I_{\text{cyl}} + 2I_{\text{seg}}. \tag{8}$$

It is apparent that

$$I_{\text{cyl}} = \frac{1}{2}M_{\text{cyl}}R^2 = \pi\rho R^4 H = \pi\rho R^4 a_3 x. \tag{9}$$

The moment of inertia for a spheroidal segment is

$$I_{\text{seg}} = \frac{1}{2}\pi\rho\int_H^{a_3} R^4 dz = \frac{\pi}{2}\rho a_1^4 a_3\int_x^1 (1-x^2)^2 dx. \tag{10}$$

We can easily calculate the integral in (10):

$$I_{\text{seg}} = \frac{\pi}{2}\rho a_1^4 a_3\left[\frac{8}{15} - x + \frac{2}{3}x^3 - \frac{1}{5}x^5\right], \tag{11}$$

where x is determined from (4).[1]

Thus, the moment of inertia for the entire delineated part of the homogeneous spheroid is

$$I(R) = \frac{4}{15}\pi\rho a_1^4 a_3\left(2 - 5x^3 + 3x^5\right) = I_t\left(1 - \frac{5}{2}x^3 + \frac{3}{2}x^5\right), \tag{12}$$

where I_t is the total moment of inertia of the spheroid.

Eliminating x from (12) using (5) and taking into account (6), we obtain the desired formula for the angular-momentum distribution in a Maclaurin spheroid

$$L(R) = L_t\left\{1 - \frac{5}{2}\left(1 - \frac{M(R)}{M_t}\right) + \frac{3}{2}\left(1 - \frac{M(R)}{M_t}\right)^{5/3}\right\}, \tag{13}$$

shown graphically in Fig. 2.

3. APPLICATION TO A STRATIFIED INHOMOGENEOUS GALAXY

We will compare two models of galaxies: an initial model A, which is less oblate and close to a Maclaurin spheroid (this model is also considered in [1]), and a final model B, which is essentially inhomogeneous and consistent with observations. The latter model displays barotropic differential rotation. As the galaxy evolves, each element conserves its angular momentum, and there is no mixing of elements with

[1] In the particular case $x = 0$ (half a spheroid), we obtain $I_z = \frac{2}{5}ma_1^2$; besides, (11) yields for the case of a spherical segment $a_1 = a_1 = r$

$$I_{\text{seg}} = \frac{mh}{10}\frac{20r^2 - 15hr + 3h^2}{3r - h},$$

where h is the height of the segment and $m = \pi\rho h^2\left(R - \frac{h}{3}\right)$ is its mass. The moment of inertia for a spherical segment given on p. 69 of the handbook is underestimated by a factor of two.

different momenta. The essence of the problem is that, in this case, the two models will have virtually the same dependence $L[M(R)]$.

Let us consider the specific case when, in the course of evolution, a protogalaxy is transformed into a stratified, inhomogeneous spheroid with a barotropic rotation law $\Omega = \Omega(R)$ and with the density distribution

$$\rho = \rho(m). \tag{14}$$

For E galaxies, the density can be well approximated by the law

$$\rho = \frac{\rho_0}{(1+\beta m^2)^{3/2}}, \tag{15}$$

where the constant β is determined by comparison with photometric data. In the general case, the surfaces of constant density will form a family of spheroidal surfaces with various degree of oblateness:

$$R^2 + \frac{z^2}{1-e^2(m)} = m^2 a_1^2, \quad 0 \le m \le 1. \tag{16}$$

As noted above, it is important that the angular-momentum distribution (13), which for the sake of brevity can be written in the form

$$L(R) = L_t\left(1 - \frac{5}{2}q + \frac{3}{2}q^{5/3}\right), \quad q = x^3, \tag{17}$$

will be invariant in the course of evolution. Under these completely reasonable assumptions, we can derive the function $\Omega(R)$ specifying the rotation in the final model of the galaxy. To this end, we will delineate an elementary cylindrical envelope with radius $R_0 = a_1 m_0$ and unit thickness inside the spheroid (Fig. 3).

Using the mathematical technique developed in [7], we can derive the angular momentum for the envelope:

$$l(R_0) = \left[\frac{dL(R)}{dR}\right]_{R=R_0} = \frac{dL(m_0)}{a_1 dm_0}. \tag{18}$$

Substituting (17) into this expression, we obtain after transformations

$$l(m_0) = 10\pi a_1^2 m_0 \frac{L_t}{M_t}\left(1 - q^{2/3}\right)\Phi(m_0), \tag{19}$$

where

$$\Phi(m_0) = \int\limits_{m_0}^{1} dm\rho(m)\frac{d}{dm}\left[\sqrt{1-e^2(m)}\sqrt{m^2-m_0^2}\right] \tag{20}$$

and

$$q = 1 - \frac{M(R)}{M_t} \tag{21}$$

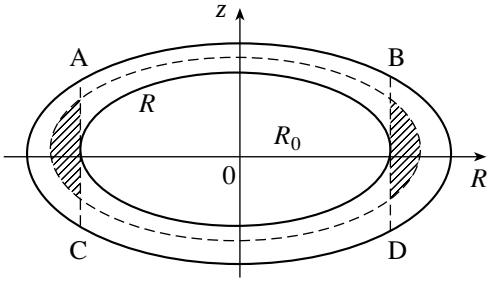

Fig. 3. A stratified inhomogeneous spheroid. ABCD is the delineated cylindrical volume of radius R_0. The torus cross section is shaded.

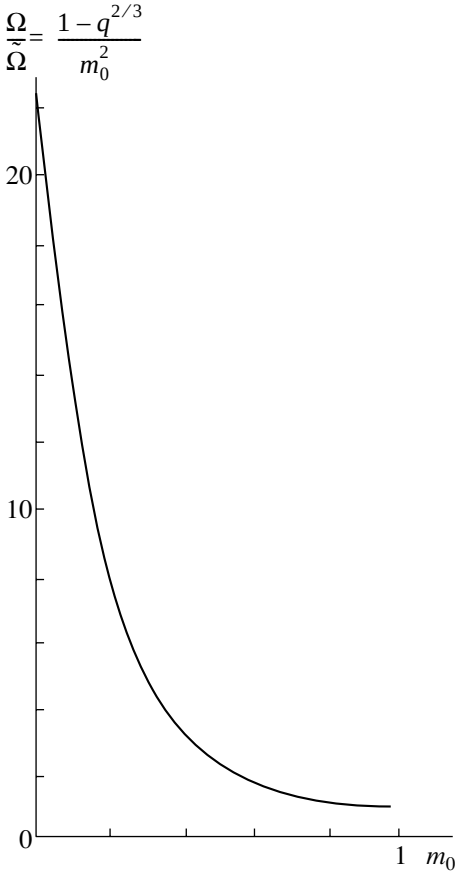

Fig. 4. Distribution of relative angular velocity inside an inhomogeneous spheroidal galaxy, calculated according to (23), $\beta = 150$.

$$= \frac{\int\limits_{m_0}^{1} dm\rho(m)\frac{d}{dm}\left[\sqrt{1-e^2(m)}\left(m^2-m_0^2\right)^{3/2}\right]}{\int\limits_{0}^{1} dm\rho(m)\frac{d}{dm}\left[m^3\sqrt{1-e^2(m)}\right]}.$$

On the other hand, for the same elementary cylindrical envelope, assuming barotropic rotation in the galaxy, direct calculation yields the specific angular

momentum

$$l(m_0) = 4\pi a_1^4 m_0^3 \Omega(R_0)\, \Phi(m_0). \qquad (22)$$

Comparing (22) and (19) yields the desired expression for the angular velocity:

$$\Omega(m_0) = \widetilde{\Omega}\, \frac{1 - q^{2/3}}{m_0^2}, \qquad (23)$$

where the coefficient

$$\widetilde{\Omega} = \frac{5}{2} \frac{L_t}{M_t a_1^2} \qquad (24)$$

can be represented by the series

$$\widetilde{\Omega} = \Omega_{MC}\,[e(1)] + \delta\Omega + ..., \qquad (25)$$

whose first term

$$\frac{\Omega_{MC}^2}{\pi G\rho} = \frac{2\sqrt{1-e^2}}{e^3}\left(3 - 2e^2\right) \arcsin e - \frac{6}{e^2}\left(1 - e^2\right) \qquad (26)$$

corresponds to a classical Maclaurin spheroid. Further corrections in (25) can be derived iteratively.

Figure 4 presents the angular velocity calculated using formula (23), together with real values for the density distributions in galaxies.

4. CONCLUSION

In essence, we present here a criterion for assumed paths of galactic evolution. The method employed yields formula (23) for the angular velocity in the final model for a galaxy; the coefficient in the formula can be represented in the form of a series whose first term is the well known value for the angular velocity in a Maclaurin spheroid. This formula is new and convenient to use. The calculations are in good agreement with observations of rotational motions in galaxies. Note also that, according to our calculations, the square of the angular velocity in the center of the model increases by a factor of 518, whereas the density increases by a factor of 1855. Therefore, Maclaurin modeling of the momentum distributions in galaxies satisfies Poincaré's criterion $\Omega^2 \leq 2\pi G\overline{\rho}$. This circumstance is essential from the viewpoint of the stability of galactic systems.

ACKNOWLEDGMENTS

The author thanks G.S. Bisnovaty-Kogan for useful comments.

REFERENCES

1. D. J. Crampin and F. Houle, Astrophys. J. **40**, 99 (1964).
2. B. A. Vorontsov-Vel'yaminov, *Extragalactic Astronomy* [in Russian] (Nauka, Moscow, 1978).
3. L. M. Ozernoĭ, Astron. Tsirk., No. 407 (1967).
4. V. A. Antonov, in *Kinematics and Dynamics of Stellar Systems* [in Russian] (VINITI, Moscow, 1968).
5. J.-L. Tassoul, *Theory of Rotating Stars* (Princeton Univ. Press, Princeton, 1979; Mir, Moscow, 1982).
6. B. M. Yavorskiĭ and A. A. Detlaf, *Handbook of Physics* [in Russian] (GIFML, Moscow, 1963).
7. B. P. Kondratyev, *Dynamics of Ellipsoidal Gravitating Figures* [in Russian] (Nauka, Moscow, 1989).

Translated by K. Maslennikov

Astronomy Reports, Vol. 45, No. 10, 2001, pp. 755–758. Translated from Astronomicheskiĭ Zhurnal, Vol. 78, No. 10, 2001, pp. 871–875.

An Active Galactic Nucleus as a Massive Coaxial Pulsar: A Massive Central Object with a Keplerian Accretion Disk and Twisted MHD Jet

Ya. N. Istomin[1] and B. V. Komberg[2]

[1]*Lebedev Physical Institute, Leninskiĭ pr. 53, Moscow, 117924 Russia*
[2]*Astro Space Center, Lebedev Physical Institute, ul. Profsoyuznaya 84/152, Moscow, 117810 Russia*
Received December 13, 2000

Abstract—The similarities in certain empirical relations derived for active galactic nuclei (AGN) and radio pulsars support the idea that the energy release in the jets of AGN is electrodynamical, associated with the presence of a massive central object (MCO) and circumnuclear, magnetized Keplerian disk. For example, in both types of object, the radio luminosities are proportional to characteristic time scales—for precession for AGN or rotation for pulsars—to the 0.8 power. In this approach to studying the nature of the activity, the $\dot{P}-P$ relation for pulsars can be considered analogous to the $P_{\rm r}-M_{\rm MCO}$ relation for AGN, which has the form $\log P_{5\rm GHz}(\rm W/Hz) = 2.73\log(M_{\rm MCO}/M_\odot) - 2.87$. © *2001 MAIK "Nauka/Interperiodica".*

1. INTRODUCTION

Recently, massive central objects (MCOs) with masses from 10^6 to $3\times10^{10}M_\odot$ have been found in many nearby galaxies (see, for example, [1–3]). It is interesting that there is a relationship between $M_{\rm MCO}$ and the luminosity of the bulge of the host galaxy ($M_B^{\rm bulge}$) [2, 4, 5]:

$$\log(\frac{M_{\rm MCO}}{M_\odot}) = -0.44M_B^{\rm bulge} - 0.75.$$

Massive, rotating, circumnuclear disks are observed in some of these objects (see, for example [6–8]), whose luminosities in the soft X-ray and ultraviolet (the region of the so-called big blue bump) are correlated with the radio luminosities of the central compact radio sources associated with the galaxies (see, for example, [7, 9–11]). Both AGN (quasars and Seyfert galaxies) and peculiar, galactic stellar binaries with radio jets (such as SS 433 and GRS 1915+105), which are variable X-ray sources, all lie along a single dependence. This may provide evidence that a single mechanism is responsible for the generation of the relativistic particles that radiate in the magnetic fields of these objects.

2. A JET MODEL BASED ON ELECTROMAGNETIC FORCES

The idea expressed in [12] that it is possible to extract energy and rotational momentum from a Kerr black hole via an external electromagnetic field was further developed in [13–16]. These studies indicate that a strong longitudinal electrical field can arise in the gap near the surface at which the Goldreich–Julian volume charge density is zero ($\rho_{GJ}=0$), where there is e^+e^- pair production. This field can accelerate charged particles to hundreds or thousands of MeV, which is sufficient, in the presence of scattering of e^+e^- on background photons, for the development of cascades, not unlike the situation in pulsars (although AGN, in contrast to pulsars, are coaxial rotators). In this view of the central engines of AGN, a jet from an active galactic nucleus can be described as a formation made up of two components:

(1) An inner, near-axial, light flow of charged particles (most likely e^+e^-) generated in the gap near $r_{\rm g}$. The flow of energy in this wind is determined by the electromagnetic Poynting vector. Out to $R\simeq 1000r_{\rm g}$, all processes can be described using a force-free electrodynamical approach.

(2) An external sheath made up of a heavy wind of electrons and ions from the disk, described using dissipation-free magnetic hydrodynamics—a cylindrical jet with a longitudinal magnetic field (B_z). The rotation of the MCO + massive circumnuclear disk system is transferred to the jet via magnetic coupling, leading to the development of a strong radial electrical field ($E_{\rm r}$). The charged particles are wound up in these crossed fields ($E_{\rm r}+B_z$) during their drift motions, creating a current I_z, which, in turn, generates a

1063-7729/01/4510-0755$21.00

field B_φ, which winds the magnetic force lines into a spiral. The step of the spiral will depend on how close to the MCO the cylindrical wind flow forms: the closer this is, the more tightly wound the spiral will be, since the Keplerian velocity of the disk at this distance will be higher. Estimates indicate that such a central relativistic flow surrounded by a heavy rotating sheath is stable to axially symmetric perturbations arising in the disk and can move through a region of cooler and denser plasma without being disrupted.

In this type of model for the jets of AGN, the energy is transported along the jet by the Poynting vector ($\sim E_\mathrm{r} B_\varphi$), over the whole length of the jet (as in a conductor with current). In other objects, the energy could be transported by accelerated particles. In contrast to the situation in pulsars, there is no concept of a light cylinder for charged particles emitting synchrotron radiation in a helical jet magnetic field. From this point of view, different types of AGN could differ from each other not only in the orientations of their jets relative to the line of sight (unification schemes [17, 18]), but also via evolution [19, 20], as a consequence of a decrease in their power and an increase in the dimensions of the cylindrical flow (which means a decrease in the jet rotation speed and in the winding-up of its field lines). It may be that differences in the properties of the central compact radio sources in quasars (a relatively loose field winding in a jet with a larger diameter) and BL Lace objects (tighter field winding in a jet with a smaller diameter) may be at least partially associated with this effect. The jets in the central radio sources of radio galaxies and Seyfert galaxies should have larger diameters than those of quasars, since, according to [20], these objects are later evolutionary stages of radio-loud and radio-quiet quasars. With the increase in angular resolution provided by future space radio interferometry observations, it will be possible to test whether there are differences in the transverse sizes of the radio jets of different types of AGN. Currently, most of the observed radio jets (less than several parsecs in size) are unresolved in the transverse direction (see, for example, [21]).

3. ARGUMENTS IN SUPPORT OF A SIMILARITY IN THE PROCESSES ACCELERATING CHARGED PARTICLES IN AGN AND RADIO PULSARS

It would be useful to try to confirm the above concepts about AGN using observational relations for objects in which the radio emission is clearly associated with the electromagnetic acceleration of charged particles. This is true, first and foremost, of radio pulsars. Indeed, as a rule, estimates of the radio luminosities of radio pulsars (L_r) are based on the idea that the energy losses by the rotating neutron star have a magnetic dipole character:

$$\frac{dE}{dt} = I\Omega\dot{\Omega} = L_\mathrm{mag.dip.} = \delta\frac{B^2\Omega^4R^6}{c^3}. \qquad (1)$$

Here, Ω is the angular speed of rotation of the neutron star, R is its radius, and the parameter $\delta \approx 1$. For AGN, we can take R to be the radius of the radio jet and Ω to be the angular speed of Keplerian rotation of the accretion disk: $\Omega = 2\pi/P_\mathrm{Kepl}$, $P_\mathrm{Kepl} = 2\pi R^{3/2}/(GM_\mathrm{MCO})^{1/2}$. After this, we can rewrite (1) in the form

$$L_\mathrm{mag.dip.} = \frac{G^2}{c^3}(B^2M_\mathrm{MCO}^2). \qquad (1a)$$

It is easy to see that, substituting in (1a) quantities characteristic of AGN ($M_\mathrm{MCO} = 3\times10^8 M_\odot$, $B \approx 10^4$ G), [1] $L_\mathrm{mag.dip.} \approx 10^{46}$ erg/s, which is quite appropriate for AGN. A similar mechanism was used in [23] to estimate the energy losses of a supermassive magnetized disk.

Using previously published dependences for AGN, we can derive a relation between the radio luminosities of the compact nuclear sources and the characteristic time scales for variation in the directions of the radio jets. These time scales were estimated in [24] in the framework of a disk-driven precession model [25] based on the observed spatial steps of spiral-like VLBI radio structures (on scales to tens of parsecs). According to [24], we have

$$\log\Delta t(\mathrm{years}) = 0.49M_\mathrm{abs} + 17.11, \qquad (2)$$

where the absolute magnitudes M_abs of the nuclei of radio-loud objects lie in the range from -21.5 to -27.6. On the other hand, a relation between $P_\mathrm{8.4GHz}$ (W/Hz) and M_v was derived for the nuclei of Seyfert galaxies and radio-quiet quasars in [26]:

$$\log P^\mathrm{N}_\mathrm{8.4GHz}(\mathrm{W/Hz}) = -0.4M_v + 12.9. \qquad (3)$$

Combining (2) and (3), we obtain

$$\log P^\mathrm{N}_\mathrm{8.4GHz}(\mathrm{W/Hz}) = -0.8\log\Delta t(\mathrm{years}) + 26.6, \qquad (4)$$

i.e., $P^\mathrm{N}_{\mathrm{8.4GHz}(W/Hz)} \sim (\Delta t(\mathrm{years}))^{-0.8}$.

It is interesting that a similar relation was obtained for radio pulsars in [27]: $L_\mathrm{radio}(\mathrm{erg/s}) \sim P_s^{-(0.74\text{–}0.94)}$ (although the radio luminosity scales and time scales

[1] We can estimate the magnetic field B generated in the disk near the event horizon of the black hole (r_g) by assuming equipartition of energy between the magnetic field and the disk material: $\dot{m} = (B^2/8\pi)(r_\mathrm{g}^2/c)$. For critical accretion $\dot{m} = \dot{m}_\mathrm{cr} = 10^{17}(M_\mathrm{MCO}/M_\odot)$ g/s, we can write $B = 5\times10^8/\sqrt{M_\mathrm{MCO}/M_\odot}$ G. A more accurate estimate of the magnetic field in the vicinity of a black hole was obtained in [22].

for AGN and pulsars differ by a factor of more than 10^{10-13}).

In theoretical concepts about the mechanism for the radio emission of pulsars and evolutionary variations in pulsars, a large role is played by the position of a pulsar in the $\dot{P}-P$, in which we can draw lines corresponding to specific magnetic-field values for the case of magnetic-dipole radiation:

$$B = \left(\frac{3Ic^3P\dot{P}}{8\pi^2R_{\rm n.s.}^6}\right)^{1/2},$$

where I is the moment of inertia of the neutron star (see, for example, [28]). A death line for radio pulsars emitting magnetic dipole radiation can also be drawn in this diagram: $\log\dot{P} \approx 3\log P - 17$. We can ask whether it is possible to construct an analogous diagram for AGN in our model, in which the energy radiated in the radio jet is ultimately provided by the energy of rotation of a magnetized circumnuclear disk.

It is more or less clear that in the framework of our model we can use the energy released by the AGN nucleus in the radio range ($P^{\rm N}_{\rm 5GHz}$), for example in place of $\dot{P}$. The question is what quantity we should take in place of the unknown characteristic time scale (Δt) in order to construct a $\dot{P}-P$ relation for AGN. To answer this question, we use the results of the very important study [4], in which an observational relation is derived for AGN between the 5 GHz radio power of the central radio source and $M_{\rm MCO}$:

$$\log P^{\rm N}_{\rm 5GHz}({\rm W/Hz}) = 2.73\log\frac{M_{\rm MCO}}{M_\odot} - 2.87. \quad (5)$$

Combining this relation[2] with (4), we can write:

$$\log\Delta t({\rm years}) = -3.4\log\frac{M_{\rm MCO}}{M_\odot} + 37 \quad (6a)$$

or

$$\log\frac{M_{\rm MCO}}{M_\odot} = 0.3\log\Delta t({\rm years}) + 10.9. \quad (6b)$$

It follows that for AGN we can use the mass of the massive central object $M_{\rm MCO}$ in place of the characteristic time scale for precession of the radio jet (Δt from (2)). This means that relation (5) from [4] can be considered analogous to the $\dot{P}-P$ diagram for radio pulsars.

To test our hypotheses, it is desirable to derive relation (5), which was obtained from observational data, directly from the assumptions of [14]. Since this model assumes that the energy release in the jets of AGN has an electromagnetic nature, we can write the following expression for the flux of electromagnetic energy for a jet with radius r_j with a field B_φ:

$$S = \frac{c}{4\pi}E_{\rm r}B_\varphi s,$$

where $E_{\rm r} = (\Omega r/c)B_\varphi$, $s = 4\pi r_j^2$, $B_\varphi = B_{\rm g}(r_{\rm g}/r_j)$, and $r_{\rm g} = 2GM_{\rm MCO}/c^2$. It follows that $S = B_{\rm g}^2\Omega r_j r_{\rm g}^2$, and using the relation $\Omega_{\rm Kepl.} = (GM)^{1/2}/r_j^{3/2}$ we obtain

$$S = B_{\rm g}^2 r_{\rm g}^{7/3}c^{2/3}\Omega^{1/3} \sim B_{\rm g}^2M_{\rm MCO}^{7/3}\Omega^{1/3}. \quad (7)$$

Assuming that Ω is related to Δt by the simple expression $\Omega = 2\pi/\Delta t$ and adopting $B_{\rm g} \approx B \sim M_{\rm MCO}^{-1/2}$ in accordance with (1a) and $\Omega \sim M_{\rm MCO}^{3.4}$ in accordance with (6a), we obtain from (7): $S \sim M_{\rm MCO}^{2.5}$. This theoretical relationship is not very different from the observed dependence $P^{\rm N}_{\rm 5GHz} \sim M_{\rm MCO}^{2.7}$ (5) derived in [4] or the relationship $P^{\rm N}_{\rm 5GHz} \sim M_{\rm MCO}^{2.2}$ obtained in [5].

In conclusion, we would like to consider certain very interesting results obtained in connection with analyses of the optical variability of some AGN over several decades (see, for example, [30] and references therein). Belokon *et al.* [30] point out the following properties of the light curves of objects such as OJ 287, 3C 273, 3C 345, 3C 390.3, PKS 0735+178, ON 231, and W Com:

(1) At least two characteristic time scales (quasi-periods) can be traced: hundreds of days (or years) and decades.

(2) The amplitude of the slow variations is proportional to that of the rapid variations.

(3) For a given object with a characteristic time scale, the shape of its impulses has two or more humps and is repeated.

(4) There is a significant anti-correlation between the characteristic time scale for repeating of an impulse and its width.

It is striking that points (3) and (4) resemble the situation with radio pulsars, with the only difference being that the temporal processes in the light curves of AGN are drawn out relative to those in pulsars by a factor of $\sim (M_{\rm MCO}/M_\odot) \sim 10^8$ and the energy-release processes are enhanced by a factor of $(M_{\rm MCO}/M_\odot)^2 \sim 10^{16}$.

Note also that Kardashev [31] pointed out the similarity between AGN and radio pulsars in connection with their very high brightness temperatures ($T_{\rm b}$), which exceed the value $T_{\rm b,\,crit} \simeq 10^{12}$ K determined by the inverse-Compton limit by many orders of magnitude. Such high values of $T_{\rm b}$ can be achieved under a number of conditions (non-stationarity of the

[2]Note that according to [29] relation (5), which was constructed from data for a large number of objects, is maintained, on average, only for galaxies that are not too powerful in the radio.

source, coherent radiation, Doppler boosting), including the possible presence of appreciable numbers of relativistic protons in the jets of AGN. In this case, $T_b \sim (m_p/m_e)^{9/7}$, and the brightness temperature can reach values $\sim 10^{16}(B_\perp(\mathrm{G}))^{-1/7}$.

4. CONCLUSION

The question of the energy-release mechanism in AGN and in peculiar stellar systems where we observe collimated radiation over a wide range of wavelengths from jets on scales from tens of astronomical units to tens of kiloparsecs is an important astrophysical problem. We suggest that this problem can be solved using a unified magnetohydrodynamical approach. This requires the presence of a gravitating center and a magnetized, rotating accretion disk. In the case of Keplerian rotation of the disk, the magnetic force lines will be wound in the azimuthal direction, facilitating the transfer of angular momentum from the disk and enhancing the accretion rate $\dot{m}_{\mathrm{acc}}$ from the gravitating center. In addition, plasma is accelerated in the axial direction by the Poynting vector, leading to the formation of an axially symmetric relativistic jet.

ACKNOWLEDGMENTS

The authors would like to thank their colleagues in the theoretical department of the Astro Space Center and N.S. Kardashev for useful discussions. B.V. Komberg thanks I.D. Novikov for the possibility of visiting the Theoretical Astronomical Center in Copenhagen, and the possibility to work on this paper. This work was partially supported by the Federal Science and Technology project "Astronomy. Cosmic Microphysics." The study was also supported in part by the Russian Foundation for Basic Research (project no. 99-02-17184).

REFERENCES

1. E. Eckart and R. Genzel, Mon. Not. R. Astron. Soc. **284**, 576 (1997).
2. L. C. Ho, Preprint No. 4678, Harvard-Smithsonian Center for Astrophysics (1998).
3. J. Magorrian and S. Tremaine, Mon. Not. R. Astron. Soc. **309**, 447 (1999).
4. A. Francsehini, S. Vercellone, and A. C. Fabion, Mon. Not. R. Astron. Soc. **297**, 817 (1998).
5. P. Salucci, E. Szuszkiewicz, P. Monaco, and L. Danese, Mon. Not. R. Astron. Soc. **307**, 637 (1999).
6. M. Miyoshi, J. Moran, J. Herrnstein, *et al.,* Nature **373**, 127 (1995).
7. P. P. van der Marel and F. C. Van den Bosch, Preprint No. 1277, Space Tel. Science Inst. (1998).
8. T. Storchi-Bergmann, astro-ph/9903074 (2000).
9. H. Falcke and P. L. Biermann, Astron. Astrophys. **293**, 665 (1995); **308**, 321 (1994).
10. G. Pugliese, H. Falcke, and P. L. Biermann, Astron. Astrophys. **344**, L37 (1999).
11. L. M. Ozernoy, A. M. Fridman, and P. L. Biermann, Astron. Astrophys. **337**, 105 (1998).
12. C. A. Jackson and J. V. Wall, Mon. Not. R. Astron. Soc. **304**, 160 (1999).
13. V. S. Beskin, Ya. N. Istomin, and V. I. Par'ev, Astron. Zh. **69**, 1258 (1992) [Sov. Astron. **36**, 642 (1992)].
14. Ya. N. Istomin and V. I. Pariev, Mon. Not. R. Astron. Soc. **267**, 629 (1994); **281**, 1 (1996).
15. M. Livio, G. I. Ogilvie, and J. E. Pringle, Astrophys. J. **512**, 100 (1999).
16. S. Koide, D. L. Meier, K. Shibata, and T. Kudoh, Astrophys. J. Lett. **495**, L63 (1998); **536**, 668 (2000).
17. M. J. L. Orr and I. W. H. Browne, Mon. Not. R. Astron. Soc. **200**, 1067 (1982).
18. C. M. Urry and P. Padovani, Publ. Astron. Soc. Pac. **107**, 803 (1995).
19. B. V. Komberg, Astron. Zh. **72**, 3 (1995) [Astron. Rep. **39**, 1 (1995)].
20. D. Dultzin-Hacyan, Y. Krongold, I. Fuentos-Guridi, and P. Marziani, Astrophys. J. Lett. **513**, L111 (1999).
21. K. I. Kellermann, Preprint No. 45, NRAO (1999).
22. G. S. Bisnovatyi-Kogan and A. A. Ruzmaikin, Astrophys. Space Sci. **42**, 375 (1976).
23. G. S. Bisnovatyi-Kogan and S. I. Blinnikov, Astrophys. Space Sci. **19**, 93 (1972).
24. J. F. Lu, Astron. Astrophys. **229**, 424 (1990).
25. C. L. Sarazin, M. C. Begelman, and S. P. Hafchett, Astrophys. J. Lett. **238**, L129 (1980).
26. M. J. Kukula, J. S. Dunlop, D. H. Hughes, and S. Rawlinys, Mon. Not. R. Astron. Soc. **297**, 366 (1998).
27. I. F. Malov and V. M. Malofeev, Astron. Zh. **71**, 762 (1994) [Astron. Rep. **38**, 677 (1994)].
28. B. Zhang, A. K. Harding, and A. G. Muslimov, Astrophys. J. Lett. **531**, L135 (2000).
29. A. Laor, astro-ph/0009192.
30. E. T. Belokon, M. K. Babadzhanyants, and J. T. Pollock, Astron. Astrophys. **356**, L21 (2000).
31. N. S. Kardashev, Preprint No. 27, FIAN (Lebedev Institute of Physics, Russian Academy of Sciences, 1999); Mon. Not. R. Astron. Soc. **276**, 515 (1995).

Translated by D. Gabuzda

Astronomy Reports, Vol. 45, No. 10, 2001, pp. 759–768. Translated from Astronomicheskiĭ Zhurnal, Vol. 78, No. 10, 2001, pp. 876–886.

Image Reconstruction for the Einstein Cross Gravitational Lens QSO 2237+0305

V. A. Belokurov[1], E. V. Shimanovskaya[2], M. V. Sazhin[1], A. G. Yagola[2], B. P. Artamonov[1], V. N. Shalyapin[3], and I. Khamitov[4]

[1]*Sternberg Astronomical Institute, Universitetskiĭ pr. 13, Moscow, 119899 Russia*
[2]*Moscow State University, Moscow, Russia*
[3]*Radio Astronomy Institute, Kharkov, Ukraine*
[4]*Ouloug-Beg Astronomical Institute, Tashkent, Uzbekistan*

Received November 22, 1999

Abstract—An image-reconstruction algorithm developed by a group of Belgian scientists based on the regularization method of Tikhonov is studied and applied to images of the gravitational lens QSO 2237+0305 obtained during long-term observations using the 1.5-m telescope at the Maĭdanak Observatory. The algorithm separates the observed image into two parts: a (galactic) background plus images of the quasar. The method has enabled appreciable improvement in the accuracy of astrometric and photometric measurements of this gravitational-lens system. The positions of the quasar images are determined with an accuracy of $0\farcs05$, and the brightness of individual components with an accuracy of 0.03^m for images with FWHM $\approx 0\farcs8$. © *2001 MAIK "Nauka/Interperiodica".*

1. INTRODUCTION

Gravitational lensing is an area of astrophysics in which interest has been sharply rising. The discovery of the first gravitational lenses at the end of the 20th century provided astronomers with a new and unique means to study and model the Universe. However, it is important to be able to extract useful information from these valuable data, which, as a rule, are obtained at the sensitivity and resolution limits of modern instrumentation. Information about image brightnesses and the geometry of the object are of the most interest. The reliability of results depends primarily on the astrometric and photometric accuracy of the methods used. Most identified lens systems and gravitational-lens candidates are difficult to analyze [1, 2]. The images of gravitational lenses consist primarily of several intersecting images of point sources (images of the lensed object). In some cases (such as the system QSO 2237+0305, known as the Einstein Cross), these images are superimposed on the image of the refracting body itself [3]. The Einstein Cross structure with its four quasar images against the background of the lensing galaxy represents the most difficult case for analysis.

The problem of the correct reconstruction of images has been discussed for a long time. Here, as in most astrophysical applications, we encounter the need to find solutions to inverse problems with various levels of complexity. Algorithms designed to deal with such problems can be divided into two groups according to the principle used to search for solutions. The first group includes various modifications of the CLEAN method (such as XECClean [4]), which is a method that essentially avoids exact solution of the inverse problem. The main idea behind algorithms forming the second group, which as a rule are based on the theory of Tikhonov (see [5]), is to search for extrema of a functional of a chosen type.

In the current paper, we study a method for image reconstruction proposed in 1997 by a group of Belgian scientists (Magain, Courbin, and Sohy, further abbreviated MCS) [9]. In a number of cases, this method can appreciably increase the resolution of images, as well as the accuracy of photometric and astrometric measurements. A comparison of the methods noted above and the MCS method can be found only in the work of Burud [10]. Analyzing the accuracy and reproducibility of these methods as applied to QSO 2237+0305, Burud [10] concluded that the MCS method was preferable according to most characteristics.

The construction of realistic light curves for the images of the Einstein Cross requires a series of regular observations of this object. However, the currently available observations of QSO 2237+0305

1063-7729/01/4510-0759$21.00

are far from uniform. In addition to individual ground-based observations [11–15] and observations using the Hubble Space Telescope [16, 17], two programs to monitor the Einstein Cross have been successfully carried out. The first international project [18] included three years of observations at two different telescopes, with observations separated by slightly less than one year. In spite of the sparse sampling of this study, Corrigan *et al.* [18] were able to detect significant variations in the brightness of component A of the Einstein Cross, and to obtain a preliminary estimate of the characteristic size of the emitting region in the quasar. The results of Ostensen *et al.* [19] proved to be more fruitful. These observations were carried out over five years on the Nordic Optical Telescope. The resulting light curves for the components of QSO 2237+0305 also have appreciable gaps; however, the segments corresponding to successful observations contain many more data points than previous datasets. Neither Corrigan *et al.* [18] nor Ostensen *et al.* [19] found evidence for high amplification events (HAEs).

In the current paper, we investigate the possibility of applying a new method for image reconstruction to images of QSO 2237+0305 obtained by the group of B.P. Artamonov in 1997. The lens was monitored at the Maĭdanak Observatory over four years, from 1996 to 1999. This yielded a unique series of long-term observations of the Einstein Cross (90 observing nights in the *BVRI* filters). We also analyze the characteristics of the MCS method and the dependence of our results on the seeing. We demonstrate that this method represents a modernization of the regularization algorithm of Tikhonov.

2. QSO 2237+0305

This gravitational lens was discovered by Huchra *et al.* [11] in 1985 during the Center for Astrophysics Redshift Survey. A broad emission line, subsequently found to belong to a quasar with a redshift of $z \approx 1.69$, was detected in the spectrum of the spiral galaxy 2237+0305. The redshift of the galaxy is $z \approx 0.039$. This is currently the only known system in which the lensing galaxy is located so nearby. This advantageous combination of circumstances provides opportunities for detailed studies of the galaxy and to constrain possible models for the system in a natural way. The hypothesis that gravitational lensing was probable was confirmed by observations of this object with high angular resolution [12] and by spectroscopic data [20]. Four images of the quasar (the Einstein Cross) were detected in the central region of 2237+0305, with the maximum distance between the images being $1\farcs8$. Gravitational-lensing theory predicts the formation of an odd number of images in such a system [21]. Based on the results of new observations, Racine [13] pointed out the existence of a fifth image close to the nucleus of the galaxy; however, this has not been confirmed by other studies. The mass of the gravitational lens inside the four images is estimated to be $2 \times 10^{10} h_{50}^{-1} M_\odot$, and the total amplification coefficient is about 18.5 [17].

Many studies (see, for example, [22]) have noted that the Einstein Cross provides a unique system for investigations of microlensing. Indeed, the large time delay makes it easy to identify intrinsic variations in the quasar brightness from the brightness variations of the individual images due to microlensing. Note also that the probability of HAEs in the system is high. Based on observations of QSO 2237+0305 by various groups from 1988 to 1994, we can distinguish two exceptional microlensing events: one for component A in 1988 and the second for component B in 1991.

The most complete light curves of the Einstein-Cross images have been obtained by Ostensen *et al.* [19]. These data clearly illustrate appreciable variations in the light curves of all four components in the *I* and *R* filters. Against the background of long-term brightness variations with a time scale of several years, individual more rapid variations with durations of several weeks can be distinguished. The group of Ostensen reported that they had not detected signs of high-amplification microlensing events during their monitoring of the Einstein Cross from 1990–1994.

An analysis of the extensive results produced by studies of QSO 2237+0305 [19, 23–31] makes clear the need to derive accurate light curves of the system. Accurate photometric measurements of this object are important both for the construction of plausible mass distributions for the galaxy and for detailed investigations of microlensing events, as well as for other applications of gravitational-lensing studies, such as the determination of the Hubble constant. It is obvious that the Einstein Cross is one of the best objects for various studies among currently known gravitational lenses. However, its value is limited by the difficulty of acquiring accurate photometric measurements of its components. The stumbling block here is the galaxy underlying the quasar images, which creates a complex and nonuniform background. This makes the results of photometric measurements model-dependent, since most algorithms require the use of additional information about the object. We cannot be certain that the resulting component brightnesses will not be adversely affected by the need to use various theoretical models for the galaxy.

Figure 1 presents an image derived by summing six frames obtained on the AZT-22 telescope with a 12-m focus at the Maĭdanak Observatory. The

size of the field is approximately $4' \times 4'$. The spiral galaxy 2237+0305 can clearly be seen. The size of the enlarged region is 20×20 pixels, which corresponds to $5\farcs5 \times 5\farcs5$. The letters α, β, γ denote individual stars to which we will refer below, and the letters A, B, C, and D indicate the quasar components. We also introduce the notation N for the nucleus of the galaxy.

3. OBSERVATIONS AND PRELIMINARY DATA REDUCTION

The images of QSO 2237+0305 we analyze here were obtained using the 1.5-m AZT-22 telescope at the Maĭdanak Observatory, which is located to the south of Tashkent at an altitude of 2600 m. The observations were carried out by B.P. Artamonov (Sternberg Astronomical Institute), V.N. Shalyapin (Radio Astronomy Institute, Ukraine), and I. Khamitov (Ouloug-Beg Astronomical Institute, Uzbekistan) on November 9 and 10, 1997.

The observations were obtained using the TI800×800 Texas Instruments CCD array of St. Petersburg State University, which has a pixel size of 15 μm, corresponding to approximately $0\farcs27$, mounted on the 1.5-m AZT-22 telescope for a quasar monitoring program. The CCD array was located in a liquid-nitrogen-cooled cryostat.

All exposures were 120 s. The mean seeing corresponded to a point source having a FWHM (Full Width at Half Maximum) of $\approx 0\farcs8$. The observations were carried out in the standard way, with bias and flatfield frames acquired at the beginning and end of the observing night. The preliminary reduction of each frame included subtraction of the bias and multiplication by the mean flatfield. We also corrected for bad pixels and subtracted cosmic rays.

The accuracy of photometric measurements is determined by the signal-to-noise ratio. Images acquired with a CCD array can potentially be distorted by numerous sources of noise. However, work with a good-quality, well-adjusted CCD array should require taking into account only background noise and readout noise. Assuming that the background noise is Poisson, we can write the signal-to-noise ratio

$$\frac{S}{N} = \frac{S}{\sqrt{\sigma_{\rm ro}^2 + I/g}}, \qquad (1)$$

where S is the flux integrated over the image area for a point source after subtraction of the random background, I is the total flux in the point source, $\sigma_{\rm ro}$ is the readout noise, and g is the CCD gain. In the 120-s exposures used in our study ($\sigma_{\rm ro} = 10e^-$, $g = 1$), S/N varies from 100 to 150.

The main characteristic of an astronomical image is the transfer function, or, as it is sometimes called,

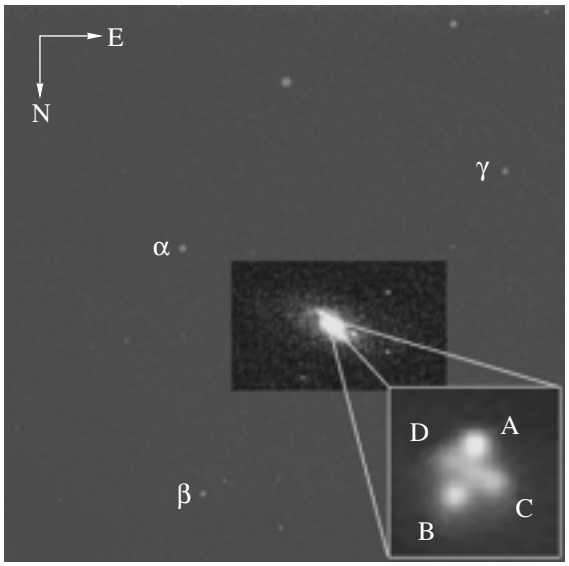

Fig. 1. Image of the neighborhood of QSO 2337+0305. The size of the frame is $6\farcm5 \times 6\farcm5$. The size of the enlarged region is $5\farcs5 \times 5\farcs5$.

the point spread function (PSF). This is the two-dimensional intensity distribution of a point source in the image. Thus, the observed intensity distribution $d(x, y)$ is the convolution of the real distribution $f(x, y)$ and the transfer function $t(x, y)$:

$$d(x,y) = \int_{-\infty}^{+\infty}\int_{-\infty}^{+\infty} t(x-\xi, y-\eta) f(\xi,\eta)\, d\xi d\eta \equiv t * f. \qquad (2)$$

The PSF is the same for all stars in a frame, independent of their brightness and position. Thus, images of bright and weak stars should differ only in a scaling factor. The fraction of the total intensity in a given aperture does not depend on the brightness of the star. This is the principle of aperture photometry. In photometric measurements, the characteristic variation in the total intensity with an increase in the aperture size is monitored to determine the radius at which the main contribution ceases to be made by the starlight and becomes dependent only on the background noise. Aperture photometry is usually used for measurements of the intensities of individual bright stars. It is practically impossible to apply this algorithm in regions with numerous intersecting sources with different magnitudes. Such cases require the use of so-called PSF photometry. Here, the desired result is achieved by approximating the images in a frame using a transfer function of a specified form. The necessary point spread function is determined from observations of individual stars in the frame under study. There are three different

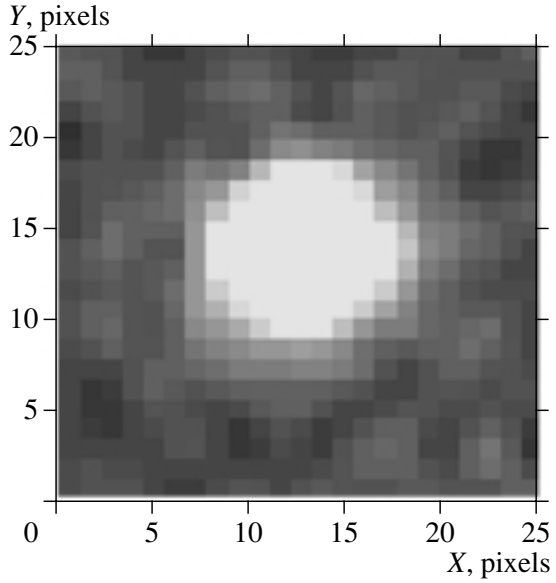

Fig. 2. Image of a star (FWHM$\approx 0.''8$). The pixel size is $\approx 0.''14$.

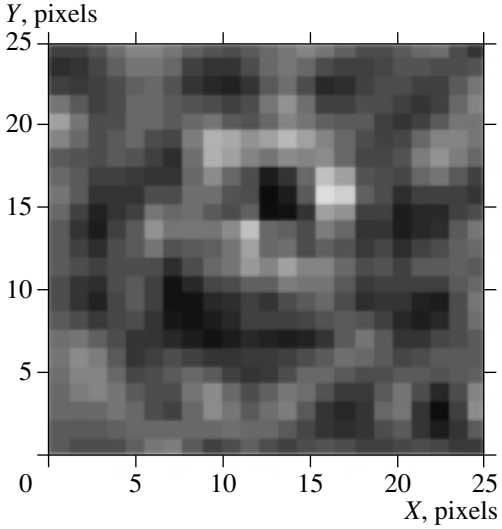

Fig. 3. Error distribution for a modelled PSF. The pixel size is $\approx 0.''14$.

methods for constructing the PSF. The first uses a numerical point spread function; i.e., an empirical brightness profile for the stars in the frame is adopted as the PSF. This method is free of any assumptions about the shape of the transfer function, but depends on the grid used to construct the brightness profile. This can lead to difficulties in reproducing the PSF at other points of the frame. A stellar image can also be approximated using a theoretical brightness distribution (a Gaussian or Moffat distribution). One advantage of this approach is the simplicity of the computations; however, the adopted approximation is not always a good representation of the real brightness distribution. Finally, a third possible method is a combination of the first two: an analytical brightness distribution is corrected using tabulated residuals obtained by comparing the image of a chosen star and the theoretical point spread function.

We investigated the application of transfer functions of the second and third type using two-dimensional circular and elliptical Gaussian distributions for the theoretical profiles (both with and without allowance for rotation of the ellipse). As a result of our analysis of the reconstructed images and residual (data−model) distributions, we chose the elliptical PSF model allowing for rotation of the ellipse. When approximating field stars, we found that the axial ratio for the resulting PSF (b/a, where b is the minor axis and a the major axis) could be varied from 0.925 to 0.997. We constructed the transfer function in two ways: (1) using individual stars (α, β, γ) and (2) using the mean brightness distribution obtained by superposing the profiles for individual stars (α, β, γ). In the latter case, the stars were registered with an accuracy of ≈ 0.01 of a pixel and were superposed with weights inversely proportional to their intensities. We found that the best model for the PSF was obtained using the star α. Figure 2 presents a typical image for the field star α (the X and Y axes show the corresponding pixel numbers; here and below in Figs. 3 and 4, the scale is decreased to $0.''14$ per pixel via interpolation). For further use in the reconstruction algorithm, this image was interpolated to a new, denser pixel grid. The seeing corresponds to a FWHM of $\approx 0.''8$. Figure 3 presents the distribution of the approximation errors (model − data). Figure 4 depicts the observed and theoretical (solid curve) brightness profiles (slices through the two-dimensional distribution along the X axis). We used the total loss in the intensity as an estimate of the accuracy of a constructed model for the transfer function. Let k be the ratio of the integrated model intensity to the integrated intensity for an observed field star. The total loss in intensity y can be described by the simple formula

$$y = (1 - k) \times 100\%.$$

The quantity y varies from 0.1 to 0.7% for various stars. For the stars imaged in Fig. 2, the total loss in intensity is $100\% - 99.4\% = 0.6\%$.

We also used the semi-analytical RAS (Rotate-And-Stare) method [32] to construct the point spread function. The RAS algorithm yields a one-dimensional profile derived from levels of constant intensity. The intensity of a specific level is calculated as the weighted sum of the contributions of individual pixels delineated by concentric rings of a specified width with their common center at the center of the star.

The PSFs determined using the RAS method are in excellent agreement with those theoretically modelled using elliptical Gaussian distributions. In our subsequent analysis, we used a two-dimensional Gaussian approximation for the transfer function.

4. METHOD FOR IMAGE RECONSTRUCTION

The progress of astronomy has always been closely linked to progress in observational techniques and the improvement of the quality of astronomical images. Unfortunately, even the most modern instruments have a finite resolving power. The light from a point source is smeared by the telescope, and the angular size of the resulting image is inversely proportional to the diameter of the primary mirror. If observations are carried out on a ground-based telescope, turbulent motions of the air in the atmosphere also contribute to degradation of the image quality. The resulting image can be described mathematically as a convolution of the real brightness distribution and the total transfer function, including the instrumental transfer function and the contribution of atmospheric turbulence:

$$A[f](x,y) \equiv \int\int_D t(x-\xi, y-\eta) \times f(\xi,\eta)\, d\xi d\eta = d(x,y), \quad (x,y) \in D. \tag{3}$$

Here, $f(x,y)$ is the desired intrinsic brightness distribution, $t(x,y)$ the total transfer function, $d(x,y)$ the observed brightness distribution, and D the region covered by the frame. The goal of a reconstruction algorithm is to derive the original brightness distribution $f(x,y)$, given the observed brightness distribution $d(x,y)$ and point spread function $t(x,y)$. Thus, the task of reconstructing the image of an astronomical object can be represented as a solution of a two-dimensional integral Fredholm equation of the first kind, whose kernel depends on the difference of the arguments. The right-hand side of (3) is specified approximately with some error δ, due to the presence of random noise. The most widespread method for the solution of this type of ill-posed inverse problem is the regularization method of Tikhonov (see [5, 33, 34]). The idea behind this method is to chose a function f for an approximate solution, such that the smoothed functional $M^\alpha[f]$ reaches a minimum, where

$$M^\alpha[f] = \|A[f] - d\|^2_{L_2} + \alpha\Omega[f]. \tag{4}$$

Here, $\Omega[f]$ is the regularized functional, whose form is chosen taking into account *a priori* information about the desired solution, and α is a regularization parameter chosen in accordance with the developed criteria [5, 33, 34].

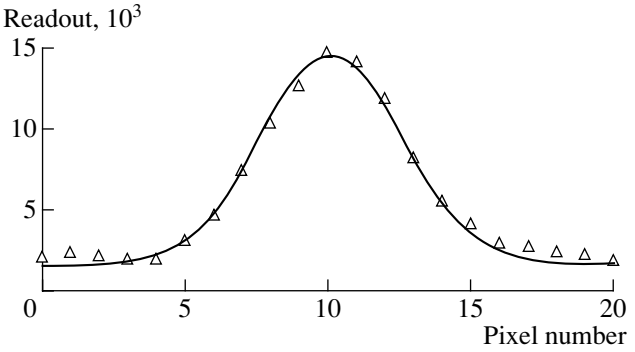

Fig. 4. Observed (triangles) and theoretical (solid curve) brightness profile. The pixel size is $\approx 0.''14$.

The brightness distribution in an image obtained with a CCD array is not continuous, and is represented by a series of sampled values (the intensities in each pixel). It is necessary to rewrite (3) taking into account the pixel grid $x_i = \xi_i = i\Delta_0$, $i = 0, \ldots, n_1 - 1$, $y_j = \eta_j = j\Delta_0$, $j = 0, \ldots, n_2 - 1$, where Δ_0 is the initial pixel size and n_1 and n_2 are the numbers of sampled points along the corresponding axes. Approximating the integral in (3) using a rectangle formula and introducing the notation $d_{ij} = d(x_i, y_j)$, $f_{ij} = f(x_i, y_j)$, $t_{i-l,\, j-m} = t(x_i - \xi_l, y_j - \eta_m)$, we obtain

$$\sum_{l=0}^{n_1-1}\sum_{m=0}^{n_2-1} t_{i-l,\, j-m} f_{lm} \Delta_0^2 = d_{ij}. \tag{5}$$

A finite-difference approximation for the functional (4) has the form

$$M^\alpha[f] = \sum_{i=0}^{n_1-1}\sum_{j=0}^{n_2-1} \frac{\Delta_0^2}{\sigma_{ij}^2} \times \left[\sum_{l=0}^{n_1-1}\sum_{m=0}^{n_2-1} t_{i-l,\, j-m} f_{lm}\Delta_0^2 - d_{ij}\right]^2 + \alpha\Omega[f], \tag{6}$$

where σ_{ij} is the error in the intensity at the point (x_i, y_j).

One of the most important problems of reconstruction algorithms is determining the relative contributions to the resulting image of point sources and of the background. We know that, on the whole, typical astronomical images cannot be considered flat: point sources (stars and so forth), which, in the ideal case, can be represented as Dirac δ functions, will appear in our frame as sharp brightness enhancements against a background of slower intensity variations. Therefore, it is logical to separate the image under consideration here into two components: the quasar

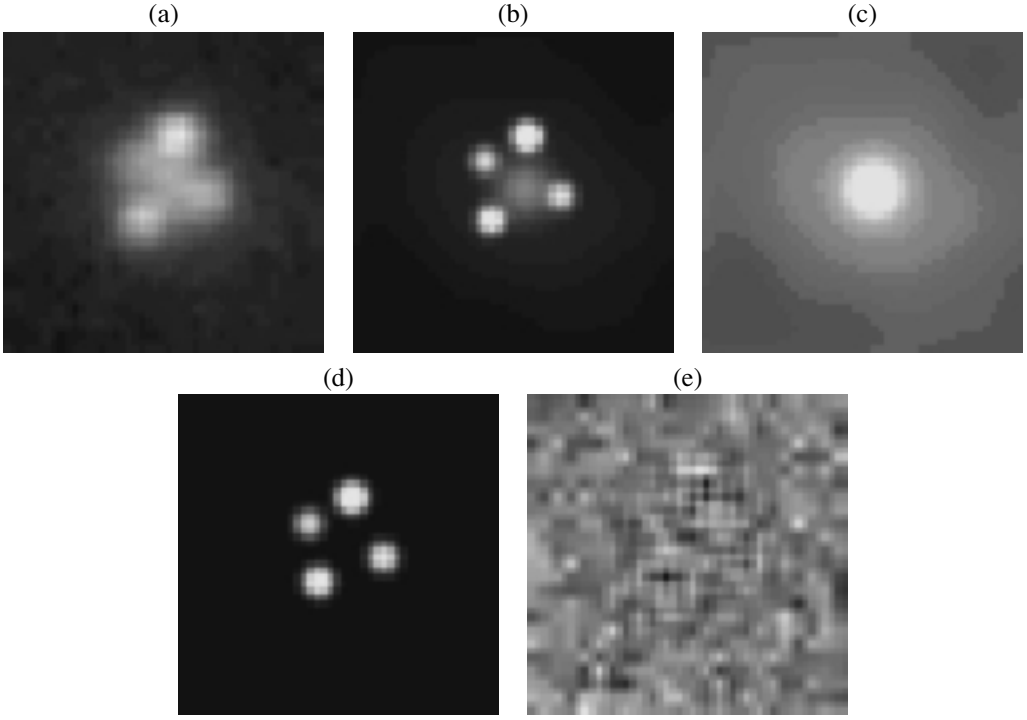

Fig. 5. (a) Observed image, (b) reconstructed image, (c) central region of the galaxy 2237+0305, (d) components of the quasar, and (e) error distribution = (model − data)/$\sqrt{\text{model}}$.

components (a sum of δ functions) and a smooth background (the galaxy):

$$f(x,y) = \sum_{k=1}^{K} a_k \delta(x - b_k, y - c_k) + h(x,y), \quad (7)$$

where K is the number of point images in the frame, specified by the coordinates (b_k, c_k) and intensities a_k, and $h(x,y)$ is the image of the galaxy.

Another problem is that the relative dimensions of the processed images are small. In this case, the accuracy of measurements can be increased by decreasing the sample step and interpolating the intensity distribution onto a denser grid of sample values. The need for a correct implementation of this procedure led to the creation of the following image reconstruction method based on the regularization algorithm of Tikhonov (further, the MSC method) in 1997 at the Liège Astronomical Institute in Belgium [9].

In the MCS method, the image reconstruction does not use the total transfer function $t(x,y)$, but instead some narrower distribution $s(x,y)$, chosen such that the transfer function $r(x,y)$ of the reconstructed image has characteristic dimensions that are comparable to the initial width of the sampling step. The transfer functions $t(x,y)$, $r(x,y)$, and $s(x,y)$ are related by the simple expression

$$t = r * s. \quad (8)$$

Thus, approximating a background star using a two-dimensional Gaussian distribution, we find the parameters σ_{tx}, σ_{ty}, and T, and obtain the total function $t(x,y)$:

$$t(x,y) = \frac{1}{2\pi\sigma_{tx}\sigma_{ty}} \exp\left\{-\frac{x'^2}{2\sigma_{tx}^2} - \frac{y'^2}{2\sigma_{ty}^2}\right\}, \quad (9)$$

$$x' = x\cos T - y\sin T,$$

$$y' = x\sin T + y\cos T.$$

Further, we interpolate the intensity distribution in the frame onto a denser pixel grid with step $\Delta = \Delta_0/n$ (recall that Δ_0 is the initial pixel size). We chose a transfer function $r(x,y)$ in the form of a two-dimensional, symmetrical Gaussian distribution:

$$r(x,y) = \frac{1}{2\pi\sigma_r^2} \exp\left\{-\frac{x^2}{2\sigma_r^2} - \frac{y^2}{2\sigma_r^2}\right\}, \quad (10)$$

with the parameter σ_r ($\sigma_r < \min\{\sigma_{tx}, \sigma_{ty}\}$) chosen such that the full width at half maximum of the distribution $r(x,y)$ exceeds the initial pixel size $n\Delta$. We used the following conditions for the choice of σ_r:

$$\sigma_r = \frac{n\Delta}{2\sqrt{2\ln 2}}. \quad (11)$$

Next, proceeding from (8) and using the convolution theorem, we determine the function $s(x,y)$. It is obvious that this function will be an elliptical Gaussian

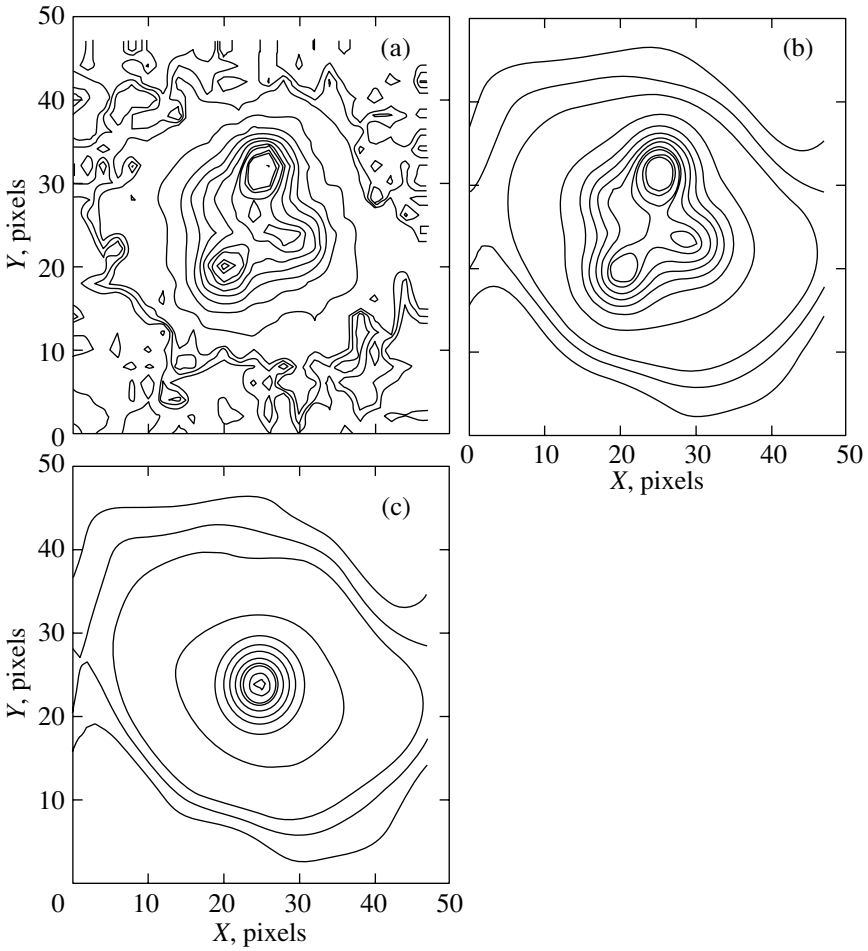

Fig. 6. Contours of constant brightness: (a) observed image, (b) resulting model, and (c) central part of the galaxy 2237+0305.

distribution in this case:

$$s(x,y) = \frac{1}{2\pi\sigma_{sx}\sigma_{sy}} \exp\left\{-\frac{x'^2}{2\sigma_{sx}^2} - \frac{y'^2}{2\sigma_{sy}^2}\right\}, \quad (12)$$

$$x' = x\cos T - y\sin T,$$

$$y' = x\sin T + y\cos T,$$

where $\sigma_{sx} = \sqrt{\sigma_{tx}^2 - \sigma_r^2}$, $\sigma_{sy} = \sqrt{\sigma_{ty}^2 - \sigma_r^2}$.

We now seek not the initial brightness distribution $f(x,y)$, but instead some function $f'(x,y)$ that is the convolution of $f(x,y)$ with the specified function $r(x,y)$. Then, if the processed frame includes point sources, their shape in the reconstructed image will be precisely known: it will simply be $r(x,y)$. Thus, we can write an expression for the function $f'(x,y)$ in the form

$$f'(x,y) = \sum_{k=1}^{K} a_k r(x - b_k, y - c_k) + h'(x,y), \quad (13)$$

where $h'(x,y)$ is an additional component of the solution, corresponding to the (in most cases) smooth background.

To avoid deformation of the smooth background (which, in our case, is far from a flat spiral galaxy), it is natural to require that the function $h'(x,y)$ be smooth on scales $r(x,y)$, which can be achieved by chosing a regularizer of the form $\Omega(h') = \|h' - r * h'\|_{L_2}^2$.

Thus, we seek a solution minimizing the functional

$$M^\alpha[h', a_k, b_k, c_k] \quad (14)$$

$$= \sum_{i=0}^{N_1-1}\sum_{j=0}^{N_2-1} \frac{\Delta^2}{\sigma_{ij}^2}\left[\sum_{l=0}^{N_1-1}\sum_{m=0}^{N_2-1} s_{i-l,\,j-m} \times \left\{h'_{lm} + \sum_{k=1}^{K} a_k r_{l-p_k,\,m-q_k}\right\}\Delta^2 - d_{ij}\right]^2$$

$$+ \alpha \sum_{i=0}^{N_1-1}\sum_{j=0}^{N_2-1} \Delta^2\left[h'_{ij} - \sum_{l=0}^{N_1-1}\sum_{m=0}^{N_2-1} r_{i-l,\,j-m} h'_{lm}\Delta^2\right]^2,$$

which is written on the new grid $x_i = \xi_i = i\Delta$, $i = 0, \ldots, N_1 - 1$, $y_j = \eta_j = j\Delta$, $j = 0, \ldots, N_2 - 1$, where N_1 and N_2 are the number of sampled points

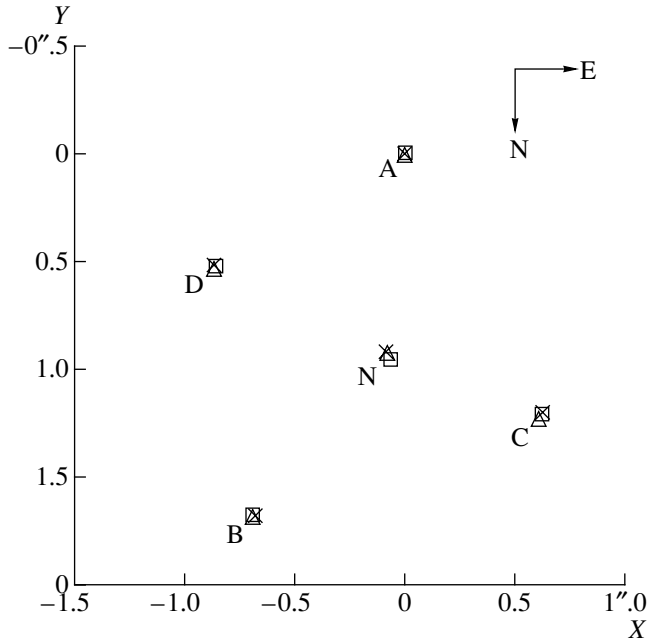

Fig. 7. Positions of the components of the quasar QSO 2237+0305 according to our data and the data of Rix *et al.* [17] and Burud [10].

along the X and Y axes, respectively ($N_i = n_i(n_i - 1) + 1,\ i = 1, 2$). Here, we have used the notation $s_{i-l,\,j-m} = s(x_i - \xi_l, y_j - \eta_m)$, $h'_{ij} = h'(x_i, y_j)$, $r_{i-p_k,\,j-q_k} = r(x_i - p_k\Delta, y_j - q_k\Delta)$, $d_{ij} = d(x_i, y_j)$, $r_{i-l,\,j-m} = r(x_i - \xi_l, y_j - \eta_m)$. The pairs of numbers p_k, q_k $(k = 1, \ldots, K)$ determine the grid points at which point sources are located, whose coordinates (b_k, c_k) are then expressed as $b_k = p_k\Delta$, $c_k = q_k\Delta$. The variable quantities in (14) are h'_{ij} $(i = 0, \ldots, N_1 - 1,\ j = 0, \ldots, N_2 - 1)$, a_k, p_k, and q_k $(k = 1, \ldots, K)$. If the distribution $r(x, y)$ is chosen such that $\|r\|_{L_2} \neq 1$, then $\Omega(h')$ satisfies the condition $g_1\|h'\|_{L_2} \leq \Omega(h') \leq g_2\|h'\|_{L_2}$, $g_1, g_2 > 0$ and, consequently, gives rise to an equivalent norm in the space L_2. The theory of solving ill-posed problems via the minimization of a Tikhonov functional with the regularizer $\Omega(z) = \|z\|^2_{L_2}$ is described in [5], and here we only introduce the result. A regularizing algorithm is an algorithm in which an extremum of the Tikhonov functional at a value of the regularization parameter chosen in accordance with the residuals is adopted as an approximate solution of an ill-posed problem. Choice of the parameter α in accordance with the residuals can be described as a search for α such that the resulting χ^2 distribution displays the correct statistical behavior $\chi^2 \approx N$. In this way, this method is a regularization method in L_2 (i.e., to zeroth order), converging not to the solution, but instead to the convolution of the solution with the *a priori* specified function $r(x, y)$.

5. RESULTS

We created a set of IDL programs designed to realize this algorithm. We used the observations of QSO 2237+0305 in the R filter for the reduction. The pixel size was decreased to half of its initial size ($0\farcs27/2 \approx 0\farcs14$). We chose the transfer function for the reconstructed image to have the form of a Gaussian distribution ($a = b$) with FWHM = 3 pixels = $0\farcs42$. Since the galaxy 2237+0305 has a fairly bright nucleus, we introduced an additional point source in the model to absorb the most rapid background variations. Thus, the reconstructed distribution of the intensity in the galaxy was the sum of the bright nucleus (a Gaussian) and a numerically modelled background.

Figures 5 and 6 illustrate the results of processing one of the images, obtained on November 10, 1997. The seeing corresponds to FWHM $\approx 0\farcs8$. The window size is 24×24 pixels ($6\farcs5 \times 6\farcs5$). We can see that the algorithm has successfully separated the observed image into two components—the quasar components and the lensing galaxy. The probability that the resulting model cannot be rejected is 0.98. The maximum deviations in the residual distribution of $\pm 4\sigma$ are associated with the positions of the individual components and may be due to errors introduced when approximating the PSF as a Gaussian distribution (Fig. 3). Neiher Fig. 5 nor Fig. 6 show any signs of artefacts distorting the image structure.

The positions of the quasar components relative to component A are shown in Fig. 7. For comparison,

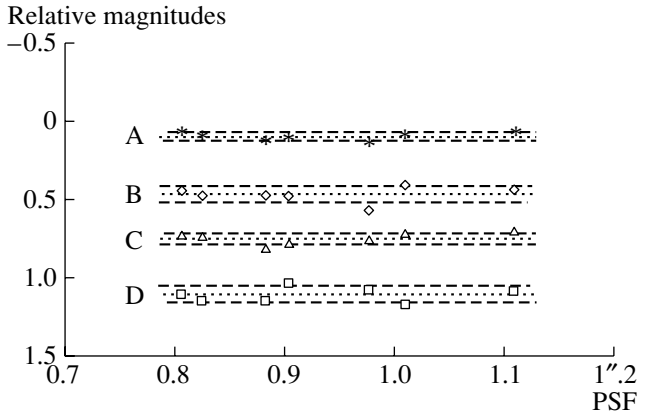

Fig. 8. Dependence of the magnitudes of the components on seeing.

we also present the data of Rix *et al.* [17] and Burud [10].

Figure 8 shows the dependence of the brightness of the quasar components on the seeing. The X axis plots the FWHM in arc seconds, and the Y axis, the relative magnitudes of the components (the component magnitudes minus the magnitude of the star α). We calculated the following mean R magnitudes and standard deviations σ for each component:

	A	B	C	D
$\overline{m - m_*}$	0.09	0.46	0.74	1.09
σ	0.03	0.05	0.03	0.05

We can propose two methods to further improve the quality of the photometric measurements. The first uses a numerical model for the galaxy derived by reconstructing a frame with good seeing to process frames with poorer seeing. In this way, we fix the background h_i, and have for the galaxy model in the reconstructed images

$$h'_i = h_i z_{1i} + z_{2i},$$

where z_1 and z_2 are coefficients correcting the model for different exposure times and night-sky brightness levels. The second method involves the simultaneous reconstruction of several frames, searching for the minimum of a total functional. This method could provide more accurate results in searches for variability of individual components but requires vastly larger amounts of computing time.

The algorithm we have applied provided good results for both astrometric measurements and photometry of individual components. An undoubted advantage of the method is the stability of the results to the use of images with differing seeing.

6. CONCLUSIONS

Our investigation of the new MCS method for reconstructing images has demonstrated the possibility of using this algorithm to extract information from frames with modest image quality.

One advantage of the method is the absence of defects in the reconstructed image, due to the correct use of the data and the invocation of natural supplementary conditions for solving the inverse problem (dividing the image into two components). One of the main problems that arose during the reduction of the images of QSO 2237+0305 was the choice of a good model for the galaxy. Applying the MCS algorithm, we are able to use a fully numerical model. In this way, we minimize errors associated with a non-optimal choice of analytical profile for the galaxy brightness. The astrometric and photometric results obtained using this method are virtually free of the influence of seeing. If required, the results can be improved by fixing the numerical model for the galaxy.

Our task also included studies of the quality of original data obtained on the AZT-22 1.5-m telescope at the Maĭdanak Observatory using a TI800×800 CCD array. Our main conclusion is that it is possible to derive the intensities of the individual components of QSO 2237+0305 with rather high accuracy using these observational data and the MCS method.

ACKNOWLEDGMENTS

This work was supported by the Russian Foundation for Basic Research (project codes 98-02-17490 and 99-01-00447) and the Federal Science and Technology Program "Astronomy. Fundamental Cosmic Research" (grant 1.2.5.5). The authors also thank the "Universities of Russia—Fundamental Research" (grant 4-5220) for partial support of this work.

REFERENCES

1. P. V. Bliokh and A. A. Minakov, *Gravitational Lenses* [in Russian] (Naukova Dumka, Kiev, 1989).
2. A. F. Zakharov, *Gravitational Lenses and Microlenses* [in Russian] (Yanus-K, Moscow, 1997).
3. M. V. Sazhin and V. M. Sidorov, Preprint No. 3 of the High Mountain Observatory of the Sternberg Astronomical Institute (1989).
4. J. Teuber, *Digital Image Processing* (Prentice Hall, Englewood Cliffs, 1993).
5. A. N. Tikhonov, A. V. Goncharskiĭ, V. V. Stepanov, and A. G. Yagola, *Numerical Methods for Solutions of Ill-Posed Problems* [in Russian] (Nauka, Moscow, 1990).
6. B. Roy Frieden, J. Opt. Soc. Am. **62**, 4 (1971).

7. R. Narayan and R. Nityananda, Ann. Rev. Astron. Astrophys. **24**, 127 (1986).
8. J. Skilling and R. K. Bryan, Mon. Not. R. Astron. Soc. **211**, 111 (1984).
9. P. Magain, F. Courbin, and S. Sohy, astro-ph/9704059 (1997).
10. I. Burud, Candidata Scientiarum Thesis (1997).
11. J. Huchra, M. Gorenstein, S. Kent, *et al.,* Astron. J. **90**, 691 (1985).
12. H. K. C. Yee, Astron. J. **95**, 1331 (1988).
13. R. Racine, Astron. J. **102**, 454 (1991).
14. M. Houde and R. Racine, Astron. J. **107**, 466 (1994).
15. V. G. Vakulik, V. N. Dudinov, A. P. Zheleznyak, *et al.,* Astron. Nachr. **318**, 73 (1997).
16. P. Crane, Astrophys. J. Lett. **369**, L59 (1991).
17. H.-W. Rix, D. P. Schneider, and J. N. Bachall, Astron. J. **104**, 959 (1992).
18. R. T. Corrigan, M. J. Irwin, G. G. Fahlman, *et al.,* Astron. J. **102**, 34 (1991).
19. R. Ostensen, S. Refsdal, R. Stabell, *et al.,* Astron. Astrophys. **309**, 59 (1996).
20. H. K. C. Yee and M. M. DeRobertis, Astrophys. J. Lett. **398**, L2 (1992).
21. A. F. Zakharov and M. V. Sazhin, Usp. Fiz. Nauk **168** (10) (1998) [Phys. Usp. **41**, 945 (1998)].
22. R. Kayser, S. Refsdal, and R. Stabell, Astron. Astrophys. **166**, 36 (1986).
23. C. R. Keeton and C. S. Kochanek, astro-ph/9705194 (1997).
24. P. Schneider, E. L. Turner, J. E. Gunn, *et al.,* Astron. J. **95**, 1619 (1988).
25. C. S. Kochanek, Astrophys. J. **373**, 354 (1991).
26. J. Wambsganss and B. Paczynski, Astron. J. **403**, 517 (1994).
27. H. J. Witt and S. Mao, Astrophys. J. **429**, 66 (1994).
28. K.-H. Chae, D. A. Turnshek, and V. K. Khersonsky, Astrophys. J. **495**, 609 (1998).
29. K.-H. Chae, D. A. Turnshek, and V. K. Khersonsky, astro-ph/9808354 (1998).
30. E. E. Falco, J. Lehar, R. A. Perley, *et al.,* Astron. J. **112**, 897 (1996).
31. S. Refsdal and R. Stabell, Astron. Astrophys. **278**, L5 (1993).
32. J. Teuber, R. Ostensen, R. Stabell, *et al.,* Astron. Astrophys., Suppl. Ser. **108**, 509 (1994).
33. A. V. Goncharskiĭ, A. M. Cherepashchuk, and A. G. Yagola, *Ill-Posed Problems in Astrophysics* [in Russian] (Nauka, Moscow, 1985).
34. A. V. Goncharskiĭ, A. M. Cherepashchuk, and A. G. Yagola, *Numerical Methods for Solution of Inverse Problems in Astrophysics* [in Russian] (Nauka, Moscow, 1978).
35. A. N. Tikhonov, V. V. Vitkevich, V. S. Artyukh, *et al.,* Astron. Zh. **46**, 472 (1969) [Sov. Astron. **13**, 374 (1969)].

Translated by D. Gabuzda

Astronomy Reports, Vol. 45, No. 10, 2001, pp. 769–783. Translated from Astronomicheskiĭ Zhurnal, Vol. 78, No. 10, 2001, pp. 887–901.

Arc-Shaped and Spheroidal Stellar Complexes

Yu. N. Efremov

Sternberg Astronomical Institute, Universitetskiĭ pr. 13, Moscow, 119899 Russia

Received March 5, 2001

Abstract—Complexes of young clusters and high-luminosity stars in the shape of regular, circular arcs have been found in a number of galaxies, first and foremost the LMC, NGC 6946, and M83. These shapes are found even in strongly inclined galaxies, suggesting that the observed arcs are projections of partial spherical shells. Obviously, these stellar shells must have formed from gaseous shells swept up by some source of central pressure and become gravitationally unstable. The power of this source corresponds to several dozen supernova explosions; however, its nature remains unclear. A central cluster providing a source of O stars and supernovae is usually absent. The presence of multiple arcs located close to each other can be explained by the fall of a swarm of fragments or by the progenitor stars originating in a single peculiar star cluster, implying the existence of stellar objects capable of giving rise to explosions with energies an order of magnitude higher than those of individual supernovae. The same objects may be responsible for gamma-ray bursts. It may be that only the most massive clusters with frequent or especially powerful supernova explosions are capable of producing HI supershells. Otherwise, it is impossible to explain why no supershells have been found around numerous clusters that should be capable of producing them according to current theories. The presence of star clusters in shell-like structures provides extremely important information about the physical conditions in and the ages of the initial gaseous shells, making stellar arcs the best available laboratory for studies of triggered star formation.

1. INTRODUCTION

Stellar complexes unify most stellar associations and young clusters, together with less young individual stars (e.g., Cepheids), into giant groupings with sizes ranging from 0.5 to 1.0 kpc [1, 2]. Complexes can be concentrated along the spiral arms of galaxies, where they are sometimes closely spaced, or randomly scattered throughout irregular galaxies. The formation of ordinary stellar complexes is due to general mechanisms acting on galactic scales, first and foremost, to large-scale gravitational instabilities in the gaseous disks of galaxies [3].

However, some galaxies are known to contain isolated young stellar complexes, often with peculiar shapes. These either have sharp, circular edges or contain arc-shaped structures made up of young stars and clusters. Such complexes are isolated, are often located on the outskirts of the host galaxy, and appear as separate formations. One cannot help but have the impression that the star formation in these regions must have been triggered by some source of pressure near the centers of curvature of the arc-shaped structures. One distinguishing feature of many isolated complexes is a sharp outer edge, indicating that gravitational forces did not play the dominant role in the formation of these stellar systems. The rarity of these objects may be partly due to their obvious expansion, implying that they should become scattered and then lost among field stars over several tens of millions of years; i.e., it is not only the decrease of the member-stars' luminosities with age that causes these objects to become less prominent with time. All the available evidence indicates that stars and clusters in arc-shaped complexes formed inside gaseous shells, which, in turn, were produced by some source of central pressure unrelated to the surrounding region of the galaxy. Most of these complexes are characterized by a large fraction of star clusters, indicative of a high efficiency of star formation.

Studies of such complexes should eventually reveal the nature of the corresponding progenitor events. Such investigations have become especially topical in connection with the possibility that the formation of such complexes is associated with gamma-ray bursts [4, 5]. Whatever the nature of their central sources, these complexes provide the best available laboratory for studying triggered star formation.

The first collection of giant, ring-shaped structures with diameters of several kiloparsecs was reported by Hayward [6], who considered them to be possible remnants of superpowerful supernovae, citing Shklovskiĭ [7]. Most of the formations he identified are probably not real; this applies, first and foremost, to the giant arcs and ellipses of young stellar

1063-7729/01/4510-0769$21.00

complexes in M101 and M74. However, the system of five bright, giant rings in NGC 7741 appears to be real, and a bright star cluster is located in the center of one of the arcs.

Hayward [6] also pointed out several dark arcs in M31, which are clearly optical counterparts of HI and H_2 shells. Such features are numerous in images of gas-rich galaxies, as first noted by Brand and Zealey [8], who also reported a list of arc- and loop-shaped dust structures in the Milky Way. However, most of these are not related to star-forming regions in any obvious way.

Later, Westerlund and Mathewson [9] described a "large arc of bright blue stars" located at the northeastern edge of the Large Magellanic Cloud (LMC), in the region of an HI–HII supershell that later became known as the LMC4 supershell. They erroneously identified this region with Shapley's "Constellation III." Westerlund and Mathewson [9] also attributed the formation of both the arc and the hydrogen cavity in which it resides to the explosion of a super supernova. Soon afterwards, Hodge [10] pointed out three other arcs near the first arc, and his search for similar features in other galaxies led to the discovery of another system of arcs in the galaxy NGC 6946. Hodge also interpreted both systems as relicts of hypothetical super-supernovae.

To our knowledge, giant arcs of stars and clusters have been described in only two other papers. Vader and Chaboyer [11] discovered a giant arc of young clusters surrounding the largest cluster in the spiral galaxy NGC 1620 and studied this feature in detail. Ryder *et al.* [12] noted a large stellar arc in the vicinity of the HI supershell in the irregular galaxy NGC 1313, which they describe as being similar to "Constellation III" in the LMC, noting that the center of this arc lies outside the HI supershell. Efremov *et al.* [4] found a round, sharp-edged feature in M101, which, if observed at low resolution, appears similar to Hodge's object in NGC 6946. At about the same time, Efremov [5] provided a brief description and coordinates of an isolated stellar complex and two stellar arcs in M83.

We looked for similar features in the galaxies depicted in the atlas of Sandage and Bedke and in many other atlases. Though it is far from complete, our sample already enables us to draw certain conclusions concerning the nature of these features, which we describe in this paper.

2. THE SYSTEM OF GIANT STELLAR ARCS IN THE LMC

The system of arc-shaped stellar complexes at the northeastern edge of the Large Magellanic Cloud is the most thoroughly studied such feature (Figs. 1 and 2). It is located near the giant, gaseous LMC4 supershell, and includes four (and possibly five) giant arcs with radii 150–300 pc made up of high-luminosity stars and young clusters (Fig. 1). The image of the smallest of these arcs (the "Sextant"—see below) can be found on the World Wide Web at the "Astronomy Picture of the Day" site on the June 25, 1995 and August 23, 1997 pages. An ultraviolet image can be found on the page of October 11, 1995 with the caption: "The reason the arc has the observed shape is currently unknown."

The most conspicuous of these arcs was first noted in 1966 by Westerlund and Mathewson [9], who attributed the origin of both this arc and the LMC4 hydrogen cavity to the explosion of a hypothetical super-supernova, citing Shklovskiĭ [7]. The HI distribution maps available at that time had low resolution, leading to the conclusion that the giant stellar arc closes the hydrogen cavity from the south, and originated on the side of the cavity with the highest density of ambient gas. In reality, however, this arc resides deep inside the LMC4 cavity (Fig. 2). Westerlund and Mathewson [9] identified this arc of bright blue stars with Shapley's "Constellation III." However, they overlooked several other arcs in the vicinity of this feature. Prior to 1998, the only work to mention the existence of these arcs was a brief paper by Hodge about "a super-supernova remnant in NGC 6946," in which he presented a schematic of "Constellation III" in the LMC and a somewhat similar feature in the spiral galaxy NGC 6946. Prof. Hodge informed us that this was the only such structure he found in his systematic searches for features resembling the system of stellar arcs in the LMC.

The region of "Constellation III" became the subject of numerous studies treating it as a classical example of a region of propagating star formation (see references in [13]). However, no further reference was made to the presence in the same region of several giant arcs of stars and clusters, shown in one of the figures in Hodge's [10] paper! Efremov and Elmegreen [13] were the first to point out the problem of the origin of this remarkable system of arcs, in 1998. Incidentally, we discovered that it is incorrect to assign the name of "Constellation III" to the arc of blue stars (also known as association LH77) described by Westerlund and Mathewson [9]. This name was first given to the $28' \times 28'$ region surrounding the cluster NGC 1974 [14], and does not include the LH77 arc, which we called the Quadrant. However, NGC 1974 is located in a smaller arc, called the Sextant [13]. Bok *et al.* [15] were the first to point out the arc-like shape of this feature, whose components include the clusters NGC 1955, NGC 1968, and NGC 1974.

The regular, circular shapes of these two arcs were explained as a consequence of their formation from

gas swept up by the pressure of O stars and supernovae possibly residing at the arc centers, where the remnants of a sparse association (for the Quadrant) and a small cluster (for the Sextant) were found. Up to several dozen supernovae would have to have exploded to release a total energy of the order of 10^{52} erg, required to produce shells from the swept-up gas with the observed sizes of the Quadrant and Sextant arcs and the ages inferred from the star clusters they contain [13].

Later, Efremov [5] and Efremov and Elmegreen [16] pointed out the logical flaws of this hypothesis. It is unclear why such unusual features as arcs should have formed around such inconspicuous clusters while being absent around a great many richer clusters with appropriate ages. It is even much more difficult to understand why all the giant stellar arcs known in the LMC are located near each other within a 1.5 kpc region, which, in addition, contains the largest hydrogen cavity in the LMC. One cannot avoid the conclusion that the formation of the entire system of arcs was brought about by some unique phenomenon.

The photometric data of Braun *et al.* [17] failed to confirm the existence of a stellar grouping with an age appropriate for the formation of the arc in question near the center of the Quadrant. They suggested that the entire star-forming region, including LMC4, formed as a result of gas-dynamical interactions between the gas of the Milky Way and gaseous clouds located at the leading side of the LMC as it moves through the halo. However, Braun *et al.* [17] say nothing about the possible origins of the formation of such specific features as stellar arcs.

Efremov and Elmegreen [13] found that the age and radius of the Quadrant are 16 Myr and 280 pc, and those of the Sextant are 7 Myr and 170 pc. These parameters enable estimation of the final expansion velocities of the arcs based on the differences in their radii and ages, without invoking theoretical assumptions about the formation mechanism. The resulting velocity is (280–170) pc/(16–7) Myr = 12 pc/Myr $\approx$ 12 km/s, which agrees reasonably well with the values implied for each arc by the theory of triggered star formation in swept-up gaseous shells [13]. The stars in the arcs maintain the expansion velocity of their parent gas shells, which naturally depends on the initial density of the gaseous medium, so that the suggestion that the expansion velocities of the two arcs are the same can be correct only to first approximation.

A possible fourth arc in the eastern region (Fig. 1b) has a radius of about 500 pc, implying an age of about 40 Myr for a velocity of 12 km/s. However, the reality of this arc is in doubt. We know the ages of only two clusters located in this arc, and their mean age is 125 Myr. It is important that, despite its convincing appearance, the reality of the third arc is also subject to question. The dispersions of the ages and radial velocities in this arc are high, and the structure may be superimposed by unrelated groupings. However, the existence of the fifth arc, which we overlooked in

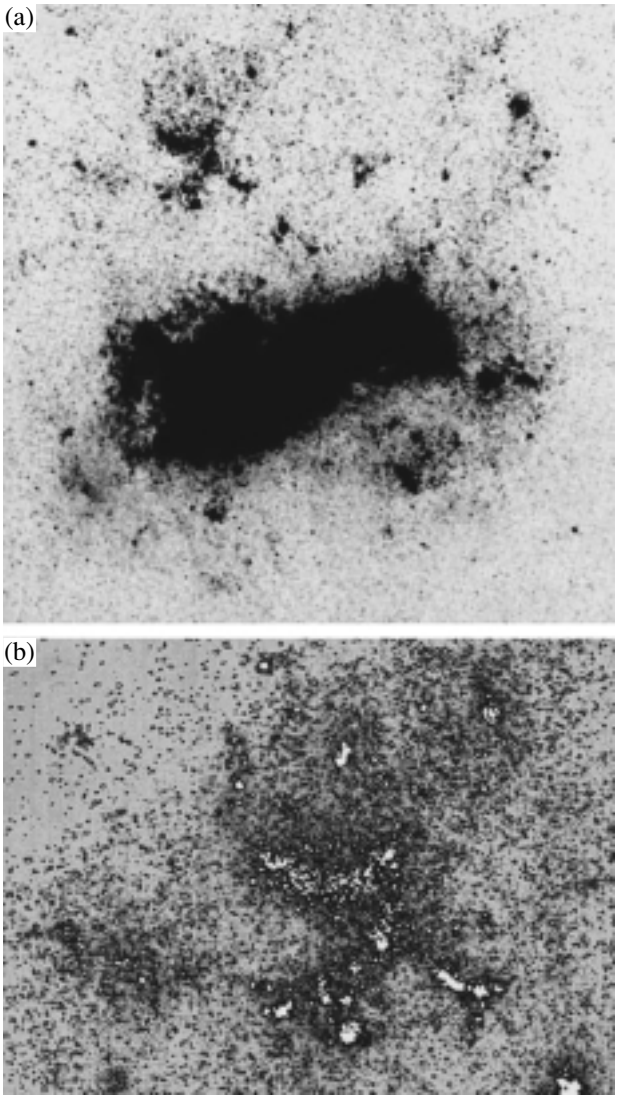

Fig. 1. Giant stellar arcs in the LMC. (a) Position of the system of arcs in the galaxy. A region of enhanced density of high-luminosity stars can be seen north and northwest of the Quadrant. It is bounded from the east by the fifth arc. (b) The LMC4 region with the Quadrant in the center and the Sextant, the third, and the fifth arcs located southwest, south, and above the eastern tip of the Quadrant, respectively. The fourth arc, possibly an artefact, is located to the southeast. The cluster NGC 1948 is to the northwest. The regions of the highest stellar density are shaded white. (The initial photograph was kindly provided in electronic form by P. Hodge and K. Olsen.) See Fig. 2 for scale. Throughout, north is up and east is to the left.

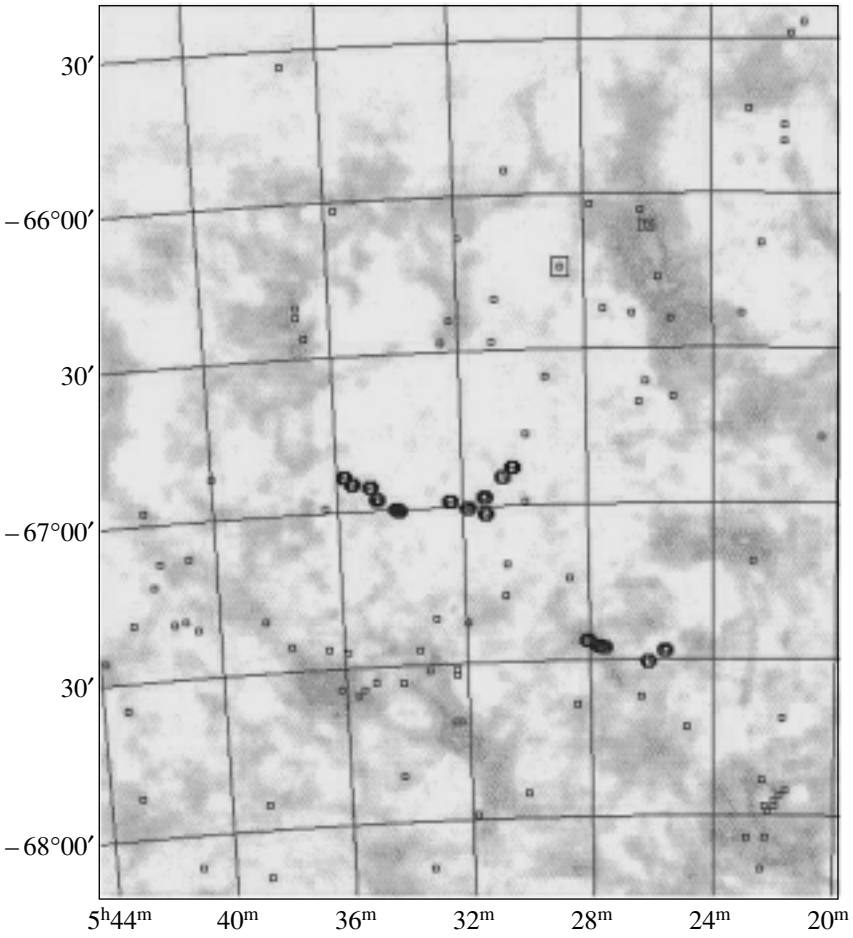

Fig. 2. Star clusters with available integrated *UBV* photometry (small squares) and an HI map of the LMC4 region (according to the data of Kim *et al*. [24]). The circles indicate clusters of the Quadrant and Sextant arcs. The large squares indicate the cluster NGC 1978 (larger square) and the supernova remnant N49 (smaller square). 1° = 900 pc. The coordinate grid corresponds to the equinox of 2000.0.

our previous works, is beyond question. It is shown in one of Hodge's [10] figures, and the unresolved background that surrounds it also has the shape of an arc (Fig. 1b).

One way or another, stellar arcs become less prominent as they grow older, due to the decreasing luminosities and density of their stars. Of course, arcs are not gravitationally bound formations.

It is easy to see that both the Quadrant and Sextant are fragments of regular circles (Figs. 1b and 3). Given the fairly large inclination of the plane of the LMC of about 33°, this implies that both arcs are parts of spherical shells seen in projection. There is no question that the Sextant circle cannot be described by an ellipse corresponding to the inclination of the LMC. The width of the gaseous disk of the LMC (about 200–300 pc) is smaller than the diameter of the Sextant, let alone the diameter of the Quadrant, making the overall situation unclear. It appears that stars in shells form before the initial gaseous shell breaks through the gaseous disk of the galaxy and that the stellar shell maintains the decreasing expansion velocity of the initial gaseous shell.

The hypothesis that the arcs are segments of spherical shells seen in projection can be verified by determining the number density of early-type stars: if the hypothesis is true, this density should decrease more slowly toward the arc centers of curvature. Preliminary estimates based on the Sextant image obtained with UIT are consistent with this pattern. This idea is also supported by a comparison of a direct image of the Quadrant and a model spherical segment filled with randomly distributed points, with a thickness 0.2 times its radius, a central opening angle of 130°, and the central radius vector viewed at an angle of 10° to the plane of the sky (Fig. 3).

Such an orientation, together with the large sizes of the partial shells, which are close to the thickness of the gaseous disk of the LMC, are already sufficient to explain the lack of arcs symmetric with respect to

their centers of curvature. The absence of such arcs could, in principle, be explained if the central source of pressure is beyond the gaseous disk of the galaxy; however, in this case, the arc apices should point either toward or away from the intersection of the plane of the sky and the plane of the LMC [18], which is true only for the fifth arc (Fig. 1a). The apparent shape of the resulting stellar grouping should depend not only on projection but also on possible anisotropy of the initial energy release and local inhomogeneities in the interstellar medium. It is obvious that in this case the groupings should not always be arc-shaped in projection and could also be round, with no concentration toward the center. One possible example of such a grouping is the young cluster NGC 1948 (located in the northwestern part of the LMC4 region) and the surrounding association, which is characterized by a small age spread (Fig. 1a).

Thus, we must explain why all the arcs in the LMC are concentrated in a single region. An oblique impact of a group of clouds could, in principle, explain this pattern and the similar orientation of the Quadrant and Sextant arcs. However, the orientations of the third and fifth arcs are completely different. Braun *et al.* [17] argue strongly against the idea that the specific features of the LMC4 region were formed by impacts of high-velocity clouds. The substantial spread in the arc ages is difficult to reconcile with the hypothesis of an impact of a group of clouds. Finally, no perturbations in the HI velocity field are observed in the vicinity of the Sextant (there is no hydrogen around the Quadrant); such perturbations were detected only near the supernova remnant N49, far from both arcs (Fig. 2).

The observed characteristics of the Sextant arc can be explained by either a single powerful explosion or continuous energy output from a center located near the edge of a dense cloud; the nearly equal distances between clusters could be interpreted as the result of the development of gravitational instability in the gaseous shell [18]. However, it is difficult to imagine that all such phenomena in the LMC occurred only at the edges of dense clouds. An isotropic explosion at a large height above the symmetry plane of the gaseous disk would also produce a one-sided arc; however, as pointed out above, in this case, the line connecting the center of the arc with its center of curvature should be perpendicular to the intersection of the plane of the galaxy and the plane of the sky, in conflict with the observed orientations of all but the fifth LMC arcs. Note that the hypothesis of an explosion away from the plane of the galaxy makes it impossible to explain the arcs as the result of multiple supernova explosions, since sufficiently young clusters are concentrated toward the plane of the galaxy.

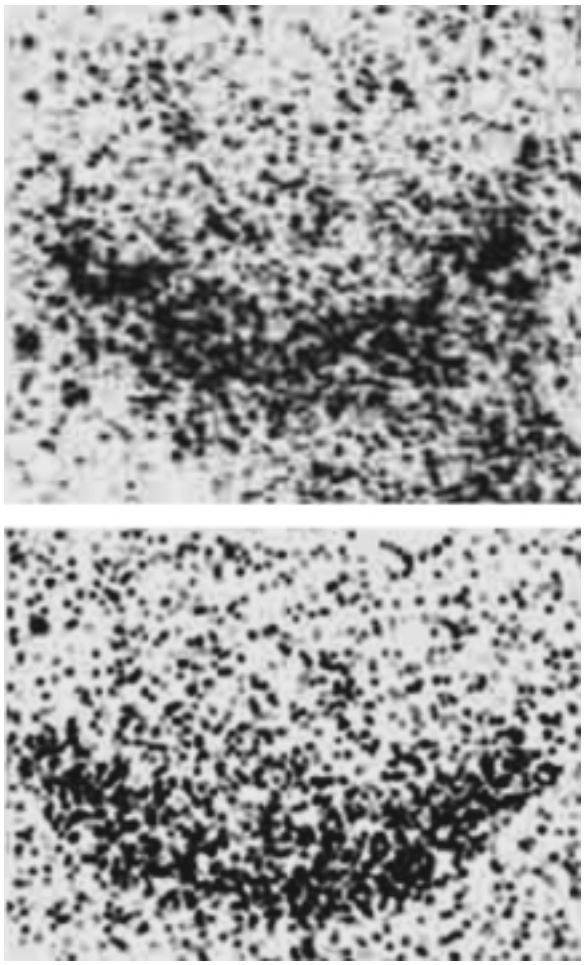

Fig. 3. Top: the Quadrant arc. Bottom: model of a spherical segment whose thickness is 0.2 times its radius with an opening angle of 130° and the central radius vector inclined by 10° to the plane of the sky.

Thus, neither cloud impacts nor multiple supernova explosions can explain the origin of giant stellar arcs in the LMC. At the same time, their spherical symmetry is not the only evidence that the arcs were formed by a powerful central energy source that triggered synchronized star formation. The age spread of the clusters in the Quadrant is less than the observational errors, but one of the clusters in the Sextant arc—NGC 1974—appears to be younger than the other clusters. Braun *et al.* [17] consider this fact to be in conflict with the possibility of star formation triggered by a central source of pressure; however, the smaller age of NGC 1974 could be due to the higher gas density at the western end of the Sextant arc (Fig. 2), which could accelerate the star-formation process.

Another important fact that has so far received little attention is the small age dispersion within each cluster in the arcs. Such data are available only for

the Sextant and Quadrant (LH77). Oey and Smedley [19] found that the spread in the ages of OB stars in the associations LH51 and LH54 in the Sextant is only 2–3 Myr. Dolphin and Hunter [20] give ages of 16^{+6}_{-4} Myr and 12^{+4}_{-4} Myr for the westernmost edge of the Quadrant (LH77) and the cluster NGC 2027 near the easternmost edge of the Quadrant, respectively. For two clusters in the same Quadrant arc—SL 538 and NGC 2006—Dieball and Grebel [21] give ages of 18 and 22.5 Myr, respectively, with a spread of 2–2.5 Myr. It goes without saying that this spread includes all random errors. The data of Braun *et al.* [17] also indicate that the spread in the ages of stars and clusters in the Quadrant arc is smaller than the errors of the ages themselves. None of the above authors noted that the clusters they were studying are parts of rather peculiarly shaped structures...

Everything indicates that the formation of star clusters in these arcs was triggered and synchronized by some external factor. This makes arc-shaped stellar complexes an ideal tool for studying the initial luminosity function of triggered star formation, especially for verifying the long-debated assumption that there is a deficiency of low-mass stars in this mode of star formation [22, 23].

The regular, round shapes of the arcs also clearly indicate that their parent clouds formed from gas swept up by some central source of pressure and that they did not existent prior to this. It is difficult to understand the suggestion of Braun *et al.* [17] that the arcs owe their geometry to the structure of clouds that existed long before the stars formed and not to a process that resulted in both this cloud geometry and the star formation occurring in the clouds. In the picture of Braun *et al.* [17], the natural question of what could produce such a peculiar and dynamically unstable cloud structure remains unanswered.

It first seemed to us that the unique stellar arcs in the LMC owe their regular shape to the fact that they are located in a region of very low and apparently uniform hydrogen density, so that the swept-up gaseous shell acquires and maintains a regular shape. However, new data about the HI distribution in the LMC [24] have shown that, although the Quadrant resides deep inside the LMC4 cavity, the Sextant is located in a region of high gas density (Fig. 2).

There is the impression, as suggested in the first studies of the LMC4 region [9, 10], that the stellar arcs were produced by some event with an energy output far higher than that of common supernovae. However, no-one has explained why an entire system of arcs formed in a single region of the galaxy. In our view, the only natural explanation is that the parent objects of the arcs formed in some nearby unusual star cluster, and were subsequently ejected from the cluster. Such a cluster—NGC 1978—does exist, and objects that were ejected from it and then exploded can be identified with the progenitors of gamma-ray bursts [5, 16, 25, 26].

3. PECULIAR STELLAR COMPLEXES IN M83

In July 1998, we noted an isolated stellar complex on the outskirts of M83, 3′ southeast of the galactic nucleus on a photographic image of the galaxy obtained on an Australian 4-m telescope and hanging in the library of Dominion Astronomical Observatory in Victoria. This complex contains two small arcs of blue clusters. The presence of these arcs, the complex's overall shape, and its isolated position in the galaxy make this southeast complex similar to the complex of stellar arcs in the LMC (Fig. 4). A brief description of this complex and its coordinates are given in [5]. Our three attempts to include this complex in an HST observing program (1998–2000) were unsuccessful, and, in the meantime, it was independently discovered on an image taken with the 8-m VLT telescope in March 1999 by Comeron [27], who reported the discovery in his paper entitled "A Gould-Belt-like Structure in M83." However, the two structures are actually not very similar, since the complex of the Local System (Gould's Belt) is not isolated, being part of the Cygnus–Orion spiral arm, and has fewer young and relatively rich clusters than the complex in M83.

Based on the lack of HII regions and of any apparent distortion of the shape of the southeast complex due to galactic shear, Comeron [27] estimated its age to be a few tens of millions of years. Larsen [28] kindly informed me in a letter of June 30, 2000 that his UBV photometry of six clusters in this complex implies ages of 18 and 19 Myr for the two brightest clusters, while the cluster at the northern edge of the larger (northern) arc is 32 Myr old. It is important that the smaller (southern) arc in the southeast complex consists of fainter clusters and is located in a rather dense region of the complex, bringing its very identification into question; however, the clusters of this arc stand out due to their blue colors, and should therefore be young.

We consider the two other arcs of clusters in M83 below. Figs. 5a shows the positions of peculiar stellar complexes in M83 and Figs. 5b–5e present detailed images. We draw the reader's attention to an isolated oval structure with enhanced surface brightness in the southwestern part of M83 (Fig. 5c), bordered by several bright star clusters. This could be a shell-like structure with most of its objects located on a spheroidal surface. On the whole, this complex is similar to Hodge's object in NGC 6946 and differs from the latter only in its lower brightness and less regular outline.

4. A PECULIAR COMPLEX IN NGC 2207

Recently, Elmegreen *et al*. [29] discovered several small arcs of clusters inside a bright cone with a bright cluster at its vertex in the interacting galaxy pair NGC 2207/IC 2163, near the western edge of NGC 2207. The coordinates of this cluster coincide with those of a 20 cm synchrotron source considered earlier to be a background radio galaxy. The cluster also has a dark cone emerging from it in to southwest. This cone abuts on the more extended bright cone emerging to the southeast. The arcs located closer to the central cluster are inside the bright circle. The feature as a whole is quite mysterious. The absorption in the dark cone is close to neutral, suggesting a large optical depth [29] or unusually large sizes for the dust grains in the cone. The bright collimated emission of the central source can be explained in one way or another, but it is quite unclear how to understand its position at the vertices of the bright and dark cones.

5. OTHER MULTIPLE ARCS?

The structure that Hayward [6] found in the galaxy NGC 7741 appears to be a real group of three to five arcs extending over several kiloparsecs. As is evident from the image of Larsen [28] made using the 2.5-m Nordic Optical Telescope, the two short arcs are located symmetrically near a bluish, diffuse object, which is very likely the richest young star cluster in the galaxy. These arcs appear to be enclosed concentrically by another giant ring adjacent to another ring to the north.

Dirsch *et al*. [30] point out several shell-like structures of stars and clusters in the irregular galaxy NGC 3664, with five clusters equally separated by about 600 pc. This case may be similar to that of NGC 7741. The galaxies also bear some similarity to each other, being classified as SB and SBm systems, respectively.

6. SPHEROIDAL STELLAR COMPLEX IN NGC 6946 (HODGE'S OBJECT)

As mentioned above, this was the only object that Hodge [10] found in his search for structures similar to the arc system in the LMC. The circular region of enhanced surface density has a diameter of about 20″. The complex has a sharp and regular-shaped circular outer edge covering an angle of about 270°, along which there are short arcs of cluster; another arc is located very near the complex to the southeast (Fig. 6).

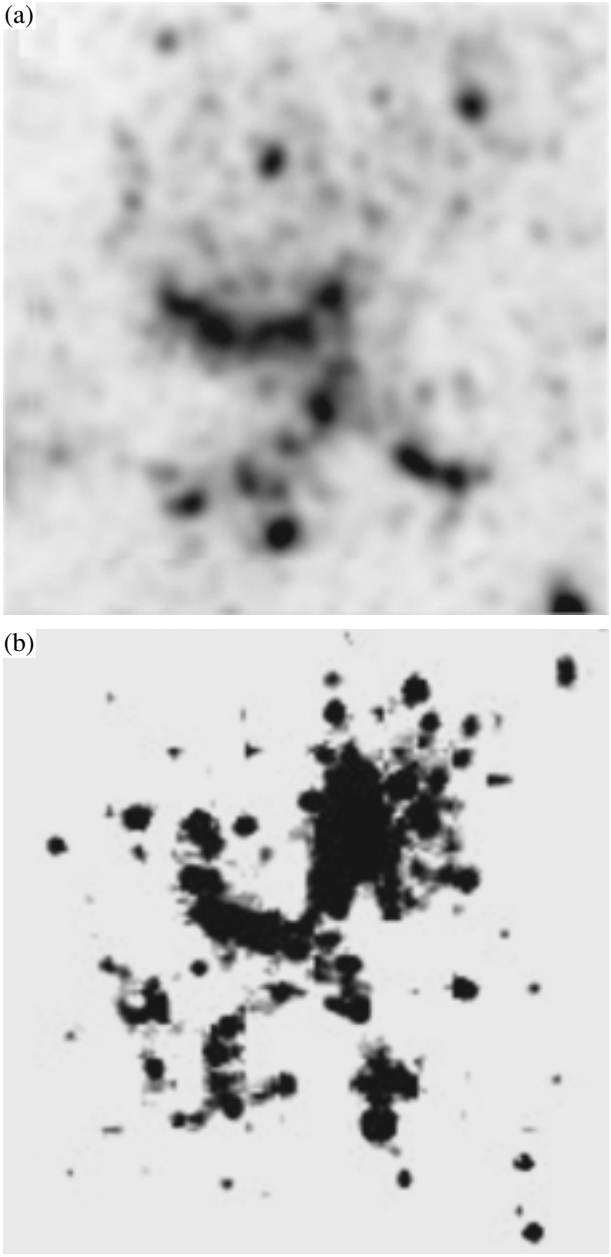

Fig. 4. Two systems of giant circular arcs. (a) The LMC4 region shown with decreased resolution; (b) the south-eastern complex in M83 (a fragment of an image taken with the 8-m VLT telescope of the European Southern Observatory).

This feature was independently rediscovered by Larsen and Richtler [31] while searching for young, massive clusters in spiral galaxies, who described it as a bubble filled with star clusters dominated by a giant, young cluster. Efremov [5] noted a diffuse object on plates taken with the 6-m telescope at the Special Astrophyiscal Observatory and suggested it could be

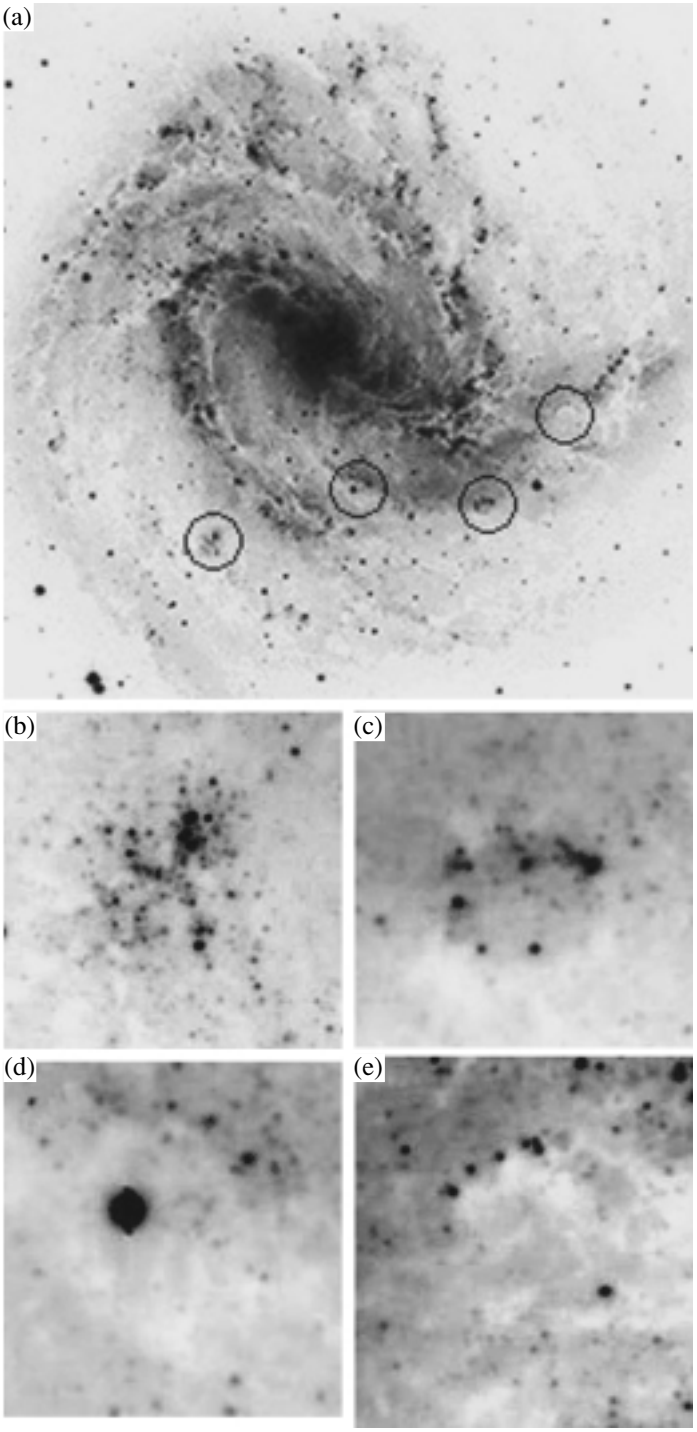

Fig. 5. Peculiar stellar complexes in M83 (fragments of an image of the galaxy taken with the 8-m VLT at the European Southern Observatory). (a) Positions of complexes within the galaxy. Circles indicate (left to right): the southeastern complex, southern ring, southwestern complex, and western ring; (b) the southeastern complex; (c) the southwestern complex; (d) the southern ring, and (e) the western ring.

a massive cluster inside Hodge's object; indeed, this object proved to be a very giant cluster, subsequently rediscovered by Larsen and Richter [31].

In their later more detailed study of this cluster and the surrounding complex, Elmegreen *et al*. [32] noted about 20 nearly coeval smaller clusters with ages of about 15 Myr inside this complex. The complex has a sharp outer rim to the north, west, and south, with

a remarkably regular shape, forming an ideal circle extending over three-quarters of the boundary of the complex. The complex diameter is about 600 pc, which clearly exceeds the thickness of the galactic HI disk. Its circular shape (not elliptical, as it should be according to the inclination of galaxy to the plane of the sky) seems to imply that it a sphere rather than a circular ring in the plane of NGC 6946. The complex can have a diameter greater than the disk thickness only if its progenitor expanding gaseous shell broke up into individual stars before its diameter reached the thickness of the gaseous disk. In this case, the sharp outer rim on the north, west, and south sides of the complex can be interpreted as the projection of the boundary of a shell-like structure of young stars and clusters.

The alternative is to suppose that this boundary simply outlines a region cleared of dust by the radiation of OB stars in the brightest young cluster, and that the absorption increases sharply beyond this region [32]. However, images of the stellar complex do not show it to be surrounded by a region of strong absorbtion; there is a small, dark region only in one small area beyond its northeastern boundary (Fig. 6). The complex owes its brightness to the contribution of its clusters and unresolved, high-luminosity stars to the normal stellar field of the galaxy. In this case, however, the very circular shape of the complex boundary demonstrates that we are dealing with a region of star formation triggered by a central source.

However, like in the LMC, no object associated with the inferred central source of pressure could be identified. One supergiant cluster seems a natural candidate, but its age is the same as those of the other complex clusters [32], and it is offset from the center of curvature of the complex boundary. If this cluster were at least about ten million years older than the smaller clusters, the explosions of its most massive stars could possibly have triggered star formation in the swept-up gaseous shell.

HST photometric data and an estimate of the velocity dispersion of the stars in the central cluster based on observations made with the Keck telescope yield a mass of $10^6 M_\odot$ and a central density of about $10^4 M_\odot/\mathrm{pc}^3$, close to typical values for the most massive classical (old) globular clusters [33]. If this cluster has a normal luminosity function, its most massive stars should have masses of about $100 M_\odot$, and such stars can produce super-powerful hypernova explosions if they are rapidly rotating (such objects are thought to be candidate progenitors of gamma-ray bursts [34]). Moreover, stellar coalescence events should occur in such dense and young clusters, which should result in the formation of supermassive and rapidly rotating stars or black holes with masses of several hundred solar masses [35, 36]. Furthermore, the results of recent computations of the dynamic evolution of clusters show that 10–50% of the most massive stars should be ejected within 10–50 Myr to distances exceeding twice the tidal radius of the cluster [37] and that explosions of hypernovae ejected from the cluster could explain the off-center position

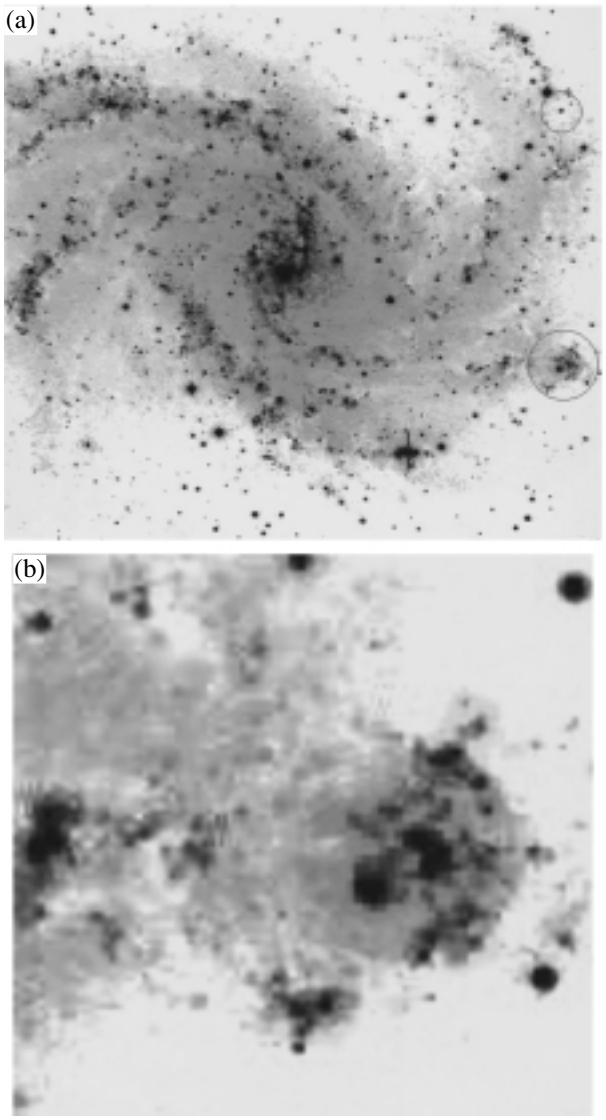

Fig. 6. Spheroidal stellar complex in NGC 6946 (Hodge's object). (The initial galaxy image was obtained by S. Larsen with the 2.5-m Nordic Optical Telescope of La Palma observatory. (a) The position of Hodge's object (bottom right) and the dark circle in the same galaxy (top right). (b) Hodge's object. Star clusters are located in the region of enhanced brightness in the unresolved background bordered on the north, west, and east by a regular semicircle. The giant young cluster is shifted to the southeast of the center of the complex.

of the young globular cluster in the circular complex and the presence of arcs of star clusters.

This hypothesis about the origin of Hodge's complex will be supported if smaller clusters prove to be younger than the central cluster. The origin of the central cluster also poses a problem. Its luminosity of $M_V = -13$ makes it one of the brightest young globular clusters, outshone only by several clusters in the interacting galaxy pair NGC 4038/4039. However, such clusters have so far been found only in interacting galaxies, near the centers of spiral galaxies with active star formation (like NGC 253), or in starburst galaxies like NGC 1569, NGC 1705, and M82 [38]. The causal link between the origins of the central cluster and of the entire complex seems beyond question; however, strictly speaking, even the direction of this link remains unclear. The high pressure in the interstellar medium inside the complex could result in the formation of a massive, gravitationally bound cluster, very like the situation Elmegreen and Efremov [39] proposed for classical globular clusters. However, what could have caused such a high pressure within a clearly delineated region at the outskirts of a quite normal galaxy (albeit with a high star formation rate)?

In the recent past, all galaxies containing young, massive, compact clusters should have undergone encounters with other galaxies involving collisions of their gaseous clouds. Radio observations of NGC 6946 revealed HI clouds moving with velocities differing by 45 km/s from the galactic rotation velocity and with masses as high as $10^7 M_\odot$ [40], suggesting that a collision of such a gaseous cloud with the galactic disk is quite possible. This event could have led to the formation of all the clusters of the complex, although the regular spherical shape of its boundary is difficult to explain in this way. Note that the complex is not associated with holes in the gaseous disk of the galaxy, although some such holes are located fairly close to it [40].

One way or another, spectroscopic observations of the complex made with the 6-m SAO telescope have shown that the radial velocity of its central cluster (150 km/s) and of HI regions in its vicinity might somewhat differ from those of surrounding HII regions. An HII shell with a diameter of about 300 pc centered about 200 pc east of the central cluster was also detected; it is expanding at about 100 km/s. The data also show spectral evidence for shocks. Some sources of pressure are still active in the complex, although it appears to be devoid of young supernova remnants. The age of the central cluster was estimated to be 13 Myr based on the intensity of Balmer absorption lines in its integrated spectrum [41].

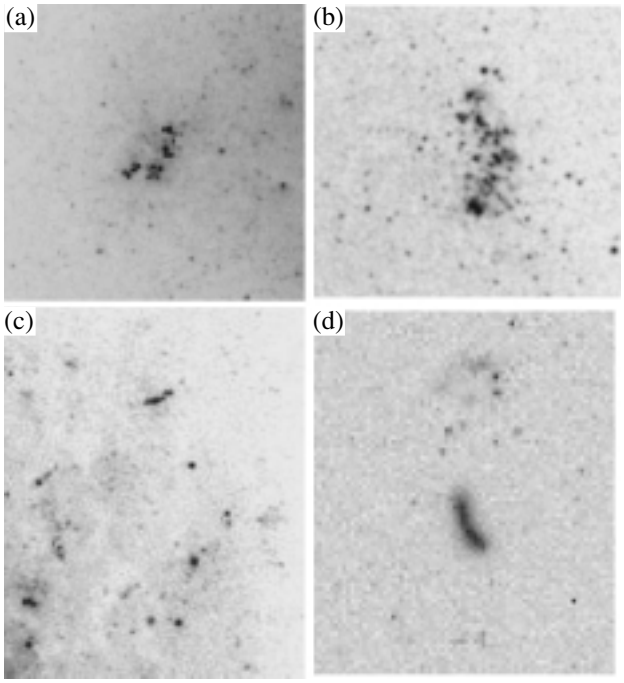

Fig. 7. Single isolated cluster arcs: (a) giant arc of young clusters in NGC 300 embedded in an HII region (image taken by S. Larsen with the Nordic Optical Telescope of La Palma observatory); (b) isolated stellar association HS137 in the northwestern part of M33; (c) possible arc of star clusters in the northern part of NGC 7793; (d) a strange arc in NGC 2451 (an arc-shaped background galaxy?). (Image adopted from the HST archive.)

7. CIRCULAR SHARP-RIMMED COMPLEXES

There are other stellar complexes with round and sharp outer edges, albeit not as ideally circular as in the case of the complex in NGC 6946. We also found a structure 30″ in diameter located 3′ to the south of the center of M101, which is very reminiscent of Hodge's [5] object if observed with low resolution. This similarity is maintained at higher resolution, although the outlines of the complex become less regular. Images from the HST archive show that although the southern boundary of the complex exhibits a regular arc of clusters with an opening angle of 80° it is not ruled out that the complex is bordered on the west and east by regions of higher absorption. Near its northern boundary, there is a young, rich double cluster surrounded, like the central cluster of Hodge's complex, by a region with a very high density of smaller clusters and high-luminosity stars [42].

We also found circular structures with sharp outer edges near the western edge of M83 (Fig. 5c) and in the northern part of NGC 1232 by inspecting VLT images of these galaxies. A circular feature in M31

with a diameter of 0.6′ (120 pc) located inside the association OB 59 near the dark cloud D474 is similar. It is conspicuous in chart 10 of Hodge's atlas [43]. This feature includes compact clusters and high-luminosity stars. Its axial ratio would be 1 : 4 if it were a disk in the plane of the galaxy.

It is important that when observed with low resolution such small circular complexes in distant galaxies are indistinguishable from bright foreground stars (see, especially, the complex in NGC 1232 in the atlas of Sandage and Bedke). It is, therefore, possible that such objects are not all that rare.

The sharp outer edges of such features indicate convincingly that their constituent stars and clusters are mostly located on a spheroidal surface. This, in turn, clearly indicates that they were produced by some source of pressure located near their centers of curvature. However, we must make certain that this boundary cannot be due to an abrupt increase in absorption beyond the boundary of the complex.

8. SINGLE ARCS OF STARS AND CLUSTERS

Several single arcs of stars and star clusters are also known. The young clusters NGC 1962, NGC 1965, NGC 1966, and NGC 1970 in the LMC, which make up the isolated association LH58, outline a wide arc covering 180° with a diameter of about 50 pc. In their study of this association, Garmany *et al.* [44] concluded that most of its stars formed simultaneously several million years ago. The even younger cluster NGC 2074 (LH101) in the LMC has a similar arc-like shape with a diameter of about 30 pc. No conspicuous objects could be found at the centers of either arc [45].

A bright, arc-shaped complex about 500 pc across with an opening angle of about 160° was found in the spiral galaxy NGC 300. It consists of four groups, each made up of four or five objects, all star clusters, judging by their brightness and sizes (Fig. 7a). The complex must be very young, since it is embedded in an HII-region. This wide arc, like LH58, is representative of objects that are, in some sense, intermediate between circular complexes and single stellar arcs.

Vader and Chaboyer [46] found a giant arc of young clusters with a radius of 3 kpc located 11 kpc south of the center of the spiral galaxy NGC 1620. They point out that the peculiarity of this arc is that it consists of star clusters (rather than gas) and has a rich, young cluster at its center, possibly somewhat older than the clusters in the arc. Vader and Chaboyer [46] conclude that 400 to 6500 supernovae exploding in this cluster could have produced a swept-up gaseous shell, which, after expanding to a radius of 0.5–1.0 kpc, became gravitationally unstable, resulting in the onset of star formation. The asymmetry of the arc's surface-brightness distribution (which covers 220° in the ultraviolet) may reflect the radial gradient of the gas density in the disk of NGC 1620, with the bends in the arc being due to inhomogeneity in the gas distribution in the vicinity of the central cluster. Vader and Chaboyer [46] also suggest that the supernova explosions ended at least 5×10^7 years ago, so that the inner part of the gaseous bubble they inflated have had time to cool and the corresponding HI void has disappeared.

The stellar association HS137 occupies an isolated position in the northwestern region of M33 [5]. This association is part of an arc covering about 90° with a radius of 44″, or about 160 pc (Fig. 7b). Determining the ages of its constituent stars and clusters is an important and observationally feasible task.

The reality of small, individual arcs of clusters located in regions with a high density of the resolved background and unaccompanied by dark regions with a corresponding morphology remains open to question. Such arcs, especially short ones, may be numerous and real; however, only a similarity of the ages of their constituent clusters can be considered proof that the arcs are not chance configurations. In the absence of age data, the isolated position of a particular arc can be taken as evidence for a physical association between its constituent objects. Short arcs with several adjoining clusters have been found in NGC 300 and NGC 7793 (Fig. 7c), however, these could be chance configurations. Note also that if such arcs were planar features, i.e., fragments of circles, they should be seen as arcs only if viewed at a certain angle, with short arcs being especially difficult to identify.

The short, the bright arc in the spiral galaxy NGC 2451 that we noted on the HST image is of great interest [47]. This is the only object of that kind that we found by systematically inspecting galaxy images published in a series of papers devoted to an HST search for extragalactic Cepheids. The high surface density of this arc seems to be inconsistent with the idea that it is a peculiar background galaxy. At the same time, this arc shows no signs of being resolved into individual stars (Fig. 7d), which would be unusual for a young stellar grouping in NGC 2541 (stellar arcs can never be old).

The entire 3 kpc irregular galaxy DDO165 is sharply bounded from the south by a regular, circular arc (Fig. 8). Is this really a fragment of a spherical shell seen in projection, with the entire galaxy having the shape of a thick-walled bowl? If this is the case,

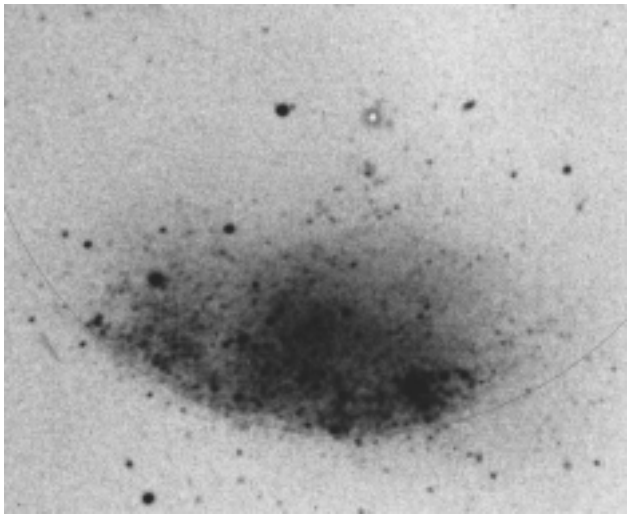

Fig. 8. Irregular (!) galaxy DDO 165 bounded from the south by a regular circular arc (image taken by I.D. Karachentsev with the 6-m telescope of the Special Astrophysical Observatory).

we must assume that the parent event involved the entire galaxy, or even (if all stars of the galaxy prove to be equally young) occurred in an isolated intergalactic HI cloud. In any case, the origin of such a regular and sharp boundary for an entire galaxy is very interesting. Could the arc in NGC 2541 described above be another example of such an arc-shaped galaxy?

9. THE PROBLEM OF DARK CIRCLES

We found two very interesting arcs with equally spaced clusters enclosing dark circular regions in M83 [5]. One of these, which includes four clusters spanning an arc of 60°, is located in a secondary spiral arm to the south of the galactic nucleus (Fig. 5d). It contains a bright, starlike object at its very center, which is most likely a foreground star. If this is the case, it is rather strange that the star, which is second in brightness among the few foreground stars projected onto the central region of M83, is found exactly at the center of one of the small dark rings in the galaxy. The radius of the southern ring is about 16″, and the ages of the three clusters at its northern edge are from 30 to 50 Myr [28]. Another arc of five clusters, one of which is triple, covering an angle of 70°, borders a dark ring of radius 14″ located at the western edge of M83; there is nothing in the center of the circle. Its darkest regions form a wide, scalloped arc adjacent to the cluster arc on the inside (Fig. 5e). On the opposite side, there is another cluster with about the same brightness and color as the arc clusters. As expected, the arc of clusters is located on the side of the ring that adjoins the brighter region toward the center of the galaxy, where the gas density is obviously higher.

For a distance to M83 of 4.8 Mpc, the radii of the rings are 240 and 380 pc, respectively. The western ring in M83 is a regular circle and the southern ring is elongated (Figs. 5e, 5d). The equidistant cluster spacing, which is immediately apparent in the western ring (Fig. 5e), is less pronounced in the southern ring. A similar dark ring is present in the northern corner of the irregular galaxy NGC 4449; it is bordered on the north and west by young star clusters, and there is nothing at its center. The reduced surface brightness inside this ring is confirmed by objective photometric data: the ring is immediately apparent in the galaxy isophotes [48].

We found a dark, regular, circular ring with a rather bright and slightly diffuse object at its center in the galaxy NGC 6946 located 3′ from the galaxy center. The position of this feature is indicated by a circle in the upper right-hand corner of Fig. 6a. This ring is bordered on the west by faint objects, with a hint that they are equally spaced. The ring is located in a small fragment of the northwestern spiral arm and its diameter is about 500 pc. It contains not only a central cluster but also an HII region, and its surface brightness is appreciably lower than that of the surrounding galactic region.

Note that such circular regions with low surface brightness can be seen only in high-contrast images, and that they could be rather numerous. In our opinion, the nature of such regions remains mysterious. The surface brightness inside the rings is undoubtedly lower than in the surrounding region of the galaxy, and it seems quite natural to attribute this to stronger absorption inside the rings. However, the clusters bordering these regions can be understood only if they are formed from a gaseous shell swept up by a central source of pressure. The equidistant arrangement of the clusters suggests formation as a result of gravitational instability in a gaseous shell. However, in this case, it is difficult to understand how dust could be preserved inside this shell of swept-up gas. One possibility is that the radiation or explosion of the central source were not isotropic. High-resolution images are required to obtain more conclusive results.

The idea of alternating suppression and triggering of star formation by some central source of radiation whose spectrum changed in the past [5] does not save the situation, since it is not the lack of young objects inside dark rings that poses a problem, but their surface brightness, which is lower than the surrounding regions of the galaxy. Note that far from all other known stellar arcs are located around dark clouds.

As pointed out by Brand and Zealey [8], dark, circular rings around stellar complexes are common

features, and are obviously the results of an expulsion of gas and dust from central regions occupied by young stellar groupings. Such configurations are usually numerous; they form continuous chains along the spiral arms of gas-rich galaxies such as M83 and NGC 6946. However, only one such feature can be seen in M100, located not far from the galactic center.

10. CONCLUSIONS

The legitimate question now arises of whether such structures can be found in our own Galaxy. However, they are overall very rare and also extremely difficult to identify in the Milky Way. Since we reside in the plane of the Galaxy, we are unable to see stellar arcs as such, if they are planar formations. At the same time, partial spherical shells of stars and clusters are extremely difficult to identify among foreground and background objects, especially in the presence of nonuniform absorption. Conditions are more favorable for the identification of such features when the central source is located outside the Galactic plane. The most likely candidate is the regular arc of HII regions and young clusters in the Cas OB6 association, which is located somewhat above the Galactic plane. This arc includes, among other objects, the S201, W5E, W5W, W4, and W3 HII regions and the young star clusters IC 1805 and IC 1848. The convex side of the arc points toward the Galactic plane, and is clearly visible in Figs. 1 and 2 of Normandeau *et al*. [49].

The Local System (Gould's Belt) might be a Galactic analog of the peculiar stellar complexes considered in this paper. Gould's Belt shows obvious indications of expansion, and some authors have considered the possibility that it might have been produced by the impact of a gaseous cloud into the Galactic plane [27]. Note that the age of this system (about 60 Myr) is close to the epoch of mass extinction of the dinosaurs, and it is tempting to interpret this as indirect evidence that the Local Complex formed as a result of a powerful energy release due to a gamma-ray burst.

Let us summarize the results of our analysis. The presence of young stellar groupings in the vicinity of older ones is often attributed to triggered star formation. Systematic age gradients can provide more convincing evidence of this effect. However, only the alignment of stars and clusters along regular, circular arcs can demonstrate conclusively that these objects owe their origin not to spontaneous density fluctuations in the interstellar medium, but to some source of pressure that was once located at the center of curvature of the arcs.

The best studied arc-shaped and spheroidal complexes of young star clusters have the following characteristics.

(1) Their diameters range from 100 to 600 pc, with the regular, circular arcs of stars and clusters spanning angles of 40°–200°.

(2) As a rule, they are isolated in their galaxy, and are usually located somewhere in its outskirts.

(3) The clusters within each particular arc have similar ages.

(4) Clusters in larger arcs are older.

(5) Clusters in arcs are often equally spaced.

(6) The outer arc boundary is often rather sharp and has the shape of a regular, circular arc, independent of the inclination of the galactic plane with respect to the line of sight.

(7) There are systems of multiple arcs of young clusters.

It is difficult to imagine any scenario for the origin of these features in which they are not formed from shells of gas swept up by some source of pressure, with the subsequent development of gravitational instability. If this hypothesis is true, the origin of arc-shaped stellar complexes is connected with the question of the origin of such shells, which must have been produced by some source of pressure near their centers. The nature of this source remains obscure, however. A central cluster that could harbor O stars and supernovae that produced the gaseous shell is usually lacking, and the possibility that the source is associated with impacts of massive gaseous clouds into the galactic plane has problems of its own. It is also difficult to explain the very regular circular shapes of a number of stellar arcs, which appear to be insensitive to inhomogeneities in the interstellar medium. These extremely circular shapes bear little resemblance to those for well-known examples of star formation in gaseous shells swept up by central sources of pressure, for example, in IC 2574. We also do not understand the origin of dark rings and arcs surrounded by arcs of star clusters.

The only way to explain the presence of several neighboring arcs is to suppose that their progenitors formed in a single peculiar star cluster, implying the existence of stellar objects with explosions an order of magnitude more powerful than those of individual supernovae. These same objects should give rise to gamma-ray bursts. Contrary to conventional views, only the most massive clusters with frequent or extremely powerful supernova explosions seem to be capable of producing HI supershells. Otherwise, it is not possible to explain the absence of supershells around numerous clusters, which, according to existing theories, should be capable of producing them. Recall that at least half of Galactic O stars have no Stroemgren zones, so that the absence of shells cannot be attributed to a lack of gas.

The presence of star clusters in shell structures provides extremely important information about the physical conditions in the initial gaseous shells and their ages, making them a sort of Rosetta Stone, potentially enabling us to decipher the nature of the central source of energy. In any case, these clusters are the best available laboratory for studying triggered star formation.

We will analyze the origin of arc-shaped and spheroidal stellar complexes in a future paper [50] and mention here only one more possibility. The regular, circular shapes of giant stellar arcs are difficult or impossible to explain if they are formed from gas swept up by a central source of pressure, since this requires the density distribution of the interstellar medium to be uniform on scales of several hundred parsecs. However, this same regular shape is acquired by the leading surface of a gaseous cloud moving through a medium of lower density (even if the cloud is nonuniform), apparently, even in the case of an external explosion into such a medium. The effect of the ambient pressure on a large gaseous cloud can explain not only the shape of Hodge's object but also the presence in this object of a giant, gravitationally bound cluster. Clearly, this hypothesis is also capable of explaining the existence of cluster arcs around dark rings.

ACKNOWLEDGMENTS

I am very grateful to S. Larsen for providing some of his observational data prior to publication (including galaxy images taken with the Nordic Optical Telescope), and to I.D. Karachentsev for providing images taken with the 6-m telescope at the Special Astrophysical Observatory of the Russian Academy of Sciences. Thanks are due to E.Yu. Efremov for great help in the preparation of the figures. I also acknowledge the use of VLT images published by the European Southern Observatory. This work was supported by the Russian Foundation for Basic Research (project codes 00-02-17804 and 00-15-96627).

REFERENCES

1. Yu. N. Efremov, *Sites of Star Formation in Galaxies: Star Complexes and Spiral Arms* [in Russian] (Nauka, Moscow, 1989).
2. Yu. N. Efremov, Astron. J. **110**, 2757 (1995).
3. B. G. Elmegreen, D. B. Elmegreen, J. J. Salzer, and H. Mann, Astrophys. J. **467**, 579 (1996).
4. Yu. N. Efremov, B. G. Elmegreen, and P. W. Hodge, Astrophys. J. (Lett.) **501**, L163 (1998).
5. Yu. N. Efremov, Pis'ma Astron. Zh. **25**, 100 (1999) [Astron. Lett. **25**, 74 (1999)].
6. R. Hayward, Publ. Astron. Soc. Pac. **76**, 35 (1964).
7. I. S. Shklovskiĭ, Astron. Zh. **37**, 369 (1960) [Sov. Astron. **4**, 355 (1960)].
8. P. W. Brand and W. J. Zealey, Astron. Astrophys. **38**, 363 (1975).
9. B. E. Westerlund and D. S. Mathewson, Mon. Not. R. Astron. Soc. **131**, 371 (1966).
10. P. W. Hodge, Publ. Astron. Soc. Pac. **79**, 29 (1967).
11. P. Vader and B. Chaboyer, Astrophys. J. **445**, 691 (1995).
12. S. D. Ryder, L. Staveley-Smith, D. Malin, and W. Walsh, Astron. J. **109**, 1592 (1995).
13. Yu. N. Efremov and B. G. Elmegreen, Mon. Not. R. Astron. Soc. **299**, 643 (1998).
14. Nail V. McKibben and H. Shapley, Harvard Rep. **373** (1953).
15. B. J. Bok, P. Bok, and J. M. Basinski, Mon. Not. R. Astron. Soc. **123**, 487 (1962).
16. Yu. N. Efremov and B. G. Elmegreen, in *New Views of the Magellanic Clouds (IAU Symposium No. 190),* Ed. by You-Hua Chu *et al.* Chelsea: Sheridan Books, 1999, p. 422.
17. J. M. Braun, K. S. de Boer, and M. Altmann, astro-ph/0006060 (2000).
18. Yu. N. Efremov, S. Ehlerova, and J. Palous, Astron. Astrophys. **350**, 457 (1999).
19. M. S. Oey and S. A. Smedley, Astron. J. **116**, 1263 (1998).
20. A. E. Dolphin and D. A. Hunter, Astron. J. **116**, 1275 (1998).
21. A. Dieball and E. K. Grebel, Astron. Astrophys. **339**, 773 (1998).
22. L. S. Marochnik and A. A. Suchkov, *Galaxy* (Nauka, Moscow, 1984).
23. F. Eisenhauer, astro-ph/0101321 (2001).
24. S. Kim, M. A. Dopita, L. Staveley-Smith, and M. S. Bessel, Astron. J. **118**, 2797 (1999).
25. Yu. N. Efremov, Pis'ma Astron. Zh. **26**, 649 (2000) [Astron. Lett. **26**, 558 (2000)].
26. Yu. N. Efremov, astro-ph/0102161 (2001).
27. F. Comeron, Astron. Astrophys. **365**, 417 (2001).
28. S. Larsen, private communications (2001).
29. B. G. Elmegreen, M. Kaufman, C. Struck, *et al.*, Astron. J. **120**, 630 (2000).
30. B. Dirsch, S. Baggett, and M. Dahlem, in *Abstracts of the American Astronomical Society Meeting, 1997,* No. 82.09.
31. S. S. Larsen and T. Richtler, Astron. Astrophys. **345**, 59 (1999).
32. B. G. Elmegreen, Yu. N. Efremov, and S. Larsen, Astrophys. J. **535**, 748 (2000).
33. S. Larsen, J. Brodie, B. Elmegreen, *et al.,* Astrophys. J. (2001) (in press).
34. B. Paczynski, Astrophys. J. Lett. **494**, L45 (1998).
35. S. Portegies Zwart, J. Makino, S. L. W. McMilan, and P. Hut, Astron. Astrophys. **348**, 117 (1999).
36. S. Matshushita *et al.,* astro-ph/0011071 (2000).
37. P. Kroupa, astro-ph/0001202 (2000).
38. B. C. Whitmore, astro-ph/0012546 (2000).
39. B. G. Elmegreen and Yu. N. Efremov, Astrophys. J. **480**, 235 (1997).

40. F. Boulanger and F. Viallefond, Astron. Astrophys. **266**, 37 (1992).
41. Yu. Efremov, S. Pustilnik, A. Kniazev, *et al.,* in preparation.
42. Yu. N. Efremov and S. Larsen, in preparation.
43. P. W. Hodge, *Atlas of the Andromeda Galaxy* (Univ. of Washington Press, Seattle, 1981).
44. C. D. Garmany, P. Massey, and J. W. Parker, Astron. J. **108**, 1256 (1994).
45. Yu. N. Efremov, Astron. Zh. **43**, 284 (1966) [Sov. Astron. **10**, 228 (1966)].
46. J. Vader and B. Chaboyer, Astrophys. J. **445**, 691 (1995).
47. L. Ferrarese, F. Brasolin, R. C. Kennicutt, *et al.,* Astrophys. J. **507**, 655 (1998).
48. J. L. Hitchock and P. W. Hodge, Astrophys. J. **152**, 1067 (1968).
49. M. Normandeau, A. R. Taylor, and P. S. Decodney, Astrophys. J., Suppl. Ser. **108**, 279 (1997).
50. Yu. N. Efremov, submitted to Astron. Zh. (2001).

Translated by A. Dambis

Astronomy Reports, Vol. 45, No. 10, 2001, pp. 784–796. Translated from Astronomicheskiĭ Zhurnal, Vol. 78, No. 10, 2001, pp. 902–914.

The Chemical Compositions and Surface Structures of Two roAp Stars with Lithium Spots (HD 83368 and HD 60435)

A. V. Shavrina[1], N. S. Polosukhina[1], J. Zverko[2], V. Khalak[3], V. V. Tsymbal[4], and J. Žižňovský[2]

[1]*Crimean Astrophysical Observatory, p/o Nauchnyi, Crimea, 334413 Ukraine*
[2]*Astronomical Institute, Slovak Academy of Sciences, Tatranská Lomnica, 05960 Slovak Republik*
[3]*Main Astronomical Observatory, National Academy of Sciences of Ukraine, Goloseevo, Kiev, 252127 Ukraine*
[4]*Tavrian State University, Simferopol, Crimea, Ukraine*

Received March 13, 2001

Abstract—The spectra of two roAp stars have been analyzed as part of a project to study lithium in magnetic Ap stars. Variability of the Li I 6708 Å resonance doublet and rare-earth lines was detected, which can be explained using an oblique rotator model with the lithium spots located at the magnetic poles. Synthetic spectra obtained at different rotational phases have yielded the first data on the atmospheric chemical compositions of these spotted stars. Using refined atomic data and the most complete line lists has enabled a detailed study of the spectra near the Li I 6708 Å line and computation of the Li I line profile taking into account the spotted distribution of the lithium over the stellar surfaces. The positions of two lithium spots and lithium abundances for each of the spots have been determined.

1. INTRODUCTION

Among the various abundance anomalies in the atmospheres of CP stars, the lithium abundance is of special interest, however there have been few observational studies of the Li I 6708 Å doublet in the spectra of Ap stars. In their survey, Faraggiana *et al.* [1] analyzed observations of 39 Ap stars and noted an appreciable diversity in the Li I 6708 Å profiles and a lack of correlation between the line's intensity and parameters of the stellar atmospheres. Namely, stars with similar $T_{\rm eff}$ and $\log g$ values can have different Li I 6708 Å line intensities. An analysis [2] of the observations of 12 CP stars by P. North in 1996 suggested a subdivision into four groups, depending on the pattern of changes in the Li I 6708 Å line with the stellar rotational phase, and provided an explanation for the variability of this line.

As is well known, studies of chemical surface abundances for magnetic Ap stars encounter a number of problems. For example, the chemical composition averaged over a star's surface does not reflect the real structure of the atmospheric layers. Only the local chemical compositions of individual surface regions is physically significant. The variability with rotational phase observed for the line profiles of some elements (due to the Doppler shift) make local abundance studies possible. Doppler imaging techniques [3, 4] have been used to map the surfaces distributions of several elements. The first model computations for the roAp star HD 83368 [5, 6] revealed chemical abundance anomalies in the form of spots and rings, whose position was related to the structure of the stellar surface magnetic field.

In this paper, we undertake a comparative analysis of the characteristics of the two roAp stars HD 83368 and HD 60435, whose spectra show variations of the Li I 6708 Å doublet profile with rotational phase, providing evidence for the presence of two lithium spots near the equator. Both stars belong to the first of the four groups discussed in [2], characterized by comparatively rapid rotation (10–30 km/s) and an appreciable inclination of the rotational axis from the line of sight. The position of the two lithium spots can be related to the poles of the dipole magnetic field.

1063-7729/01/4510-0784$21.00

Table 1. log of spectral observations

Spectrum number	Date	UT	Exposure	HJD 2450000+	Rotational phase	Spectral region*
			HD 83368			
23	10.3.96	$4^{h}\,41^{m}$	20^{m}	152.705	0.331	A
38	11.3.96	5 11	20	153.726	0.689	A
48	12.3.96	6 15	20	154.770	0.055	A
57	13.3.96	0 25	20	155.527	0.320	B
61	13.3.96	4 19	20	155.690	0.378	A
65	13.3.96	4 44	20	155.707	0.384	A
71	13.3.96	7 02	30	155.807	0.419	A
77	14.3.96	0 50	20	156.545	0.678	A
83	14.3.96	6 23	30	156.779	0.760	A
85	14.3.96	6 57	30	156.803	0.768	C
			HD 60435			
03	8.3.96	1 48	90	150.608	0.741	A
13	9.3.96	2 45	90	151.647	0.877	A
21	10.3.96	0 36	90	152.558	0.995	A
22	10.3.96	2 27	90	152.635	0.005	B
33	11.3.96	0 39	90	153.560	0.128	A
47	12.3.96	4 02	90	154.701	0.274	A
60	13.3.96	2 37	90	155.642	0.397	A
78	14.3.96	1 13	90	156.583	0.519	A
			HD 101065			
04	8.3.96	4 05	90	150.705	—	A

*Notation for spectral regions: A—6675–6735 Å, B—6120–6180 Å, C—6615–6671 Å.

2. OBSERVATIONS AND ANALYSIS OF THE SPECTRA

The spectra of both stars near the lithium 6708 Å doublet were obtained by North and described in detail in [7]. Table 1 presents the dates, exposure times, rotational phases, and spectral ranges of the observations. The rotational phases for HD 60435 were computed using the ephemeris from [8]:

$$\text{JD (mean } B_{\min}) = 2\,445\,385.75 + 7.6793E.$$

and those for HD 83 368 using the ephemeris from [9]:

$$\text{JD } (t_0 \text{ puls}) = 2\,448\,312.23606 + 2.851976E.$$

The preliminary reduction of the observations was carried out by North using the standard IHAP package. Subsequent reductions were performed using the SPE code developed by Sergeev [10]. We made a quantitative analysis of the spectra, applying a synthetic spectrum technique using V.V. Tsymbal's programs STARSP [11] and ROTATE, which enabled the computation of profiles of lines formed in both the photosphere as a whole and in individual spots on a rotating star, as described in [6]. We used the model atmospheres of Kurucz [12] and line lists with atomic data provided by Kurucz [13] (CDROM 23) and from VALD [14–16], available via the Internet. The atomic data for doubly ionized rare earths were taken primarily from [17–20]. In order to identify lines of rare-earth elements, we computed positions of the lines using data on rare-earth energy levels from the NIST database, also available via the Internet.

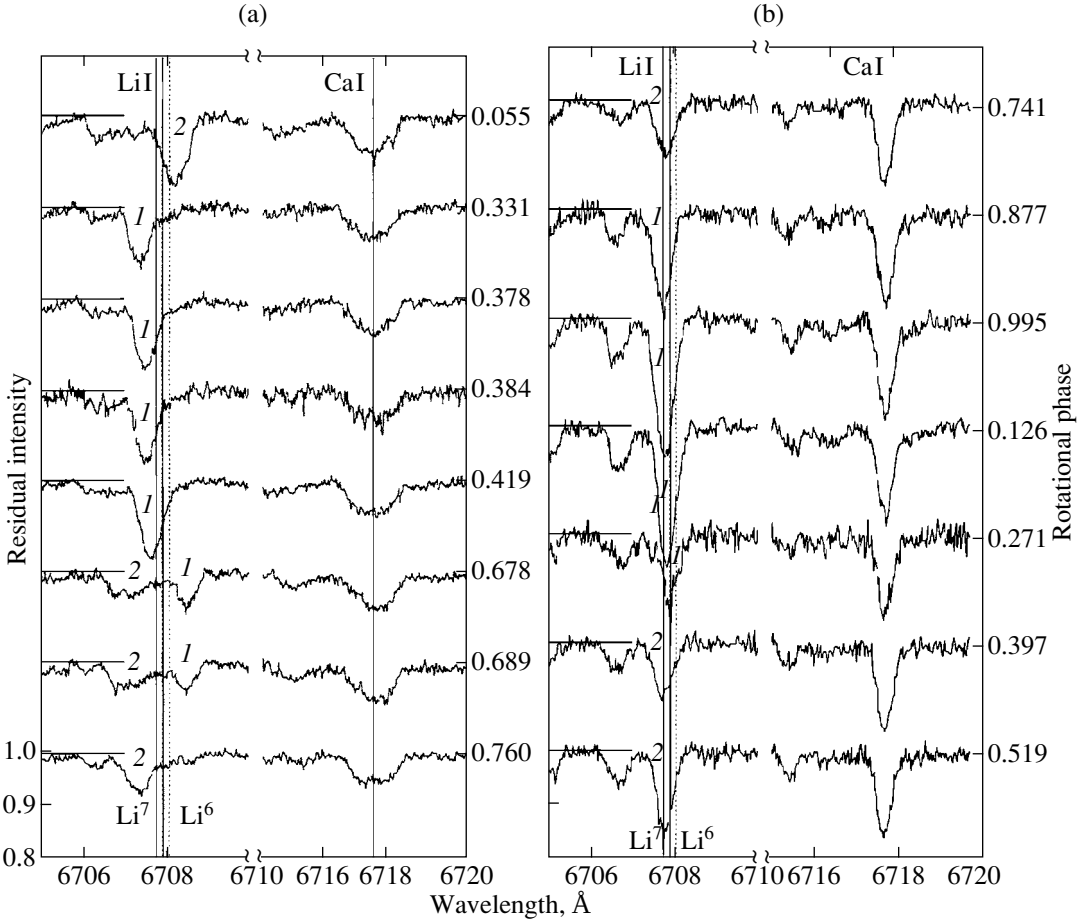

Fig. 1. Variations of the Li I 6708 Å line profiles with rotational phase in the spectra of (a) HD 83368 and (b) HD 60435. The numbers *1* and *2* correspond to the two lithium spots.

3. SPECTRAL VARIABILITY OF HD 83368 AND HD 60435 NEAR THE Li I 6708 Å DOUBLET

The spectra of the roAp stars HD 83368 and HD 60435 demonstrate cases when the Li I 6708 Å line is the most prominent variable feature of the spectral region considered (Fig. 1). This variability is associated with Doppler shifts due to rotational modulation of the spectrum and a non-uniform distribution of lithium over the stellar surface. CP stars with strong and variable Li I 6708 Å lines are rarely observed and virtually unstudied, making a more detailed consideration of the spectroscopic anomalies of these two stars, along with their other characteristics, of evident interest.

Figure 2 presents curves of the radial velocities V_r for both stars and of the equivalent widths of the 6708 Å line W_λ, which show rather convincingly the presence of two regions of formation of the Li I 6708 Å line (i.e., two lithium spots) on both stars. There is some difference in the behavior of the lithium lines for the two stars, mainly due to their different rotational velocities ($v \sin i = 34$ km/s for HD 83368 and 11 km/s for HD 60435). Note that for HD 83368 variations of the 6708 Å line profile due to changing visibility of spots in the course of the star's rotation and the corresponding changes of W_λ and V_r have similar amplitudes for the two spots (Fig. 2a). This indicates that the spots are located in the immediate vicinity of the stellar equator and that the star is observed in its equatorial plane. In this case, we can assume that the part of the V_r curve near phase 0.5 is determined by spot *1*, which passes the central meridian at that time, while the part of the V_r curve near phase 0.0 is determined by spot *2* (the designations of the spots are arbitrary). The spots appear in turns in the visible hemisphere; we can see both spots simultaneously only during a short time interval

(phases 0.6 to 0.7), when they are on opposite sides of the stellar disk.

Note that the equivalent width of the Li I 6708 Å line W_λ reaches its maximum at phases 0.0 and 0.5, and the maximum brightness and magnetic field are observed at the same phases [6]. The periodic variations of the radial velocities V_r and equivalent widths W_λ for HD 83368 correspond to an oblique magnetic rotator model, with the stellar rotational axis inclined at $i = 90°$ to the line of sight and at $\beta = 90°$ to the magnetic-dipole axis.

The roAp star HD 60435 shows a somewhat different variability pattern. It is apparent from Fig. 2b that the V_r curve near phase 0.0 is formed by the main spot *1*, which crosses the central meridian at that time, while the V_r curve near phase 0.5 is determined by the poorly distinguished spot *2* (which is not clearly seen, or "on the wane").

Since the apparent motion of the spots across the stellar disk is the main cause of variability of the Li I 6708 Å profile, the different behavior of this line in the two stars can be explained fairly well by differences in their oblique rotator models (in the angles i and β), with the lithium spots located near the poles of the magnetic dipoles.

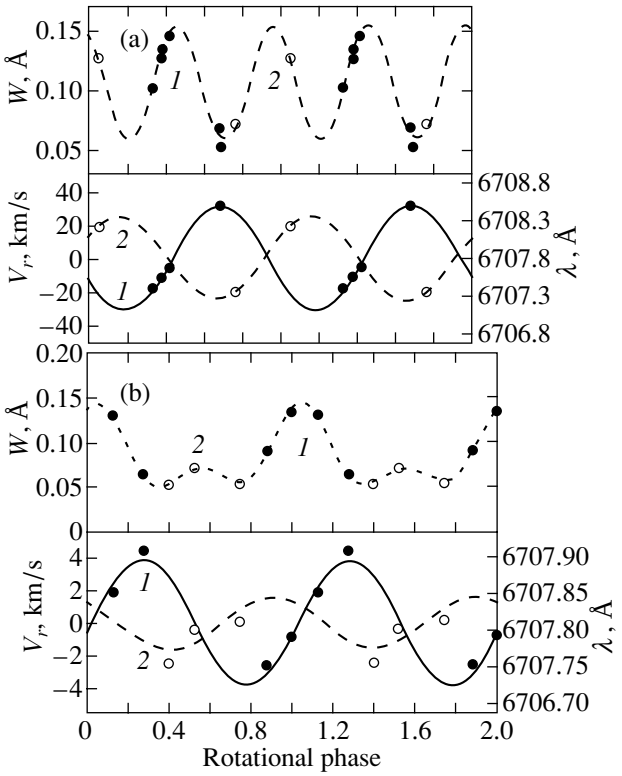

Fig. 2. Variations of the Li I 6708 Å equivalent widths and radial velocities in the spectra of (a) HD 83368 and (b) HD 60435 with rotational phase. The filled and open circles correspond to lithium spots *1* and *2*, respectively.

4. CHEMICAL COMPOSITION ESTIMATES AT DIFFERENT ROTATIONAL PHASES

Quantitative analyses of the spectra of Ap stars are usually hampered by the presence of non-uniform surface distributions of several chemical elements, in connection with the stellar magnetic fields. The results of spectral analyses for HD 83368 at 6675–6735 Å, 6120–6170 Å, and 6615–6675 Å are presented in our earlier paper [6]. The first results on elemental abundances for HD 60435 were obtained by Zverko *et al.* [21]. One of the objectives of the present study is to better account for the effects of the non-uniform surface distribution of elements and of the magnetic intensification of spectral lines. We paid special attention to the lithium 6708 Å line, as well as to lines of other elements with sufficiently large Landé factors.

For our analysis, the model atmosphere parameters $T_{\rm eff}$, $\log g$, and $v \sin i$ were taken from Shavrina *et al.* [6] for HD 83368 and from Zverko *et al.* [21] for HD 60435. To estimate possible deviations, we also computed synthetic spectra using model atmospheres with parameters differing from the chosen ones by ±250 K in $T_{\rm eff}$ and ±0.5 in $\log g$. For HD 83368, the best agreement of the iron abundances derived from Fe I and Fe II lines was obtained for the model with $T_{\rm eff} = 7750$ K and $\log g = 4.0$. For HD 60435, the model with $T_{\rm eff} = 8250$ K and $\log g = 4.5$ was selected based on the lines of Fe I, Fe II and Cr I, Cr II. For both stars, the models with metal abundance [M/H] = 0.0 were the best. We also took the values $v \sin i = 11$ km/s for HD 60435 and $v \sin i = 34$ km/s for HD 83368 from the cited papers.

We estimated the abundance variations with rotation for several elements by comparing the synthetic and observed spectra for different rotational phases. The results are presented in Table 2, which contains maximum and minimum elemental abundances, expressed as $\log(N/H)$, for HD 83368 (columns 2 and 3) and HD 60435 (columns 4 and 5). The number of lines n used to determine the abundances and the uncertainties of the abundances σ are given in columns 6 and 7. We repeated the procedure to fit the computed to the observed spectrum until achieving the minimum discrepancy for each element's abundance using all lines. The errors σ reflect uncertainties in the abundance estimates for the given model atmosphere. Columns 8 and 9 of Table 2 present abundances for HD 60435 derived by Zverko *et al.* [22] for two model atmospheres: $T_{\rm eff} = 8250$ K, $\log g = 4.5$ (column 8, model *1*) and $T_{\rm eff} = 7750$ K, $\log g = 3.0$ (column 9, *model 2*), with [M/H] = 0.0 and $v \sin i =$

Table 2. Elemental abundances in the atmospheres of HD 83368 and HD 60435 and comparison with data for HD 60435 from [22], solar data [23], and data for HD 24712 from [24] and [25]

Element	HD 83368		HD 60435		n	σ,	HD 60435		Sun	HD 24712	
	max	min	max	min		dex	m*1*	m*2*		max	min
1	2	3	4	5	6	7	8	9	10	11	12
CI	−3.8	−4.5	−3.6	−3.8	6	.3			−3.52	−4.5	
NI	−3.0	−4.0	−3.2	−3.4	10	.3			−4.09	−4.4	
OI	−3.4	−4.3	−3.9	−4.5	2	.3	−4.0	−4.0	−3.21	−3.8	
NaI	−6.1	−6.1	−5.8	−5.8	2	.3		−5.9	−5.72		
AlI	−6.0	−6.6	−6.2	−6.2	1	.2		−6.8	−5.57	−5.53	
SiI	−3.9	−4.9	−3.6	−4.4	5	.2		−4.9	−4.48	−4.43	
SI	−5.2	−5.2			5	.3			−4.84		
CaI	−5.1	−5.6	−4.7	−5.1	2	.1	−5.4	−5.4	−5.69	−5.69	
CaII	−5.3	−5.8	−5.8	−5.8	3	.3				−5.22	−4.88
TiII	−6.8	−7.3	−7.2	−7.3	2	.2			−7.10	−7.22	−7.29
CrI	−4.1	−5.0	−4.3	−4.4	4	.2			−6.35	−5.93	−5.80
CrII	−4.2	−4.6	−4.6	−4.6	4	.3	−4.9	−5.0		−5.58	−5.33
FeI	−4.6	−4.9	−4.1	−4.2	4	.1	−4.4	−4.5	−4.54	−4.77	−4.88
FeII	−4.3	−4.7	−4.3*	−4.3*	10	.2	−4.4	−4.5		−4.80	−5.11
CoI	−5.5	−6.3			1	.3		−5.7	−7.13	−5.88	−5.57
YI	−6.4	−7.0			4	.2		−8.5	−9.81	−7.80	−7.80
BaII	−9.1	−9.1	−9.1*	−9.1*	1	.2	−9.5	−10.0	−9.82	−9.12	−8.98
LaII	−8.4	−9.2			3	.4		−10.3	−10.82	−9.40	−8.75
CeII	−8.1	−8.7			2	.2		−9.4	−10.41	−9.18	−8.90
PrII	−9.3	−9.3	−9.3	−9.3	4	.2			−11.24	−10.15	−9.60
PrIII	−8.5	−9.1	−8.4	−8.8	4	.2					
NdII	−8.2	−9.3	−7.9	−8.6	4	.3		−9.2	−10.55	−9.13	−8.64
NdIII	−7.2	−8.0	−7.5	−8.0	2	.2					
SmII	−8.4	−9.1	−8.1	−8.4	3	.2		−9.9	−11.06	−9.75	−9.16
EuII	−9.8	−9.8			2	.2		−9.5	−11.07	−9.50	−9.00
GdII	−8.4	−8.9			6	.3	−8.2		−10.95	−9.11	−8.70
ErII	−8.1	−8.6			1	.3			−11.07	−9.79	−9.53
YbII			−9.3	−9.4	1	.3			−11.08	−8.30	−8.30
LuII	−9.2	−9.2	−9.4	−9.4	1	.2			−11.91		

* From spectral range 6120–6180 Å.

11 km/s. For comparison, column 10 contains the abundances for the Sun [23], and columns 11 and 12 present atmospheric abundances for a similar roAp star HD 24712, from Roby and Lambert [24] (for C, N, and O) and Ryabchikova *et al.* [25] (for the other elements). Note that, despite its similar excess abundance of rare-earth elements HD 24712 does not have a measurable Li I 6708 Å line in its spectrum [1].

This may provide an additional argument for a non-rare-earth origin for the 6708 Å spectral feature.

4.1. Abundances of Iron-Peak Elements

We can see from Table 2 that the elemental abundances in both stars' atmospheres vary with the rotational phase—as a rule, within 1 dex. The main difference between the two stars is found for iron-peak elements. For HD 60435, the variations in iron-peak elements are within the errors, whereas for HD 83368 they comprise 0.3–0.9 dex (especially for Cr I). The corresponding results for another roAp star, HD 24712 [25], are similar to those for HD 60435. The Ti and Fe abundances are close to the solar values, whereas for both stars Cr exhibits a 2 dex excess over the solar value and a 1.5 dex excess over the abundance for the roAp star HD 24712. An excess of Y by 3.1 dex relative to the Sun and 1.1 dex relative to HD 24712 is found for the atmosphere of HD 83368.

4.2. Light Elements

In the atmosphere of HD 83368, all the elements studied from C to Ca (except for Na and S) vary significantly (from 0.5 to 1.0 dex), whereas for HD 60435 only Si and O show considerable variability (by 0.8 and 0.6 dex, respectively).

The Na abundances of both stars are normal compared to the solar value. There is a deficiency of O, whereas N exhibits an excess in both cases. C is deficient for HD 83368 and has a normal abundance for HD 60435. The abundances of Si and Ca are normal for HD 83368 and slightly enhanced for HD 60435.

Compared to HD 24217, both stars have a significant excess of N (by 1 dex). The abundances of C and Ca for HD 60435 are enhanced by 0.8 dex. The abundances of all the other light elements studied are the same within the errors. The O abundance for HD 83368 is the same as that for HD 24712; a deficiency of 0.4 dex is observed for HD 60435.

4.3. Magnetic Fields of HD 83368 and HD 60435

The structure and intensity of the magnetic field of HD 83368 were discussed in detail by Bagnulo *et al.* [26] and Polosukhina *et al.* [5]. In the latter paper, the surface magnetic field was estimated to be ~2 kG, and the field varied by ±300 G in the course of the star's rotation. We attempted to estimate the magnetic field strength in the same way as in [6], but taking into account the spot structure for Fe II, which is clearly seen in the profiles of the Fe II 6147 and 6149 Å lines for HD 83368. We computed synthetic profiles for these lines including magnetic line splitting for two values of the magnetic field: with our own estimate of 2 kG [5], and with the estimate of 11 kG from [27, 28]. Zeeman splitting was taken into account for the 2 kG field; it is obviously necessary to include the Paschen–Back effect for the 11 kG field. The line profiles shown in Fig. 3 were computed for $H_s = 2$ kG, for the case of two Fe II spots at longitudes of $l_1 = 110°$ and $l_2 = 170°$ and blending with the Pr II 6148.24 Å line ($l_r = 100°$). We can see from this figure that the value $H_s = 2$ kG is preferable. This is confirmed by computations of the Eu II 6645.46 Å, Nd III 6145.07 Å, and Ba II 6141 Å profiles, likewise taking into account the spotted distribution of these elements over the stellar surface (Fig. 4a).

In contrast to HD 83368, there are no original magnetic-field measurements for HD 60435. Since we also infer the presence of two lithium spots for this star [2], like for HD 83368, we adopt a magnetic-dipole model and assume that the lithium spots reflect the structure of the magnetic field. The maximum intensity in the lithium profiles occurred at phases 0.519 and 0.995 (see Section 3). This latter phase is close to 0.005 (near 6120–6180 Å), where we see lithium spot *2* near the star's central meridian. Therefore, we used the spectrum at this phase to estimate the magnetic field from the Ba II 6145 Å and Fe II 6147, 6149 Å line profiles. We computed the profiles of these lines, taking into account Zeeman splitting and according to the magnetic field configuration at the corresponding phase, for a series of H_s values from 2 to 8 kG and $v \sin i = 11 \pm 2$ km/s. The best agreement between the computed and observed profiles was achieved for $H_s = 2$ kG for the Fe II lines and $H_s = 3.5$ kG for the Ba II line (Fig. 4b). We were also able to obtain a good fit simultaneously to the Fe II and Ba II lines for the same field value, $H_s = 3$ kG, but with different $v \sin i$ values: 9 km/s for the Fe II lines (Fig. 3b) and 13 km/s for the Ba II line. Our computations show that for this star the Nd III 6145 Å line cannot be used to determine the magnetic field because of strong blending with the Si I 6145.23 Å line. Thus, our estimate of the surface magnetic field for HD 60435 is $H_s = 3 \pm 1$ kG, at $v \sin i = 11 \pm 2$ km/s.

4.4. Rare Earths

The spectra of both roAp stars are rich in rare-earth lines. We accordingly paid special attention to the analysis of these lines, since they can be blended with the variable Li I 6708 Å line. The Nd II, Pr II, and Pr III lines are especially strong. The problems of identifying rare-earth lines in observed spectra and of estimating the gf values for rare-earth lines are

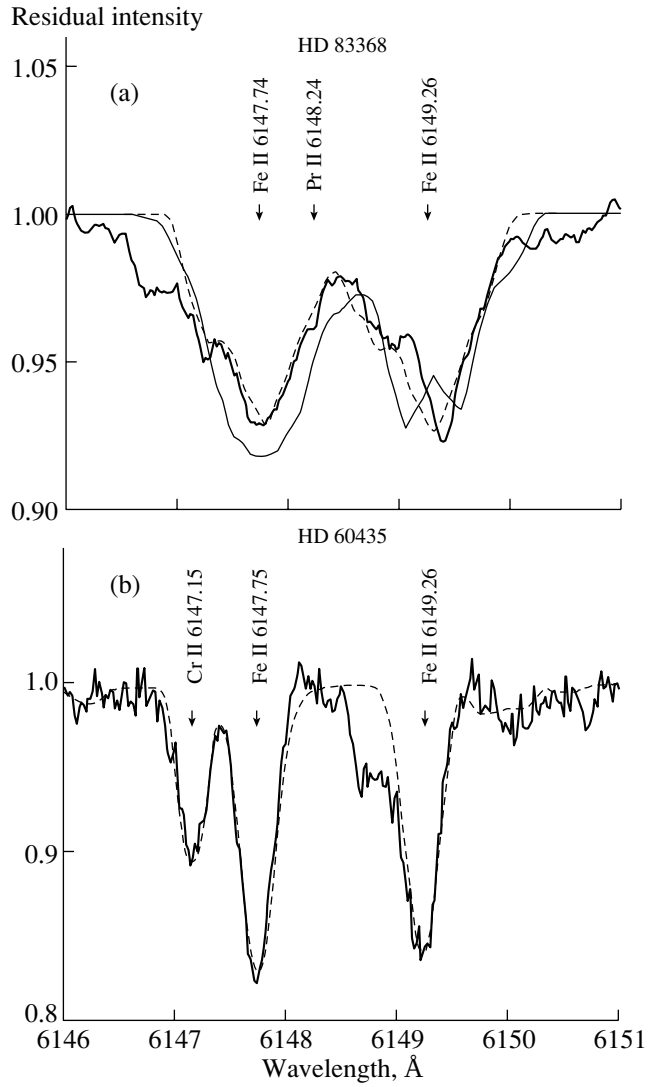

Fig. 3. Fe II 6147.74 Å and 6149.26 Å line profiles. The bold solid curves show the observed spectrum, and the dashed and thin solid curves the synthetic spectra. (a) HD 83368, phase 0.320; dashed curve, 2 kG magnetic field (Zeeman splitting); thin curve, 11 kG field (Paschen–Back effect), taking into account spots on the stellar surface. (b) HD 60435, phase 0.005; dashed curve, 3 kG field (Zeeman splitting).

discussed in detail in [5]. The Nd III 6690.9 Å and Pr III 6706.70 and 6727.67 Å lines are the most strongly variable and most prominent at 6675–6735 Å in the spectra of both stars (Figs. 5a, 5b). Their intensity variations show a phase shift relative to variations of the Li I 6708 Å line. For example, we can see two spectra for HD 83368 at phases close to the magnetic-field maxima (Fig. 5a): with the highest intensity of the lithium line at phase 0.055 and with the strongest rare-earth lines at phase 0.419. The rare-earth lines are significantly broader than the Li I 6708 Å line, which is rather narrow and shows a two-component structure only at phases 0.689 and 0.760. The rare-earth lines, especially those for doubly ionized atoms, have more complex structures (more than two components), suggesting that the region of their formation also has a more complex structure, probably made up of ring structures around polar areas with lithium spots.

Figure 5b also shows spectra of HD 60435 at the phases of maxima, 0.995 and 0.519. The insufficient spectral resolution and appreciably different Doppler shifts for the two stars ($v \sin i = 35$ and 11 km/s) hinder a reliable determination of the possible phase lag between variations of the Li and rare-earth lines for the second star. Our data provide evidence for synchronous intensity changes for the lithium, Pr II–III, and Nd II–III lines. The most significant variations

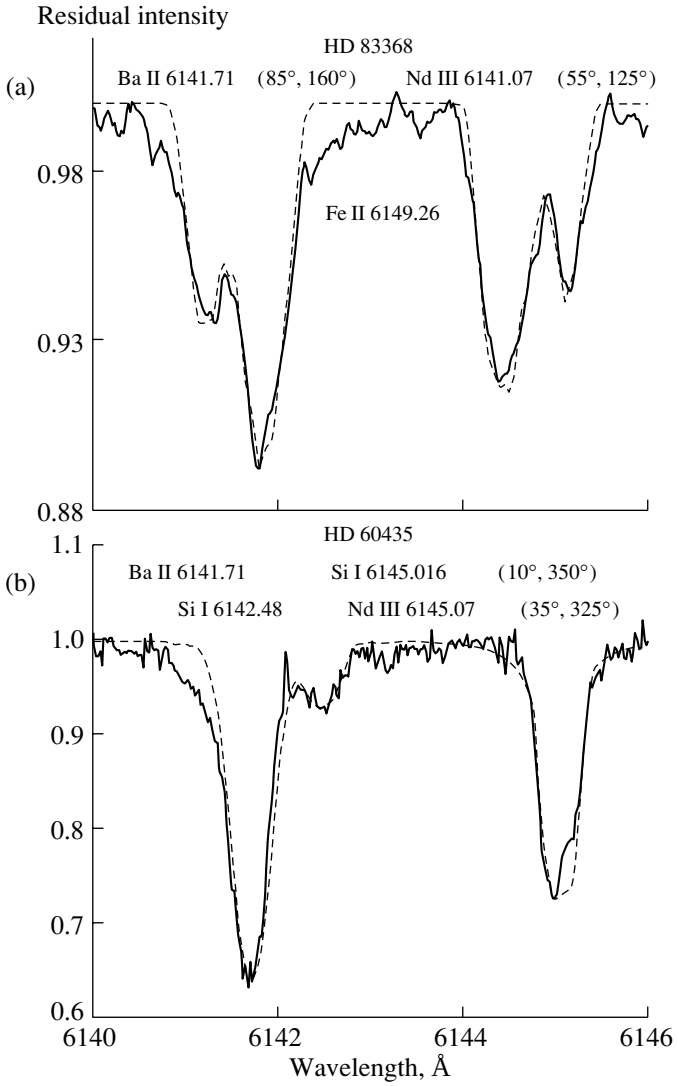

Fig. 4. Ba II 6141.71 Å line profile with Zeeman splitting and hyperfine structure taken into account. The solid curves show the observed spectrum and the dashed curves show the synthetic spectra. (a) HD 83368, 2 kG magnetic field; (b) HD 60435, 3.5 kG magnetic field. The longitudes of the spots are indicated in parentheses next to the laboratory wavelengths of the lines.

with rotational phase are exhibited by the La II, Ce II, Nd III, Sm II, Gd II, and Er II lines in the spectrum of HD 83368 and the Nd II and Nd III lines in the spectrum of HD 60435.

All the studied elements showed excesses of $\sim$2 dex in the atmospheres of both stars. Of the lanthanides, Eu showed the smallest excess in HD 83368, while Sm showed the largest excess of 2.3 and 2.8 dex relative to the solar value for HD 83368 and HD 60435, respectively.

HD 83368 has the same abundances of La, Nd, and Gd as HD 24712, within the errors, whereas Ce, Pr, Sm, and Eu exhibit excesses of 0.6, 0.6, and 1.3 dex, respectively. When computing the synthetic spectra for the Pr III and Nd III lines, we used the gf values of Bord [19]. The praseodymium abundances derived from Pr III lines in two spectral regions are the same within the errors: $\log(N_{\rm Pr}/N_{\rm H}) = -8.5 \pm 0.2$ for HD 60435 (phases 0.005 and 0.995) and $\log(N_{\rm Pr}/N_{\rm H}) = -9.0 \pm 0.2$ for HD 83368 (phases 0.320 and 0.331). These results leave no doubt about our correct identification of the Pr III 6160.2, 6161.2, 6706.7, and 6727.3 Å lines. However, there is a disagreement in the praseodymium abundances derived from the Pr II and Pr III lines, similar to that for Nd II and Nd III. A higher Pr III abundance, relative to Pr II, is derived from four Pr III lines: 6160.24, 6161.22, 6706.70, and 6727.63 Å, using the gf values computed by Bord [19]. Similar differences in the

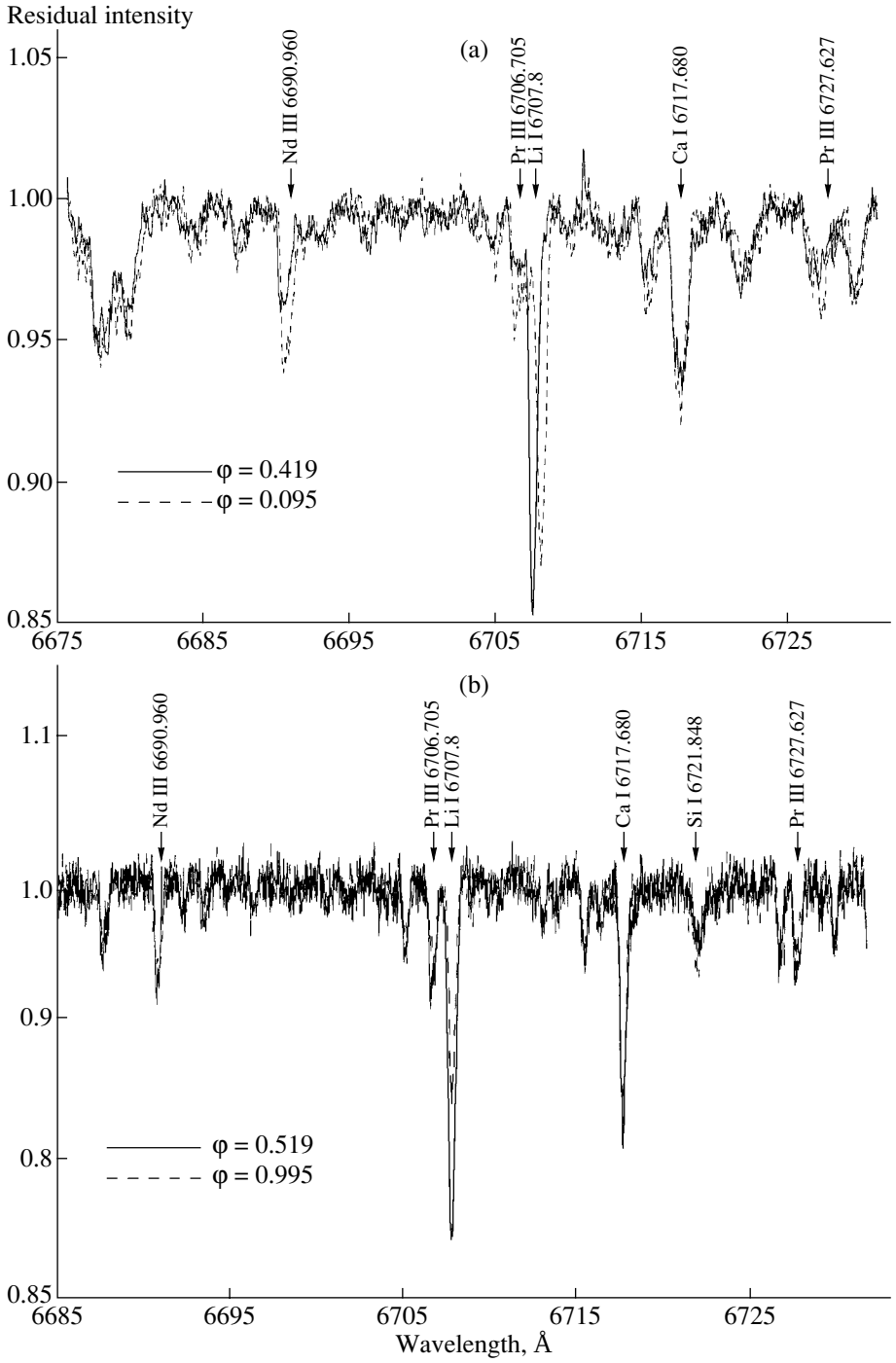

Fig. 5. Comparison between spectra for two different phases. (a) HD 83368, phase 0.419 (solid curve) and phase 0.055 (dashed curve). The lines of Nd III and Pr III are appreciably stronger in the latter spectrum, while the Li I line is weaker. (b) HD 60435, phase 0.995 (solid curve) and phase 0.519 (dashed curve). In contrast to HD 83368, synchronous variations are observed for the Li I line and the lines of rare-earth elements.

abundances for singly and doubly ionized rare-earth atoms were noted for other roAp stars in [25, 30]. This may provide evidence of surface [29] or vertical stratification of the ions of these elements for both stars.

5. ANALYSIS OF THE SURFACE SPOT STRUCTURES OF HD 83368 AND HD 60435

5.1. Modeling the Li I 6708 Å Line

Preliminary analyses of the spectra of HD 83368 [5, 6] and HD 60435 [21] showed that lithium was

distributed non-uniformly over the surfaces of these stars. The problem of modelling a stellar surface and the solution method used in the ROTATE code developed by Tsymbal have already been described in detail in [6]. However, the number of spectra for different rotational phases is insufficient to correctly solve the inverse problem of finding the physical parameters describing the conditions under which the spectral lines are formed. For this reason, we chose the method of direct modelling to compute spectral-line profiles for the atmosphere of a rotating star [31]. We divided the stellar surface into 32×32 cells and supposed the presence of spots, with a uniform distribution for the chemical element under consideration within each spot. The model parameters used in determining the physical conditions in the spots are the inclination of the stellar rotational axis to the line of sight, i; the equatorial rotational velocity of the star, v_e; the number of spots, N_s; each spot's coordinates and size, λ_s, ϕ_s, R_s; and the abundance of the element in question in each spot [Li].

The best agreement between the theoretical and observed profiles at all phases is achieved only with particular values of the model parameters. For example, the longitude, radius, and lithium abundance for each spot are determined by the spectrum for the phase of the spot's maximum visibility. To a first approximation, the longitude can also be taken to be the intersection of the radial velocity curve for the lithium line and the star's mean radial velocity. Taking the spot latitudes to be zero as a first approximation and using the known $v \sin i$ value (Section 4.3), we determined the angle i and equatorial velocity v providing the best agreement between the computed and observed Li line profiles. We then improved the agreement for all phases by varying the spot latitudes. In the final stage of profile fitting, we implemented corrections to the longitudes and minimum corrections to the abundances for each phase and then derived mean values for the spot longitudes and lithium abundances in the spots, along with the uncertainties. In general, the fits were better for phases when the spot was near the center of the visible disk and worse for phases when it was near the limb.

We determined the number of lithium spots (two) by inspecting the radial velocity curves. Other parameters were derived from the conditions for best agreement between the observed and theoretical line profiles at all rotational phases. Parameters for the lithium spots on HD 83368 were determined in [5] for $i = 90°$, $v_e = 35$ km/s, and the photospheric lithium abundance $\log(N_{\rm Li}/N_{\rm H}) = -10.2$:

$$\text{Spot } \textit{1}\text{: } l_1 = 173° \pm 6°, \varphi = 0° \pm 6°,$$
$$R = 33° \pm 6°,$$
$$\log(N_{\rm Li}/N_{\rm H}) = -8.4 \pm 0.2 \text{ (see Fig. 6a)},$$
$$\text{Spot } \textit{2}\text{: } l_2 = 337° \pm 6°, \varphi = 0° \pm 6°,$$
$$R = 35° \pm 6°,\ \log(N_{\rm Li}/N_{\rm H}) = -8.5° \pm 0.2,$$

where l is the spot longitude, φ its latitude, and R its radius ($R = 90°$ would correspond to the entire visible hemisphere).

The i value for HD 60435 was determined as follows. Matthews *et al.* [32] estimated the star's luminosity to be $L/L_\odot = 21.4$ using the value $T_{\rm eff} = 8200$ K derived from $uvby$ and H_β photometry. Further, we can use the Stefan–Boltzmann law to find the radius of the star, $R_\star = 2.30 \pm 0.45 R_\odot$. Taking into account the rotational period, $P_{\rm rot} = 7.6793^{\rm d} \pm 0.0006^{\rm d}$ d [8], and the value $v \sin i = 11 \pm 2$ km/s (see Section 4.3), we obtain the equatorial velocity, $v_{\rm e} = 15 \pm 3$ km/s from the formula $v_{\rm e} = 2\pi R_\star / P_{\rm rot}$ and the corresponding inclination of the rotational axis to the line of sight, $i = 47° \pm 23°$ or $133° \pm 23°$.

We also estimated i for HD 60435 (with the known value $v \sin i = 11 \pm 2$ km/s) independently by analyzing the Li I line profile variations with rotational phase. Using the ROTATE code and the model atmosphere with $T_{\rm eff} = 8250$ K, $\log g = 4.5$, [M/H] = 0, $i = 133°$ (or 47°), and $v_{\rm e} = 15$ km/s, the best fit of the computed and observed profiles at all phases was obtained for a photospheric Li abundance (outside the spots) of $\log(N_{{\rm Li}i}/N_{\rm H} = -10.2$. The resulting parameters of the lithium spots were:

$$\text{Spot } \textit{1}\text{: } l_1 = 11° \pm 6°, \varphi = -15° \pm 5°, R = 44° \pm 3°,$$
$$\log(N_{\rm Li}/N_{\rm H}) = -8.2 \pm 0.2 \text{ (Fig. 6b)},$$
$$\text{Spot } \textit{2}\text{: } l_2 = 205° \pm 10°, \varphi = 15° \pm 5°, R = 40° \pm 7°,$$
$$\log(N_{\rm Li}/N_{\rm H}) = -9.3 \pm 0.2.$$

Figures 6a and 6b show plots of residual intensity versus wavelength; the intensity curve for each rotation phase is offset by a corresponding amount along the vertical axis. The phases for each plot are indicated to the right. The agreement between the theoretical and observed spectrum appears good for phases when one of the spots is completely visible. The agreement is worse at phases of partial visibility of one or both of the spots. This can probably be understood if the distribution of Li over the spot surface is non-uniform and/or the Li abundance is stratified with depth in the spot. The reliability of our lithium abundance determinations for the spots is also limited by blending with other lines.

We would like to add that attempts to introduce the ^{6}Li isotope line led to a poorer agreement between the theoretical and observed profiles, even for the ratio $^6{\rm Li}/^7{\rm Li} = 0.1$ (with the possible exception of the second spot on the surface of HD 60435).

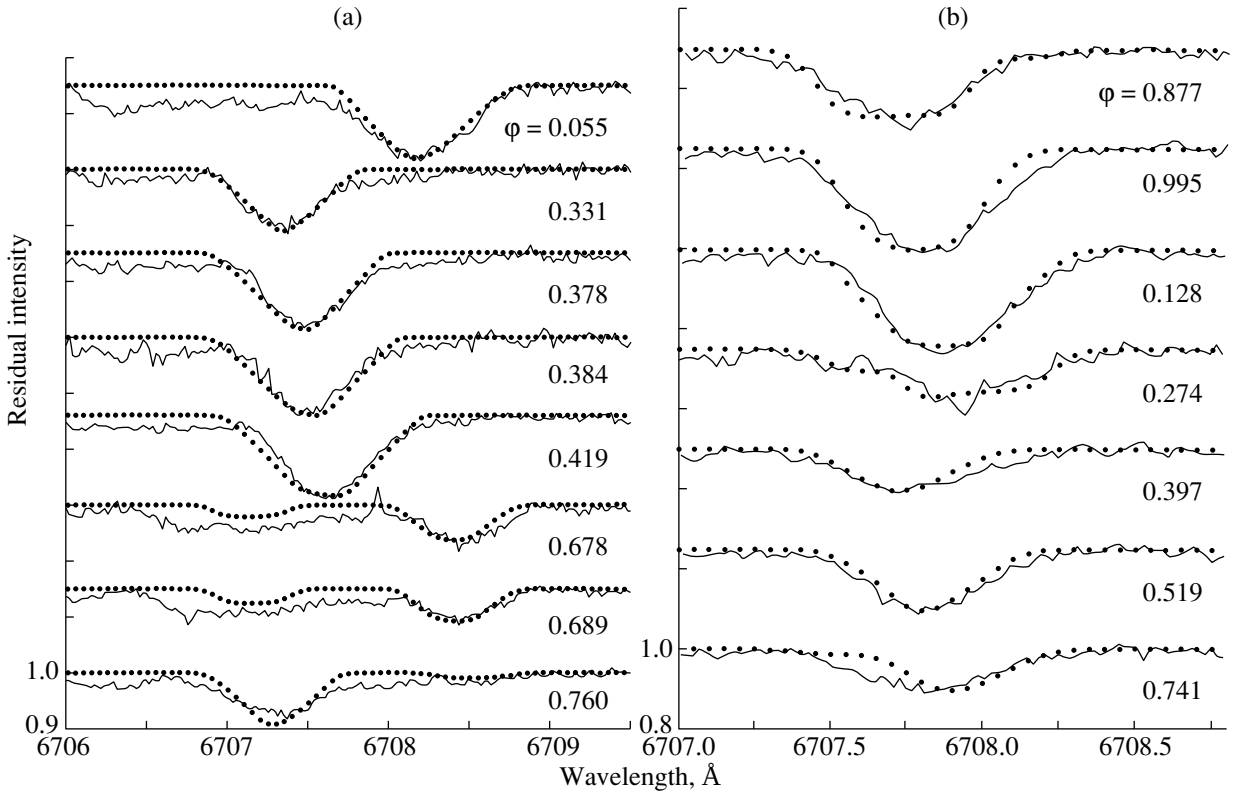

Fig. 6. Observed (dots) and computed (solid curves) profiles of the Li I 6708 Å line at (a) eight rotational phases for HD 83368 and (b) seven rotational phases for HD 60435.

6. CONCLUSIONS

We find that the elemental abundances for both stars differ from each other and from the solar values, a common feature for CP stars. The main distinguishing difference between the atmospheric chemical compositions of HD 83368 and HD 69435 (like HD 24712) and that of the Sun are high abundances of rare-earth elements. The abundances for these elements usually exceed the solar values by more than 2–3 dex. Compared to another roAp star, HD 24712, both stars show excess abundances of nearly all the elements studied, though oxygen is deficient in HD 60435.

In the atmosphere of HD 83368, the elemental abundances usually show rotational variations within 0.9 dex, whereas in HD 60435 the strongest variations (up to 0.7 dex) are exhibited by the rare-earth elements and some light elements (O, Si). The main difference between the two stars is that the abundances of iron-peak elements in HD 60435 do not vary, within the error margins.

The largest amplitudes of rotational abundance variations were shown by the rare-earth elements. These variations are probably related to the spotted structure of the stellar surfaces. For HD 83368, the maximum abundances of elements with the strongest variability occur at phases when the Li line is not at an extremum. We conclude that some elements (mostly singly and doubly ionized rare-earth elements) can form ring structures surrounding the lithium spots. Such structures have also been suggested for HD 60435.

For HD 83368, the behavior of the Li line profile and of the magnetic field shows that the lithium spots approximately coincide with the magnetic poles. The positions (longitudes) of the two lithium spots presented in Section 5.1 correspond to a delay of $\sim 23°$ between the magnetic field and the spots, in agreement with the delay derived in [2]. At the same time, the l_1 and l_2 values show that the lithium spots are not separated by exactly 180°. The variations of the Li I line profile for HD 60435, likewise, indicate positions for the spots that are not exactly opposite on the stellar surface. As in the previous case, we propose that the magnetic poles approximately coincide with the lithium spots.

The determination of i (about 90°) for HD 83368 was described in [5]. For HD 60435, we found $i = 133° \pm 2347° \pm 23°$ (Section 5.1).

Our analysis of profiles of the magneto-sensitive Fe II (6147, 6149 Å) lines yielded surface magnetic

fields of $H_s = 3$ kG for HD 60435 and $H_s = 2$ kG for HD 83368.

The ROTATE code, which was developed for line-profile computations for spotted stellar surfaces, enabled us to derive parameters of the spots: their positions, sizes, and elemental abundances. However, it is difficult to obtain a good fit when the spot is near the limb due to blending by lines of other elements (mainly rare earths) and the weakness of the lithium line at the stellar limb. A similar problem was also noted in [33]. The phase coverage for our observations is incomplete, and our results should be considered preliminary. Note that our lithium abundances (3.85 and 2.65 for HD 60435, 3.60 and 3.50 for HD 83368) agree with that determined for another roAp star, γ Equ (3.7) [34]. No less interesting is the fact that our values are close to the lithium abundances in lithium-enriched late-type giants, which, as proposed by Lambert and Sawyer [35], may begin their evolution as a class of Ap star on the upper main sequence, i.e. as chemically peculiar stars, whose abundance anomalies can be explained by diffusion due to an imbalance between the radiative and gravitational forces, which act differently on atoms and ions. It is generally thought that the diffusion separation of elements should begin before the main-sequence phase and that giants have shifted two classes below Ap stars. To explain the high lithium abundances observed for some peculiar giants with a carbon deficiency (nitrogen excess), Lambert and Sawyer [35] suggested that lithium atoms were dredged up from the zone of nuclear burning due to the action of diffusion prior to the star's arrival on the main sequence. To stabilize the diffusion distribution of elements, the protostar's envelope must be in a stable state. The mechanism suppressing turbulent motions (mixing) could be a strong magnetic field. This suggests that lithium overabundances may be observed for magnetic Ap (CP) stars on the main sequence.

ACKNOWLEDGMENTS

We thank S. Sergeev for the possibility to use the SPE code for the spectral reduction, Prof. C. Cowley for providing us with data on rare-earth elements, and P. North for the spectra; D. Bord and J. Sugar for assistance and for providing data. We used R. Kurucz's data (CDROM 23) from the ADC NASA and VALD databases; we are grateful to the administrators of these databases, which are available on the Internet. One of us (V.V.T.) would like to thank A. Yakushechkin, President of the Master Games company, for sponsoring hardware and software used for the computations needed for this investigation. V.Kh. thanks the Slovak Academy of Sciences for partial financial support through VEGA grant no. 7107.

REFERENCES

1. R. Faraggiana, M. Gerbaldi, and F. Delmas, Astrophys. Space Sci. **238**, 169 (1996).
2. N. S. Polosukhina, D. Kurtz, M. Hack, *et al.,* Astron. Astrophys. **351**, 283 (1999).
3. N. Piskunov, Contrib. Astron. Obs. Skalnate Pleso **27** (3), 374 (1999).
4. V. Khokhlova, D. Vasil'chenko, *et al.,* FENAM-2000, 2000.
5. N. S. Polosukhina, A. V. Shavrina, M. Hack, *et al.,* Astron. Astrophys. **357**, 920 (2000).
6. A. V. Shavrina, N. S. Polosukhina, V. Tsymbal, and V. Khalak, Astron. Zh. **77** (4), 273 (2000) [Astron. Rep. **44**, 235 (2000)].
7. P. North, N. Polosukhina, V. Malanushenko, and M. Hack, Astron. Astrophys. **333**, 644 (1998).
8. D. W. Kurtz, F. van Wyk, and F. Maran, Mon. Not. R. Astron. Soc. **243**, 289 (1990).
9. D. W. Kurtz, F. van Wyk, G. Goberts, *et al.,* Mon. Not. R. Astron. Soc. **287**, 69 (1997).
10. S. Sergeev, private communication (1999).
11. V. V. Tsymbal, Odessa Astron. Publ. **7**, 146 (1994).
12. R. L. Kurucz, CDROM13; CDROM23 (1993).
13. R. L. Kurucz, Preprint No. 4080 (Harvard-Smithsonian Center for Astrophysics, 1995).
14. N. E. Piskunov, F. Kupka, T. A. Ryabchikova, *et al.,* Astron. Astrophys., Suppl. Ser. **112**, 525 (1995).
15. F. Kupka, N. E. Piskunov, T. A. Ryabchikova, *et al.,* Astron. Astrophys., Suppl. Ser. **138**, 119 (1999).
16. T. A. Ryabchikova, N. E. Piskunov, H. C. Stempels, *et al.,* Phys. Scr. **83**, 162 (1999).
17. J. Reader and Ch. H. Corliss, Line Spectra of the Elements 1980, NASA ADC, CDROM 3.
18. Ch. R. Cowley, private communication (1998).
19. D. Bord, Astron. Astrophys., Suppl. Ser. **144**, 517 (2000).
20. J. Sugar, private communication (1998).
21. J. Zverko, J. Žižňovský, and P. North, Contrib. Astron. Obs. Skalnate Pleso **28**, 109 (1998).
22. J. Zverko, J. Žižňovský, and P. North, in preparation (2000).
23. N. Grevesse and A. J. Sauval, Space Sci. Rev. **85**, 161 (1998).
24. S. N. Roby and D. L. Lambert, Astrophys. J., Suppl. Ser. **73**, 67 (1990).
25. T. A. Ryabchikova, J. D. Landstreet, M. J. Gelbmann, *et al.,* Astron. Astrophys. **327**, 1137 (1997).
26. S. Bagnulo, M. Landolfi, and E. Landi Degl'Innoncenti, Astron. Astrophys. **343**, 865 (1999).
27. G. Mathys, Astron. Astrophys. **293**, 746 (1995).

28. G. Mathys and S. Hubrig, Astron. Astrophys., Suppl. Ser. **124**, 475 (1997).
29. J. Babel, in *Peculiar Versus Normal Phenomena in A-type and Related Stars (IAU Colloquium No. 138)*, Ed. by M. M. Dworetsky, F. Castelli, and R. Faraggiana, Astron. Soc. Pac. Conf. Ser. **44**, 458 (1993).
30. Ch. R. Cowley and G. Mathys, Astron. Astrophys. **339**, 165 (1998).
31. J.-L. Tassoul, in *Theory of Rotating Stars* (Princeton Univ. Press, Princeton, 1978), p. 472.
32. J. Matthews, D. Kurtz, and P. Martinez, Astrophys. J. **511**, 422 (1999).
33. R. Kuschnig, T. A. Ryabchikova, N. E. Piskunov, *et al.,* Astron. Astrophys. **348**, 924 (1999).
34. N. S. Polosukhina and L. S. Lyubimkov, Mem. Soc. Astron. Ital. **66**, 361 (1995).
35. D. Lambert and S. Sawyer, Astrophys. J. **283**, 192 (1984).

Translated by N. Samus'

Astronomy Reports, Vol. 45, No. 10, 2001, pp. 797–803. Translated from Astronomicheskiĭ Zhurnal, Vol. 78, No. 10, 2001, pp. 915–921.

Parameters of the Dust Envelope of the Symbiotic Star CH Cygni

M. B. Bogdanov[1] and O. G. Taranova[2]

[1]*Saratov State University, ul. Universitetskaya 42, Saratov, 410601 Russia*
[2]*Sternberg Astronomical Institute, Universitetskiĭ pr. 13, Moscow, 119899 Russia*

Received January 22, 2001

Abstract—The brightness and color variations of the symbiotic star CH Cygni are studied, and its stationary, spherically symmetric, extended dust envelope is modeled based on long-term $UBVRJHKLM$ photometry, the mid-IR spectral energy distribution (7–23 μm), and far-IR fluxes measured by IRAS and ISO. The existence of a hot dust envelope, detected earlier in the near IR, is confirmed; the optical depth of the envelope has probably increased with time. Model fits to the IRAS and ISO data indicate that the V-band optical depth increased from 0.22 to 0.41 due to dust density enhancement during the 14 years between the observations by the two spacecraft. The mass-loss rate, gas-expansion velocity at the outer boundary of the envelope, and upper limit of the mass of the central source of emission are estimated assuming that the stellar wind of the system is driven by the pressure of the red giant's radiation on the dust, with subsequent momentum transfer to the gaseous medium. © *2001 MAIK "Nauka/Interperiodica"*.

1. INTRODUCTION

When studying the spectrum of the red giant CH Cyg in 1967, Deutsch [1] detected another source of emission that almost completely veiled the molecular absorption bands at short wavelengths. Since then, this unique symbiotic star has been a continuous object of study, and has been intensely observed at all wavelengths, from the X-ray to the radio. Yamashita and Maehara [2] discovered variability of the red giant's radial velocity with a period of $5750^{\rm d}$, while Luud and Tomov [3], who found lines due to the hot component in the spectrum of CH Cyg and measured their shifts, estimated the masses of the two stars. Based on thirteen years of high-resolution spectral observations at 2 μm, Hinkle *et al.* [4] concluded that the system was triple: the symbiotic pair has an orbital period of $756^{\rm d}$, and the third component—a yellow dwarf—is revolving around the common center of mass with a period of about 14.5 years. An analysis of visual and UV spectra and photometric data enabled Skopal *et al.* [5] to confirm that the system was triple and demonstrate that the symbiotic pair is eclipsing.

Most researchers believe that the hot component of the system is a white dwarf that is accreting material from the red giant. The luminosity of the resulting accretion disk appreciably exceeds the luminosity of an ordinary white dwarf. The emission from the hot component is highly variable. Together with irregular fluctuations, large increases of brightness followed by rapid declines are observed. The most powerful flare took place in 1984. By 1986, the hot component was essentially unobservable, and subsequent observations demonstrated a slow increase of its flux associated with a new activity cycle, which concluded with a less powerful flare in 1993 [6].

Infrared observations made soon after the detection of the hot component suggested the presence of dust in the system CH Cyg. According to the classification of [7], the object was attributed to type S—symbiotic stars without hot dust envelopes.

Since 1978, we have been obtaining regular photometric observations of CH Cyg in the near IR at the Crimean Laboratory of the Sternberg Astronomical Institute. Results obtained before 1998 and references to earlier publications are given in [6]. We have deduced that soon after the visual-brightness decline in 1984 a hot dust envelope appeared in CH Cyg [8]. Taranova [9] calculated a model for the dust envelope consisting of two thin spherical layers with fixed values for the optical depth and dust temperature. Later, in order to explain the near-IR flux variations, we considered the possibility that dust clouds were absorbing the red-giant emission [10, 11].

Here, we analyze the object's brightness and color variations in the visual and near IR throughout the

1063-7729/01/4510-0797$21.00

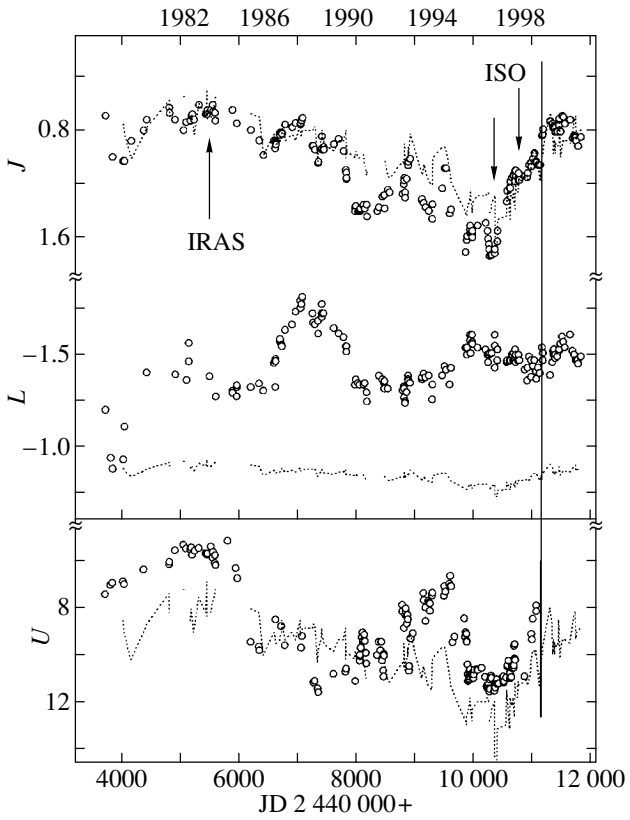

Fig. 1. Brightness variations of CH Cyg in the J, L, and U bands according to our observations in 1978–2000 (circles). The dotted curve shows calculated variations of the red-giant brightness associated with variations in the column density of dust (see text). The arrows show epochs of IRAS and ISO observations of the star. The 1999 and 2000 observations are shown to the right of the vertical line.

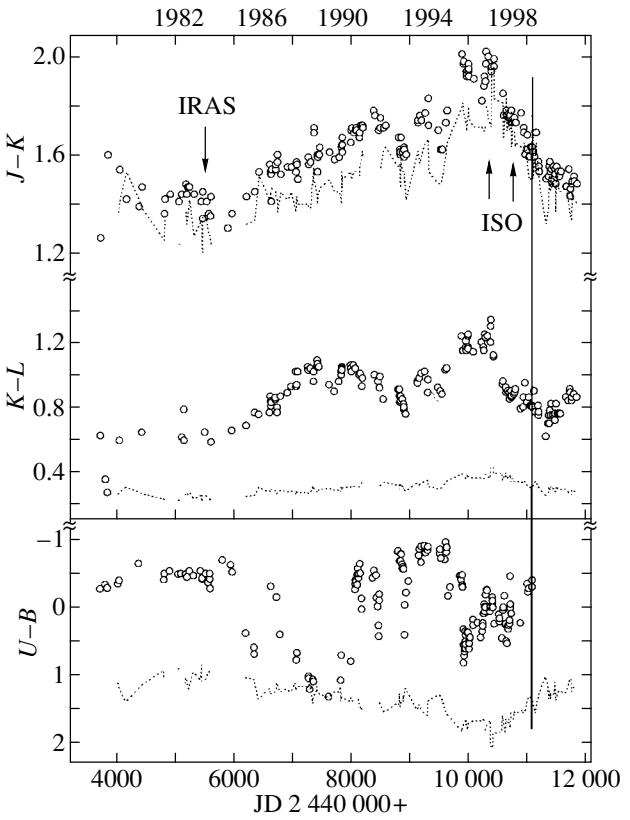

Fig. 2. Same as Fig. 1 for three color indices.

interval covered by our observations and model the extended, spherically symmetric dust envelope of CH Cyg using IRAS and ISO fluxes in the mid- and far-IR.

2. BRIGHTNESS AND COLOR VARIATIONS OF THE STAR IN THE VISUAL AND NEAR-IR

Figures 1 and 2 present the results of our photometric measurements of CH Cyg for the entire observation interval in the form of brightness and color curves. The arrows in the figures mark the epochs of IRAS and ISO observations. After 1998, we note the following features in the emission of the system. The J brightness increase that began in 1996 continued until mid-1999. On average, the brightness increased by approximately $0\overset{m}{.}6$ and, until the end of 2000, experienced fluctuations whose maximum deviation did not exceed $0\overset{m}{.}2$. The L brightness had a local minimum in 1999; it reached its 1996 level by mid-2000, then fell by $\sim 0\overset{m}{.}1$ by the end of 2000 (Fig. 1). The color index $J-K$ decreased from 1996 until the end of 2000; $K-L$ decreased until 1999, then slightly increased (Fig. 2).

The spectral energy distribution at 0.36–5-μm obtained by averaging data for almost a hundred nights with flux errors of less than 10% in the IR can be represented as the total emission from three sources: a normal M6 giant, a hot source whose $B-V$ is close to that of a B8V star, and a dust envelope with a temperature of $\sim$ 650 K. Observations at 1.25–1.65 μm indicate that the spectral type of the cool component can vary from M5III to M7III. An M5 spectrum was observed during the phase of maximum activity of the hot source in 1981–1985, while an M7 spectrum was observed when there were essentially no traces of the hot source's emission in the visual (1988). It is obvious that in the wavelength range covered by our observations, 0.36–5 μm, the hot source is manifested primarily in the U and B bands, the cool component in the J, H, and K bands; and the dust envelope in the L and M bands. We analyzed the parameters of these sources based on observations of the system made in 1978–1998 in [6].

Table 1. Mean magnitudes of CH Cyg and their deviations at times close the IRAS and ISO observations

Band	IRAS		ISO			
	JD 2 445 320 ± 170		JD 2 450 350 ± 13		JD 2 450 565 ± 15	
	Value	S.E.	Value	S.E.	Value	S.E.
U	5.63	0.04	11.48	0.05	10.69	0.18
B	6.11	0.03	11.47	0.03	10.52	0.02
V	5.64	0.03	9.95	0.02	8.94	0.00
R	4.33	0.03	7.65	0.00	–	–
J	0.67	0.01	1.72	0.01	1.3	0.03
H	−0.28	0.01	0.46	0.04	0.08	0.00
K	−0.75	0.01	−0.24	0.01	−0.50	0.00
L	−1.44	0.04	−1.51	0.04	−1.45	0.00
M	−1.58	0.06	−1.66	0.04	−1.55	0.01

Earlier, we proposed that the observed variability of the red giant in the near IR could be due to changes in the column density of dust [10, 11]. These changes are probably local, not involving the entire volume of the dust envelope, and are manifest as eclipses by dust clouds. The dotted curves in Figs. 1 and 2 show brightness and color variations of the star calculated assuming that the $J-H$ color variations are due solely to changes in the optical depth of the dust envelope along the line of sight. The adopted optical properties of the dust grains were similar to those of interstellar dust. We also assumed that in the absence of the dust envelope the J brightness of the cool component is $\sim 0\overset{m}{.}65$ (as it was near JD 2 445 320) and the spectral energy distribution coincides with that of a normal M6 red giant. These figures show that the observed brightness and color variations of CH Cyg in 1999 and 2000 are consistent with the conclusions formulated earlier in [6].

The mean magnitudes of CH Cyg in the visual and near IR at times close to the IRAS and ISO observations are listed in Table 1 together with their uncertainties.

3. OBSERVATIONAL DATA USED TO MODEL THE DUST ENVELOPE

As a basis for comparison with our models, we chose the spectral energy distribution of CH Cyg at 7–23 μm, for the following reasons. First, the accuracy of measurements in this range is rather high. Furthermore, the variability of the red giant is prominent in the near IR, and we expect a stronger influence of inhomogeneities in the dust envelope, including fluctuations of the column density of dust between the observer and the cool component. In the far IR, the optical depth of the envelope is small, and the optical characteristics of dust are not sufficiently well understood.

We retrieved 1983 data from the IRAS low-resolution spectrometer via the Internet from the database of the University of Calgary and corrected them taking into account the calibration [12]. The ISO low-resolution spectrum for May 10, 1997 and far-IR flux estimates for September 14, 1996 were also obtained via the Internet from the server of the orbiting observatory. There was one more low-resolution spectrum of CH Cyg in the ISO archive, obtained on December 3, 1996. Individual segments of this spectrum are not well matched, probably due to inaccurate calibration. Therefore, we could not use this spectrum when constructing the model of the dust envelope.

The observed spectral energy distributions of CH Cyg at 7–23 μm according to the IRAS and ISO data are shown by circles in Figs. 3 and 4. It is immediately apparent in Fig. 3 that the hot dust envelope already existed in 1983, when the accreting white dwarf was near the maximum of its activity. This is testified to by the characteristic silicate emission peak at $\lambda = 10$ μm. Another silicate peak at 19 μm is less prominent. The increase in the height of these peaks in 1997 (Fig. 4) suggests a growth in the optical depth of the envelope. This was due to an increase in the dust density, including that near the inner boundary of the envelope, rather than to additional absorption in a cool dust cloud.

4. CALCULATION OF THE DUST-ENVELOPE MODELS

The major difficulty in model calculations of circumstellar dust envelopes is the large number of

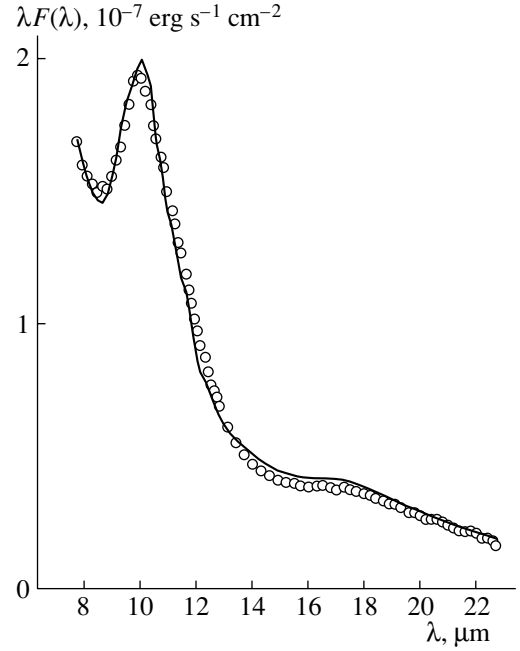

Fig. 3. Spectral energy distribution of CH Cyg measured by the IRAS low-resolution spectrometer (circles). The solid curves shows the energy distribution for the model dust envelope whose parameters are listed in Table 2.

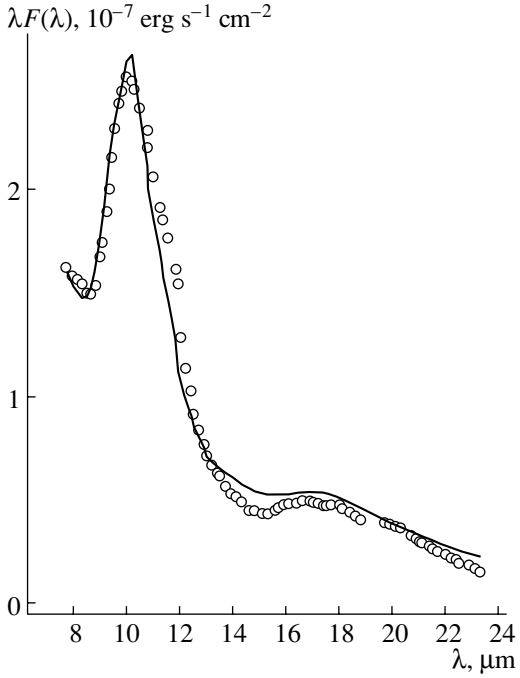

Fig. 4. Same as Fig. 3 for the ISO data.

parameters involved, whose values must be chosen based on a best agreement with the observations. Usually, it is desirable to reduce the number of parameters by using independent estimates for some of them. Since the CH Cyg system is well studied, some parameters can be considered to be fairly reliably known. We have adopted a luminosity and effective temperature for the M6III red giant of $L = 6900L_\odot$ and $T_{\rm eff} = 2850$ K [3]. The hot component of the CH Cyg system contributed less than 0.05 of the total bolometric flux, even when it was at its maximum luminosity, and was already virtually undetectable in the near IR. Therefore, we can assume that the properties of the dust envelope are determined by the emission of only one central source—the red giant.

We applied the usual assumptions when calculating models for the envelope using the IRAS and ISO data. We took the dust envelope to have a sharp inner boundary at a distance r_1 from the center, and the grain density to decrease in inverse proportion to the square of the distance out to the outer boundary of the envelope, at $r_2 = 1000r_1$.

We assumed that the optical characteristics of the material making up the grains are similar to those of "warm" silicates [13], and that their size distribution $n(a)$ is described by the MRN model [14]: $n(a) \propto a^{-q}$ for radii of spherical grains $a_{\rm min} \le a \le a_{\rm max}$ with $q = 3.5$, $a_{\rm min} = 0.005$ μm, $a_{\rm max} = 0.25$ μm. The central source was assumed to have a Planck spectrum corresponding to the effective temperature of the red giant.

We solved for the radiative transfer in the dust envelope using the DUSTY code (version 2.0) with grids of 30 points in radius and 99 points in wavelength, in the interval from 0.01 μm to 3.6 cm. The basic algorithm of this program is described in [15, 16]. The input model parameters were the dust temperature at the inner boundary T_1 and the optical depth τ_V of the envelope at 0.55 μm. After calculating the model spectral energy distribution, we chose the distance d that minimized the sum of the squared differences between the observed and model fluxes. Table 2 lists the best-fit values for the parameters of models for the IRAS and ISO data. The estimated distances are, in general, consistent with the value of 300 pc adopted earlier in most studies.

The solid curves in Figs. 3 and 4 show the model spectral energy distributions fitted to the data of the IRAS and ISO low-resolution spectrometers. The circles denote the observed fluxes. We can see that the models describe the observations fairly well. Figures 5 and 6 present a comparison with the observations over a broader spectral range. The solid curves show the logarithm of the flux (in erg s^{-1} cm^{-2} cm^{-1}) as a function of the logarithm of the wavelength (in μm) for the models fitted to the IRAS and ISO data. The circles show the logarithm of the flux according to data from the CIO catalogue and IRAS (Fig. 5)

Table 2. Model parameters of the dust envelope and stellar wind of CH Cyg derived by fitting the IRAS and ISO observations

Parameter	Models fitting the observations	
	IRAS	ISO
L, $L_\odot$	6900	6900
T_{eff}, K	2850	2850
T_1, K	900	900
r_1, 10^{14} cm	2.24	2.28
τ_V	0.22	0.41
d, pc	214	230
$\dot{M}$, $10^{-7}M_\odot$/year	4.5	7.3
V_e, km/s	11.0	12.4
M_{s}, $M_\odot$	0.7	0.9

and ISO (Fig. 6) photometry. Though we have not used these flux data in the model fitting, the calculated curves are fairly close to the observations at virtually all IR wavelengths. The asterisks in Figs. 5 and 6 show our own photometric measurements (Table 1). The fluxes in the near UV and visual are, in general, consistent with the model constructed using the IRAS data, but are appreciably lower than the model for the ISO data.

The optical depth of the dust envelope is small even in the visual and quickly decreases toward the IR. In particular, for the model fitted to the ISO data, the optical depth at 1 μm is only 0.12 it decreases to 0.02 in the K band ($\lambda_0 = 2.2$ μm). Nevertheless, there is no doubt that there is a difference in the optical depths of the envelope for the two models. During the 14 years between the IRAS and ISO observations, τ_V nearly doubled. Though there was an appreciable growth in the silicate-peak heights, the fluxes at both short ($\lambda = 8$ μm) and longer ($\lambda = 23$ μm) wavelengths remained virtually unchanged. In the framework of the model assumptions, such an increase in the optical depth of the envelope can be explained by a global increase in the dust density, including in regions near the inner boundary of the envelope.

5. DETERMINATION OF THE STELLAR-WIND PARAMETERS

To estimate the parameters of the stellar wind of CH Cyg driven by the radiation pressure on the dust, with subsequent momentum transfer to the gaseous medium, we applied the gas-dynamical operational mode of the DUSTY code using a source of emission with the parameters of the red giant and the derived values of the envelope optical depth. In this case, the program implements a self-consistent procedure to solve for the radiative transfer and motion of the dust in the circumstellar envelope [17]. We assumed a silicate density of $\rho_{\text{s}} = 3$ g/cm^3 and gas-to-dust mass ratio in the envelope $r_{\text{gd}} = 200$. Using these data, DUSTY calculates the total mass-loss rate $\dot{M}$, the gas-expansion velocity at the outer boundary of the envelope V_e, and an upper limit for the mass of the central source M_{s}. The stellar-wind parameters for various models are also listed in Table 2. If needed, they can easily be recalculated for other values of ρ_{s} and r_{gd} using the relations $\dot{M} \propto (\rho_{\text{s}} r_{\text{gd}})^{1/2}$, $V_e \propto (\rho_{\text{s}} r_{\text{gd}})^{1/2}$, and $M_{\text{s}} \propto (\rho_{\text{s}} r_{\text{gd}})^{-1}$ [17].

The mass-loss rate of the red giant was small even in 1997, and was about a factor of 1.5 lower near the epoch of maximum brightness of the hot source. Note that we have considered only the stellar wind driven by the red giant's radiation pressure on the dust formed in its outer layers. The outflow of matter related to the activity of the hot component activity should be added to this. This outflow is probably channeled near the rotational axis of the accretion disk. It is possible that precisely this outflow shapes the bipolar structure observed in the radio. Therefore, the values of $\dot{M}$ listed in Table 2 should be considered lower limits for the true mass-loss rate of the symbiotic system.

Our upper limits for the mass of the central source of emission M_{s} are fairly low. According to the estimates of Luud and Tomov [3], the sum of the masses of the components of CH Cyg is close to $4.1M_\odot$. However, these estimates were made using an incorrect period for the symbiotic system, and cannot be considered trustworthy. By virtue of the details of the gas-dynamical mode calculated by DUSTY, the dust-envelope parameters depend only weakly on the gravity for small masses; in turn, this results in a large

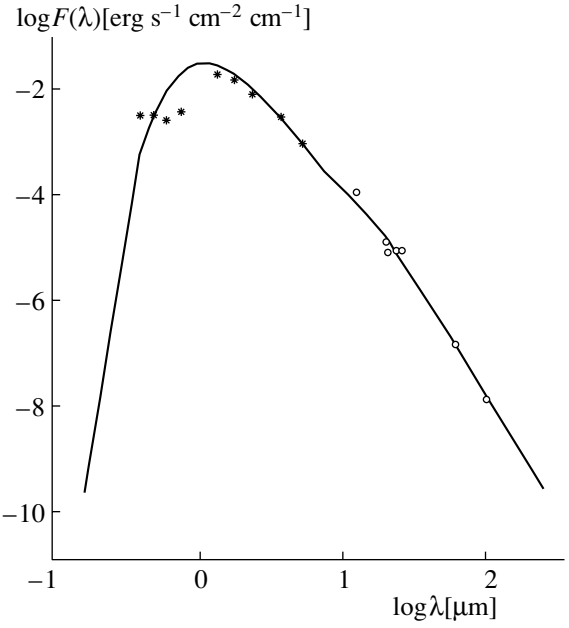

Fig. 5. Broadband spectral energy distribution of CH Cyg according to CIO and IRAS data (circles) and our observations (asterisks). The solid curve shows the model distribution fitted to the IRAS data.

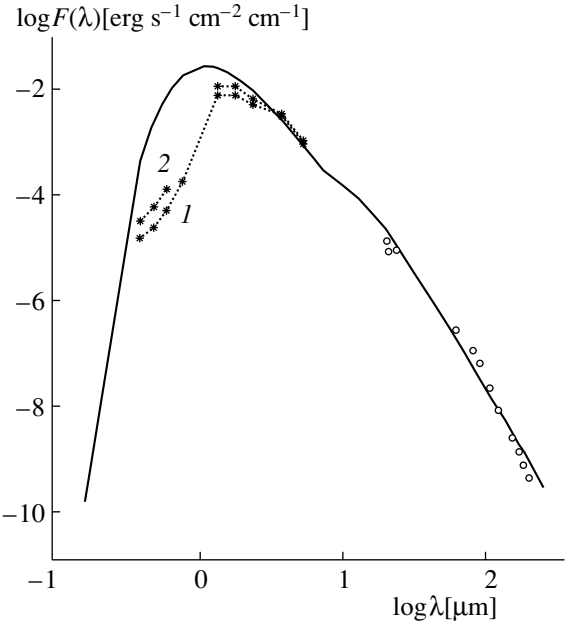

Fig. 6. Broadband spectral energy distribution of CH Cyg according to CIO and ISO data (circles) and our observations (asterisks). The solid curve shows the model distribution fitted to the ISO data.

uncertainty in the derived upper limit for the mass of the central body.

Even if we adopt $2M_\odot$ for the sum of the component masses, the period of 756^d corresponds to a semi-major axis for the orbit of 3.1×10^{13} cm, which is obviously smaller than the radius r_1 of the inner boundary of the dust envelope. Therefore, the luminosity of the hot component cannot be related to the mass-loss rate of the red giant due to its gas–dust stellar wind. Apparently, the accretion disk is mainly replenished with gas flowing through the inner Lagrange point, and its luminosity variations reflect changes in the density of matter at the boundary of the red giant's Roche lobe. The orbital motion of the white dwarf at an average velocity of about 30 km/s takes place inside the extended atmosphere of the red giant and could affect the accretion-disk dynamics. This motion could also result in the formation of a shock wave; radiation from the post-shock gas may be manifest in the visual.

6. CONCLUSION

Our model fitting of IRAS and ISO data shows that observations of CH Cyg in the mid-IR and far-IR are described fairly well by a model with an extended, spherically symmetric dust envelope surrounding the cool component of the system. The evolution of the mid-IR spectrum of the envelope on a time interval of 14 years suggests an enhancement in the dust-grain column density. During this time, the optical depth of the envelope in the visual nearly doubled, implying a corresponding increase in the mass-loss rate of the red giant. The hot component of the CH Cyg system is located inside the dust-condensation boundary in the envelope, and its activity is not related to the gas–dust stellar wind of the red giant.

ACKNOWLEDGMENTS

The authors are grateful to astrophysicists of the University of Kentucky (Željko Ivezić, Maia Nenkova, Moshe Elitzur) for the opportunity to use the DUSTY code to solve the radiative transfer equation, as well as to the staff of the SIMBAD, University of Calgary, and ISO databases for granting access to the observational data on CH Cyg. The work was partially supported by the Russian Foundation for Basic Research (project code 00-02-16272), the Federal Research Program in Astronomy, and the Ministry of Education of Russia.

REFERENCES

1. A. J. Deutch, IAU Circ., No. 2020 (1967).
2. Y. Yamashita and H. Maehara, Publ. Astron. Soc. Jpn. **31**, 307 (1979).
3. L. Luud and T. Tomov, Pis'ma Astron. Zh. **10**, 860 (1984) [Sov. Astron. Lett. **10**, 360 (1984)].

4. K. H. Hinkle, F. C. Fekel, D. S. Johnson, and W. W. G. Schrlach, Astron. J. **105**, 1074 (1993).
5. A. Skopal, M. F. Bode, H. M. Lloyd, and S. Tamura, Astron. Astrophys. **308**, L9 (1996).
6. O. G. Taranova and V. I. Shenavrin, Astron. Zh. **77**, 525 (2000) [Astron. Rep. **44**, 460 (2000)].
7. B. L. Webster and D. A. Allen, Mon. Not. R. Astron. Soc. **171**, 203 (1975).
8. O. G. Taranova and B. F. Yudin, Astrophys. Space Sci. **146**, 33 (1988).
9. O. G. Taranova, Pis'ma Astron. Zh. **17**, 253 (1991) [Sov. Astron. Lett. **17**, 107 (1991)].
10. O. G. Taranova and B. F. Yudin, Astron. Zh. **69**, 262 (1992) [Sov. Astron. **36**, 132 (1992)].
11. O. G. Taranova, B. F. Yudin, and E. A. Kolotilov, Pis'ma Astron. Zh. **21**, 529 (1995) [Astron. Lett. **21**, 470 (1995)].
12. M. Cohen, R. G. Walker, and F. C. Witteborn, Astron. J. **104**, 2030 (1992).
13. V. Ossenkopf, T. Henning, and J. S. Mathis, Astron. Astrophys. **261**, 567 (1992).
14. J. S. Mathis, W. Rumpl, and K. H. Nordsieck, Astrophys. J. **17**, 25 (1977).
15. Z. Ivezic and M. Elitzur, Mon. Not. R. Astron. Soc. **287**, 799 (1997).
16. Z. Ivezic and M. Elitzur, Mon. Not. R. Astron. Soc. **303**, 864 (1999).
17. Z. Ivezic and M. Elitzur, Astrophys. J. **445**, 415 (1995).

Translated by G. Rudnitskiĭ

Astronomy Reports, Vol. 45, No. 10, 2001, pp. 804–815. Translated from Astronomicheskiĭ Zhurnal, Vol. 78, No. 10, 2001, pp. 922–933.

Six-Day Modulation of the Quiescent Radio Emission of SS 433

S. A. Trushkin, N. N. Bursov, and Yu. V. Smirnova

Special Astrophysical Observatory, Russian Academy of Sciences, Nizhni Arkhyz, Stavropol kraĭ, 357147 Russia

Received February 7, 2001

Abstract—Two daily sets of monitoring data of the Galactic X-ray binary SS 433 (V1343 Aql) obtained on the RATAN-600 radio telescope (117 days in 1997 and 120 days in 1999) show variations in its quiescent radio emission with a period of 6.05 ± 0.1 days at six frequencies from 0.96 to 22 GHz. This 10–15% modulation in the quiescent radio light curves differs significantly from the well-known 6.28-day periodicity in the emission of moving spectral features and in optical photometric data, which are related to nodding motions of the jets and accretion-disk wobble. This period coincides almost exactly with the theoretical value for the harmonic $f = 2\,(I_o + I_p)$, related to the orbital ($T_o = 13.08$ days) and precessional ($T_p = 162.4$ days) periods for slaved accretion-disk models. The 6.06-day period corresponds to the combined frequency. It is proved that the modulation of the radio flux of SS 433 may be associated with relativistic boosting of the jet emission due to periodic variation of the orientation of the jets, which are nodding with a period of six days. The synchrotron emission of the two jets contributes to the quiescent radio flux of SS 433, and the six-day harmonic has the same radio spectrum as the quiescent radio flux: $S_\nu \sim \nu^{-0.6}$. © *2001 MAIK "Nauka/Interperiodica".*

1. INTRODUCTION

In 1978, the bright, variable emission-line star number 433 from the catalog of Stephenson and Sanduleak [1] was identified with the bright, compact radio source 1909+048, located at the center of the supernova remnant W50 [2]. This binary system with a period of 13.08 days consists of a degenerate star with an accretion disk and a massive main component that fills its Roche lobe. The supercritical regime of accretion onto the degenerate star results in two precessing jets of material flowing outward in opposite directions from the accretion-disk poles with a velocity of about a quarter of the velocity of light ($v = 0.26c$). These jets, initially detected in optical spectroscopic observations, are visible as extended structures in images of the X-ray and radio brightness distributions. Non-stationary phenomena in the binary system SS 433 result in strong variability of its emission at all wavelengths.

The variable synchrotron radio emission of SS 433 is generated in the jet outflows, where magnetized clouds (plasmons) of relativistic charged particles are formed [3]. This has been reliably established by the negative spectral index and strong linear polarization of the radio emission. The total radio luminosity of SS 433 is 10^{32} erg/s, which is three, five, and eight orders of magnitude lower than the luminosity in the X-ray, visual, and ultraviolet bands [4].

This object has two powerful jets precessing with a period of 162.5 days, made up of clumps of material ejected from the central system, which penetrate through a dense thermal envelope, with relativistic electrons generated along the path of the jet outflows.

As early as 1980, in a first long cycle of observations devoted to searches for fluctuations in the cosmic microwave background carried out at the declination of SS 433 ($\delta_0 = +04°57'$) using the fixed antenna and feed cabin of the RATAN-600 telescope [5], we noticed weak, quasi-periodic variations of the flux level of SS 433. In this observation mode, even weak flux variability of radio sources in very quiescent states could be established over a range of frequencies from 4 to 14 GHz. The absence of bright flares enabled a Fourier analysis of the radio brightness curves of SS 433. For 60 days in February–March, 1980 a weak six-day harmonic was detected in the spectrum; however, this harmonic was not detected at a significant level in the entire 100-day light curve.

Let us note other periodicities in the radio emission of SS 433. First, there is a periodicity in interferometric images of the SS 433 radio jets. The trajectories of the bright clouds (plasmons) making up the jet are suggestive of a precessing central engine ejecting clouds at a constant velocity and periodically (162.5 days) rotating, creating the characteristic corkscrew structure visible in radio maps of SS 433.

1063-7729/01/4510-0804$21.00

In other words, the radio jets follow ballistic trajectories predicted by a kinematic model for the jet outflows [4]. It is important that the plasmons are initially bright, decline in brightness, then frequently brighten again some five to six days after their appearance [6, 7]. Further, the emission of these plasmons fades with time in accordance with a power law.

It is not always possible to find counterparts of the radio plasmons in the light curve of SS 433; i.e., the time for emergence of a plasmon extrapolated back using its proper motion does not always coincide with a prominent feature in the total radio flux curve [8]. One explanation for this is that there is a quasi-continuous injection of small plasmons into the jets visible in VLBI maps, which does not lead to appreciable variations in the total flux. It is probable that these small plasmons make the dominant contribution to the quiescent flux from SS 433.

The radio emission of SS 433 has been studied many times: correlations between optical and radio flux variations have been found [9], two-frequency light curves obtained [10, 11], and changes in the radio spectrum over a broad frequency range studied [12–15]. Prior to the current work, neither regularity in the occurrence of bright flares nor modulation of the integrated radio emission with the characteristic orbital and precession periods were found.

2. OBSERVATIONS AND DATA PROCESSING

The observations were carried out during a program to monitor a sample of microquasars, which have been widely discussed since the detection of the two Galactic superluminal sources GRO J1655–40 and GRS 1915+105 [16, 17]. We used a common complex of continuum radiometers on the primary feed of the RATAN-600 telescope. The 3.9, 7.7, 11.2, and 21.7-GHz receivers were cooled to 15–20 K using closed-loop cryogenic systems. Low-noise transistor (HEMT) amplifiers were used in the uncooled 0.96 and 2.3-GHz radiometers. In 1999, to reduce narrow-band interference in the bandpass of these radiometers, their frequency ranges were divided into narrow filter subchannels using signal processors. Table 1 lists the realized sensitivity (with optimal smoothing and in the absence of interference) for a single passage of the source across the fixed beam. We emphasize that in all frequency bands the beam is sufficiently narrow to include no more than one source as bright as SS 433 at a given time.

The observations were carried out on the Northern sector of the RATAN-600 telescope from May 1 to August 30, 1997, daily at the source culmination; i.e., at the beginning of the cycle at UT $= 2^h$ and at the end at UT $= 22^h$. In the second session, SS 433 was investigated using fixed-focus observations from April 23 to August 31, 1999. Other things being equal, this observing mode provides the higher stability of the antenna parameters. Obviously, we simultaneously recorded the source flux at four to six frequencies during one daily observation.

Table 1. Flux-density sensitivity of the RATAN-600 telescope

Wavelength, cm	31.2	13.0	7.6	3.9	2.7	1.38
Frequency, GHz	0.96	2.3	3.9	7.7	11.2	21.7
ΔS, mJy	25	15	5	8	10	20

Table 2. Flux densities of the calibration sources

Name	ν, GHz					
	0.96	2.3	3.9	7.7	11.2	21.7
	S_ν, Jy					
0134+32 (3C 48)	21.9	10.91	6.88	3.63	2.50	1.2
0237–23	6.75	5.05	3.9	2.75	2.30	1.5
0518+16(3C 138)	11.3	6.7	4.15	3.00	2.10	1.15
0624–05(3C 161)	24.1	12.8	8.11	4.16	2.76	1.3
1328+30(3C 286)	17.5	11.2	8.4	4.50	3.50	2.57
1648+04(3C 348)	69.0	28.1	15.8	7.20	4.6	–
NGC7027	1.0	2.5	4.5	6.50	6.1	5.8
2127+04	4.5	3.0	2.3	1.45	1.1	–

The flux calibration was carried out using various sets of calibrators, which usually included PKS 1345+12, PKS 1810+04, and PKS 2127+04. During a cycle, we often observed secondary standard calibrators: PKS 0237–23, 3C 138, 3C 161, 3C 48, 3C 348, 3C 286, and NGC 7027. We computed flux densities using formulas for the accurate radio astronomical flux scale of the reference sources [18, 19]. The adopted fluxes of the reference sources for a given measurement cycle are listed in Table 2. Overall, our daily calibration of the antenna and radiometer against the reference sources enabled us to reduce the total error of the measured fluxes of SS 433 to 3–4% over the entire frequency range observed.

The recordings obtained were reduced using the standard processing packages (*fgr* and *prat*) and scripts written in the *shell* command language. We reduced all records to flux densities using the daily calibrations and reference sources. The resulting calibration curve was also Fourier analyzed to remove systematic effects in the flux-density calibration. Tables 3 and 4 present the measured flux densities of

Table 3. RATAN-600 flux densities of SS 433 measured in 1997

Date MJD	ν, GHz				Date MJD	ν, GHz			
	11.2	7.7	3.9	2.3		11.2	7.7	3.9	2.3
	S_ν, mJy					S_ν, mJy			
50569.07	250	380	426	565	50627.91	233	250	475	625
50570.07	125	270	319		50628.91	233	190	381	562
50571.07	142	250	281	397	50629.91	200	170	429	481
50573.06	125	320	268	411	50631.90	233	250	395	536
50574.06	200	320	331	406	50635.89	225	180	364	524
50575.06	233	470	336	478	50637.89	200		420	671
50576.05		590	347		50640.88		120	229	
50577.05	175	490	322	488	50641.87	150	170	371	454
50578.05	250	290	339	479	50643.87	217	220	367	488
50579.05	242	280	410	489	50645.86	192	260	361	473
50580.05	250	320	445	593	50647.86	150	180	343	490
50581.04	208	430	395	557	50649.85	225	270	385	528
50582.04	275	460	389	599	50651.85	175	290	379	505
50583.04	267	470	422	674	50655.84	150	200	343	475
50584.03	275	530	408	591	50657.83	175	210	414	449
50585.03			432		50660.82	208	290	400	598
50589.02	233	290	476	611	50662.82	217	360	403	575
50591.01	267	270	389	553	50664.81	175	190	296	391
50593.01	233	370	425	565	50666.81	192	250	382	447
50597.99	225	300	431	546	50668.80	192	290	361	453
50599.99	192	270	391	535	50670.80	158	230	329	420
50601.98	233	310	502	667	50672.79	233	330	424	455
50603.98	225	380	412	654	50673.79	258	390	450	571
50604.98	208	320	446	585	50674.78	267	350	484	632
50605.97	200	270		625	50675.78	208	370	381	585
50607.97	242		440	649	50676.78	183	290	341	638
50609.96	192	240	441	638	50677.78		310	377	423
50611.96	225		405	605	50678.78		280	411	423
50613.95	225	270	425	558	50679.77		330	425	425
50615.95	167	220	377	488	50680.77		340	400	531
50617.94	200	140	453	571	50681.77		220	345	414
50619.94	183	170	355	613	50682.77		260	373	394
50621.93	192	110	345	528	50683.76		320	387	444
50623.92	192	210	312	524	50685.75		370	434	564
50625.92	233	250	441	627	50686.75		400	468	625

SS 433 (in mJy) at various frequencies as functions of the modified Julian day MJD = JD−2 400 000.5. In the Fourier analysis, we used the procedure *four* from the *fgr* package (author O. V. Verkhodanov), a program for calculating the power spectrum with different smoothing windows kindly granted by P. G. Tsy-

Table 4. RATAN-600 flux densities of SS 433 measured in 1999

Date MJD	ν, GHz						Date MJD	ν, GHz					
	21.7	11.2	7.7	3.9	2.3	0.96		21.7	11.2	7.7	3.9	2.3	0.96
	S_ν, mJy							S_ν, mJy					
51291.10	225	300	377	604	825	1230	51355.89	260	281	361	520	702	1138
51292.10	205	315	366	605	840	1395	51356.89	121	362	366	537	768	
51293.09	256	300	384	563	725	1330	51357.89	278	305	359	546	723	1208
51294.09	203	270	378	561	820	1345	51358.89	187	304	381	515	746	1212
51295.09	129	310		649	760	1370	51359.88	146	255	346	469	677	1232
51297.08	126	420		737	906	1250	51360.88	101	264	344	503	639	1229
51298.08	250	370	400	694	970	1535	51361.88	212	260	358	524	754	1102
51299.08				830	925	1462	51362.87	155	346	380	582	731	1491
51300.08	470	570		1545	1615	2050	51363.87	129	259	426	639	775	1109
51301.07	405	551		1092	1644	2230	51364.87	178	280	406	566	767	1180
51302.07		498	642	908	1420	2372	51365.86	127	255	389	544	741	1339
51303.06	405	691	873	1179	1771	2565	51366.86	180	281	358	598	844	1336
51304.06	288	611	823	1170	1846	1977	51367.86	155	315	424	623	803	1290
51306.05	289	564	677	1161	1534	2466	51368.85	202	346	427	654	908	1358
51307.05	413	623	717	1038	1477	2332	51369.85	105	323	412	616	864	1093
51308.04	336	668	530	853	1293	2210	51370.85	136	343	393	550	772	1342
51309.04	503	997	1005	1149	1430	2078	51371.85	180	326	407	595	751	1436
51310.03	385	686	933	1214	1635	2038	51372.84	259	362	446	628	861	1467
51311.03	481	755	870	1240	1915	2253	51373.84	197	380	436	674	874	1333
51312.02	453	743	843	1231	1881	2195	51374.84	187	336	449	614	821	1154
51313.02	498	625	718	1082	1753	3143	51375.83	89	285	373	563	730	1291
51314.02	363	541	675	967	1499	3042	51376.83	74	251	339	537	678	1201
51315.02	306	461	610	967	1383	2175	51377.83	163	196	376	487	659	1030
51316.02	297	451	554	879	1221	2526	51378.83	108	334	400	566	679	1384
51317.02	358	483	520	835	1175	2318	51380.83	185	356	393	588	776	1302
51318.01	256	519	573	799	1091	2106	51381.83	293	287	381	580	712	1273
51319.01	281	423	509	711	1127	1987	51382.83	183	337	399	539	764	1267
51320.01	319	359	474	646	980	1860	51383.83	92	269	372	521	742	1194
51321.02	296	380	454	683	950	2038	51384.83	214	290	308	529	702	1054
51322.01	186	316	418	646	949	1652	51385.83	171	285	323	529	714	1135
51324.01	144	335	405	602	906	1526	51386.83	145	238	348	551	731	1338
51325.01	202	376	459	626	896	1659	51387.83	148	305	352	568	804	1273
51326.01	222	371	417	633	874	1835	51388.83	139	263	345	550	738	1413
51327.01	246	355	423	611	849	1318	51389.82	124	264	346	550	768	1171
51328.01	258	359	427	600	894	1461	51390.82	165	316	391	609	896	

bulev, and the *spctrm* subroutine from [20]. All these programs use an FFT algorithm for 2^n regular points. In our case, the flux-density series were expanded to 128 points with zero values.

Our processing of the flux-density series at various frequencies in the 1997 and 1999 cycles (Tables 3, 4) using these three programs yielded power spectra that do not show any systematic differences.

Table 4. (Contd.)

Date MJD	ν, GHz						Date MJD	ν, GHz					
	21.7	11.2	7.7	3.9	2.3	0.96		21.7	11.2	7.7	3.9	2.3	0.96
	S_ν, mJy							S_ν, mJy					
51329.01	268	359	416	576	871	1431	51391.82	199	313	469	664	885	1681
51330.00	249	339	435	563	874	1580	51392.82	148	400	437	671	878	1325
51331.00	125	364	424	607		1386	51393.81	188	356	463	670	887	1789
51331.99	136	369	389	593	822	1212	51394.80	221	287	337	493	738	1058
51332.99	341	355	437	559	810	1372	51396.80	134	283	373	568	771	1281
51333.99	209	345	376	527	788	1090	51397.80	169	303	391	543	749	1161
51334.99	112	367	347	483	699	1452	51398.79	93	353	406	576		1060
51335.98	174	241	305	482	722	1380	51399.79	128	286	387	563	794	1379
51336.98	199	291	340	491	722	1173	51400.79	119	358	395	541	789	1247
51337.97	171	287	331	521	716		51401.79	118	326	347	544	763	1166
51338.97	233	339	398	552	748	1412	51402.79	191	316	371	583	771	1317
51339.97	199	367	412	559	726	1419	51403.78	147	339	405	592	818	1484
51340.96	189	291	373	558	748	1357	51404.78	97	352	435	593	841	1546
51341.96	210	263	328	556	807	1370	51405.78	110	287	380	597	834	1317
51342.95	199	280	378	542	804	1344	51406.77	186	276	399	577	781	1152
51343.95	155	334	371	600	817	1280	51407.77	134	305	359	550	729	1171
51344.93	238	321	428	589	758	1377	51408.77	118	228	334	589	801	1251
51345.93	205	349	356	582	789	1723	51409.77	112	262	386	596	801	1195
51346.92	184	335	361	522	809	1699	51410.76	152	291	447	607	944	1340
51347.92	130	353	367	520	674	1513	51412.76	109	319	334	540	766	1424
51348.92	199	277	361	495	673	1122	51413.76	237	293	362	516	842	1312
51349.91	154	314	383	546	750	1209	51416.75	208	253	366	536	753	1358
51350.91	121	305	389	520	732	1372	51417.75	93	279	352	535	765	1169
51351.91	206	292	397	527	703	1199	51420.75	127	180	272	458	589	1298
51352.90	155				595		51421.75	49	281	253	435	715	1116
51353.90	162	248	330	450	661	1097							

2.1. Spectral Analysis

Periodic fluctuations of the optical brightness of SS 433 have been extensively studied [21, 22]. Brightness fluctuations of 0.2^m with a rather precisely established period of 6.288 days have been found. This period corresponds to a combination of the frequency of the 162.5-day precessional period and the doubled frequency of the 13.08-day orbital period.

After adopting the kinematic model for the precessing relativistic jets [23], considerable deviations (up to 3000 km/s) of the model from the observed Doppler shifts of emission lines from the jet material have been found. These were correctly attributed to additional short-period oscillations of the jets, similar to a nutation motion of the stellar axis. If the accretion disk follows the nodding of the primary star, the jets also nod. At the same time, the nodding period was determined from spectral observations of moving emission features by Ciatti *et al.* [24] and Mammano *et al.* [25], who found 6.28 and 6.06-day oscillations. Earlier, Katz *et al.* [26] also found periods of 5.83 and 6.29 days in their studies of moving emission features. Newsom and Collins [27, 28] confirmed these periods, though they attributed both periodicities to a single global motion with a period of about six days.

Again, we note that the 6.28-day period results from a combination of the 162.5-day period and the 13.08-day orbital period, $f = 2f_o + f_p$. Katz *et al.* [26] noted that a modulation at a frequency of $f = 2f_o + 2f_p$ is also possible. This corresponds to a period of 6.06 days. Collins *et al.* [29] emphasized that the precessing object should rotate with a six-day semi-synodic period, in which case the orbital rotation and precession are oppositely directed. Matise and Whitemire [30] discussed nutation and pseudo-regular precession and showed that, in a model with a slaved disk and the known geometry of the binary

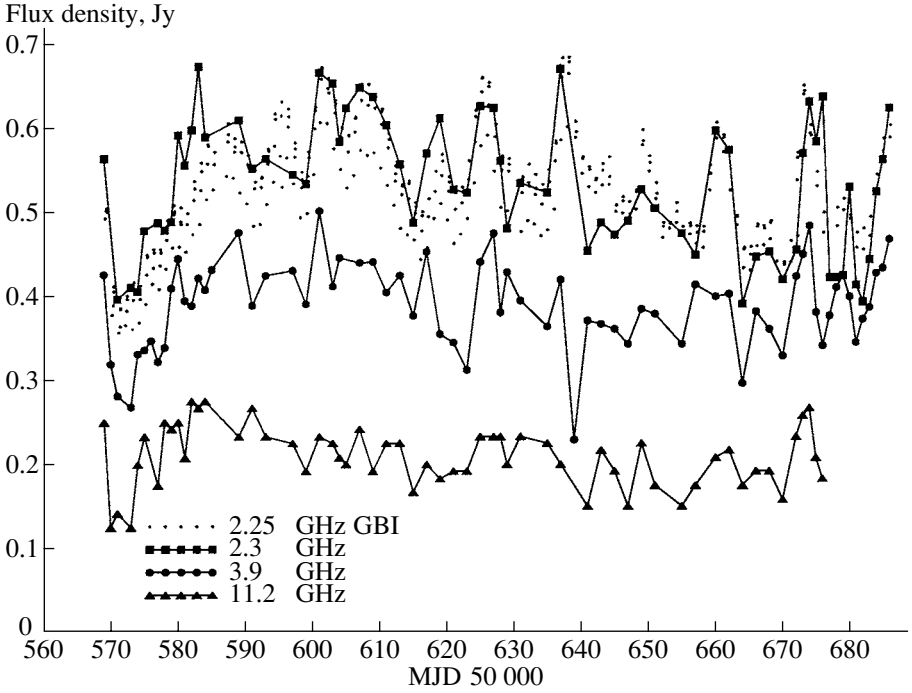

Fig. 1. Flux density variations of SS 433 in May–August 1997 at 2.25, 2.3, 3.9, and 11.2 GHz. May 1st corresponds to Julian date MJD 50 569.07.

system, a 6.06-day period should be present in all observed jet-related phenomena, while other similar periods are derived from this basic period, directly related to the jets.

Figures 1 and 2 show the initial measured light curves at various frequencies. We also used publicly available 2.25-GHz data obtained in the same time intervals on the NRAO Green Bank Interferometer.

Figure 3 presents light curves of the relative flux $\Delta S_\nu/\langle S_\nu\rangle$ measured at various frequencies in June–August 1999. A mutual correlation of the radio-flux variations without any frequency-dependent systematic time shifts is readily visible. The correlation coefficients are, on average, 0.8. This is a very important point in the interpretation of small radio brightness fluctuations. A delay throughout the observed frequency range is characteristic of bright flares in SS 433 and other microquasars, with the shift being as long as several days at frequencies from 1 to 22 GHz. Therefore, we should look for explanations of the small fluctuations not in the theory of the jet-plasmon evolution, as is usually done for radio flares, but in other frequency-independent physical models.

We believe the solution to this problem is relativistic boosting of the jet emission. We have used the usual five-element model of the jet kinematics [4] with the ephemerides of the jet nodding motions proposed by Vermeulen [31], who, in turn, used the data on the nodding motions of the SS 433 jets from [26]. These nodding motions are due to nutation of the rotational axis of the normal star, associated with perturbations from the secondary component of the binary system. These short-period motions are superimposed on the jet precession with its 162.5-day period. Figure 2 also presents a model calculation of the expected flux-density modulation arising from Doppler boosting of the emission in the relativistic jets.

Further, we removed long-scale trends in the initial light curves using a second- or third-power polynomial approximation and calculated the Fourier power spectra from the daily light curves of SS 433 at each frequency and for each cycle separately, applying various spectral windows (Bartlett, Walsh, Kaiser). The very rare gaps in the uniform series of observations were filled via linear interpolation of the adjacent data. We took the light curves at 2.3, 3.9, 7.7, 11.2, and 21.7 GHz in the intervals MJD 50 570–50 640 for 1997 and MJD 51 337–51 420 for 1999 for the spectral analysis.

Figure 4 shows the power spectrum for the 3.9-GHz light curve of SS 433 for June 7 to August 30, 1999 plotted in terms of relative amplitudes. For comparison, the power spectrum for the mean calibration curve (multiplied by a factor of ten) found from the complete set of calibration sources for each day in the same time interval is also shown. It is obvious that the specific parameters used in the data processing and reduction of the observations to actual fluxes do

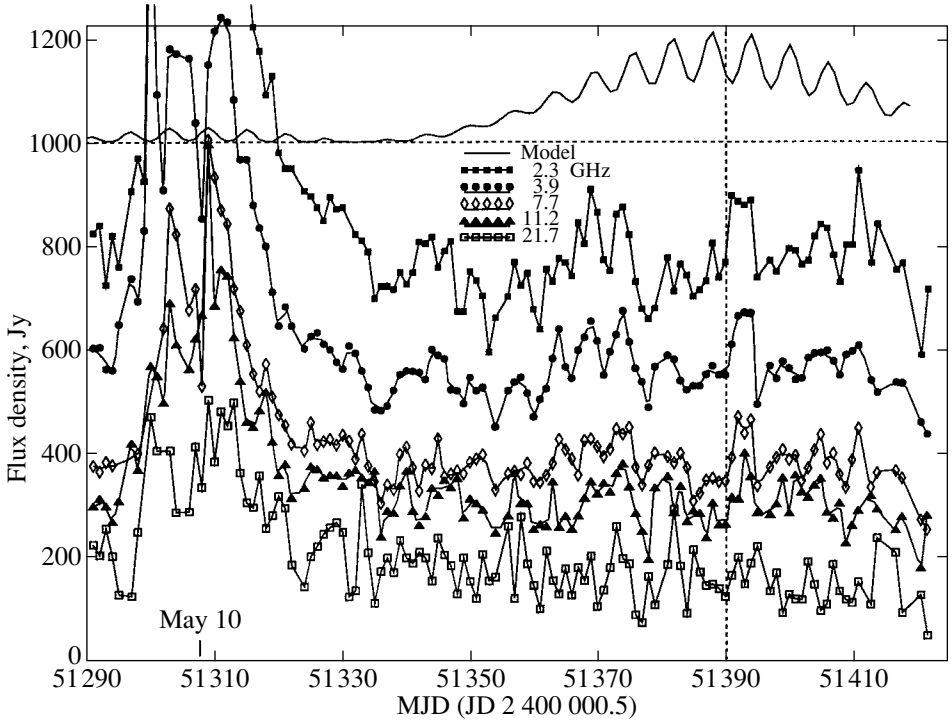

Fig. 2. Light curves of SS 433 in its quiescent state during May–August 1999 at various frequencies. Top: model light curve, normalized to 1000 (see text). At the beginning of the cycle, there was a powerful flare at all frequencies.

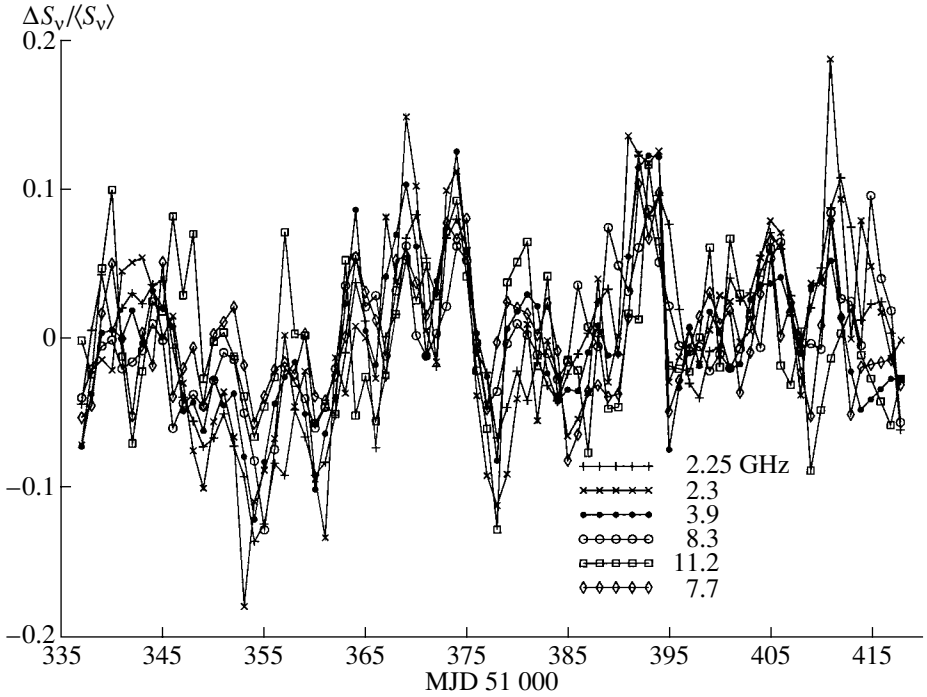

Fig. 3. Relative light curves $\Delta S_\nu/\langle S_\nu\rangle$ of SS 433 in June–August 1999 at various frequencies.

not affect our detection of the six-day harmonic in the power spectrum of the light curve of SS 433.

The power spectra of the light curves contain a bright harmonic at 0.166 ± 0.02 day^{-1} in both cycles (Figs. 2 and 6), which corresponds to a period of 6.05 ± 0.1 days UT. It is interesting that the radio spectrum of the harmonic amplitudes in 1997 repeats the total radio spectrum of the quiescent state, where-

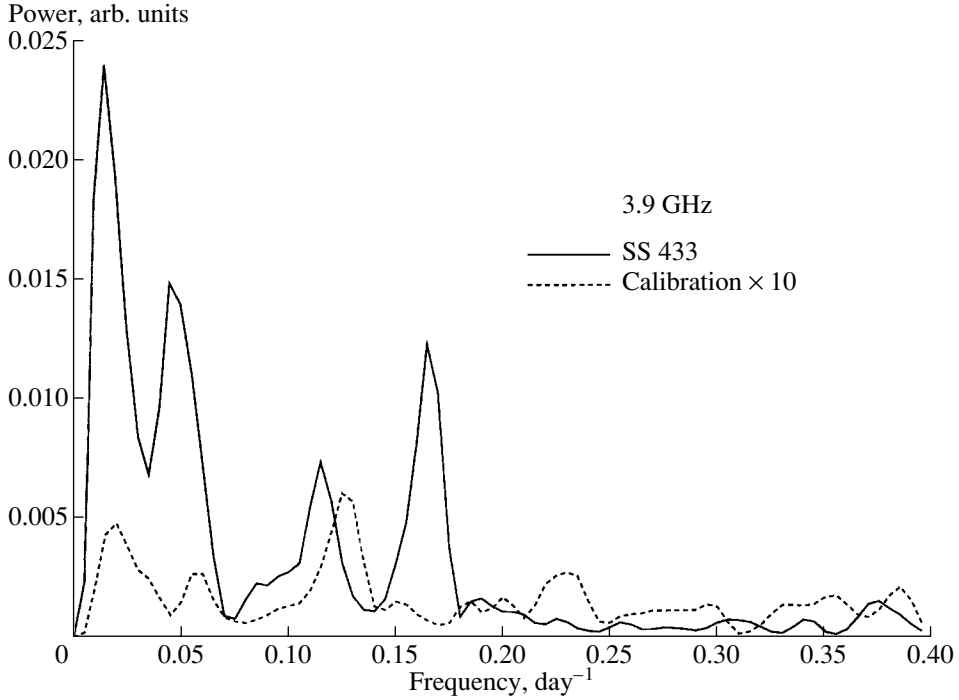

Fig. 4. Power spectrum of the light curve of SS 433 (relative amplitudes) at 3.9 GHz from June 7 to August 30, 1999 and the power spectrum for the average calibration curve, derived from the total set of calibration sources for each day during the same time interval. For clarity, the amplitude of the calibration power spectrum is magnified by a factor of ten.

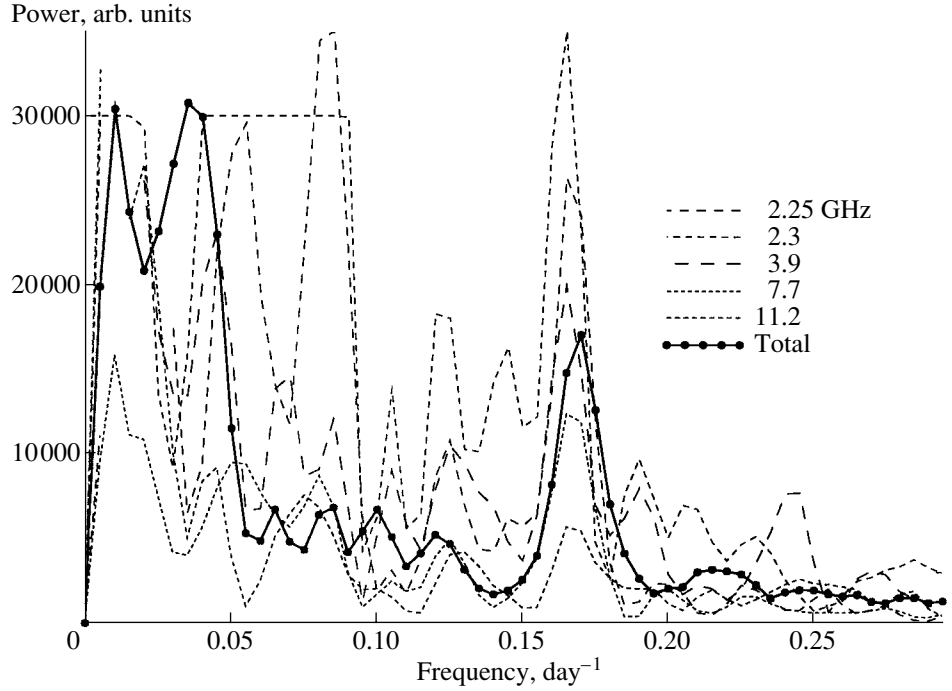

Fig. 5. Power spectrum of SS 433 for the entire cycle from May 4 to August 30, 1997 at various frequencies. The bright harmonic at 0.166 day^{-1} corresponds to the period $T = 6.05$ days.

as in 1999, the spectrum of the six-day harmonic became flatter.

We should also note here that the fluxes in the 1997 cycle were at a record low, approximately a factor of 1.5 lower than the quiescent level in the 1999 cycle. It is possible that these distinctions are important for the harmonic radio spectrum, since the lifetime (radiative timescale) of each plasmon in the

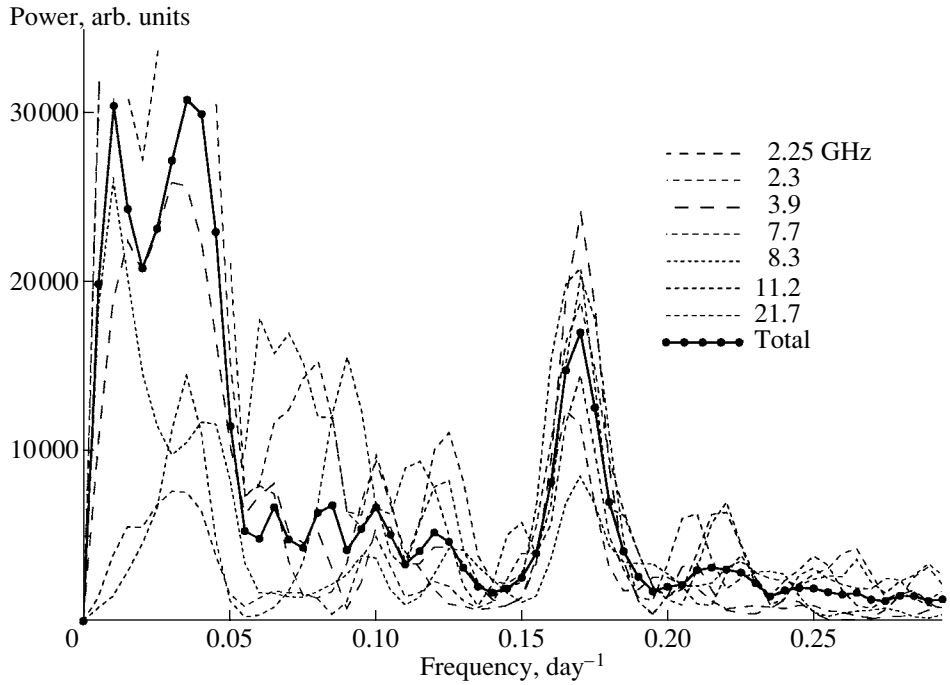

Fig. 6. Power spectrum of SS 433 for the time interval in the light curves from June 7 to August 30, 1999 at various frequencies. The average harmonic at 0.166 day^{-1} corresponds to the period $T = 6.05$ days (UT).

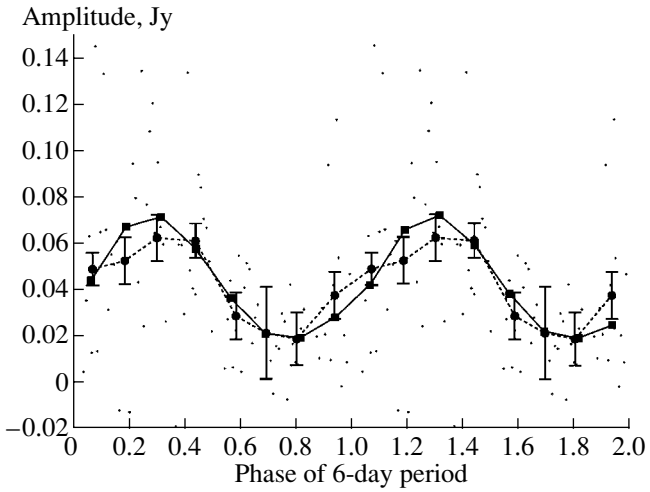

Fig. 7. Flux-density variations of SS 433 for the light curve averaged over all the frequencies in the 1999 cycle as a function of the 6-day period. Phase $\theta = 0$ corresponds to MJD 51 337.0. Robust and usual averaging over eight segments with width $\Delta\theta = 0.125$ are shown by the solid and dashed curves, respectively.

jet outflow and the plasmon birth rate can strongly affect the depth of modulation of the radio spectrum SS433.

We also applied two other methods to study the periodicity. First, analysis of the phase curves also indicates the presence of a significant six-day periodicity, with the phase run of the light curve being well determined. Figure 7 presents the phase curve of the 6.06-day period for the 1999 cycle averaged over all frequencies from 2.25 to 22 GHz. The flux densities peak at times MJD $51\,338.9 + 6.06E$. The range of the modulation is 40–50 mJy, with the average flux being about 500 mJy. The phase curve for the same period for the 1997 cycle is similar; the two light-curve amplitudes and shapes are surprisingly similar. The phase of the maxima in the first cycle is described by the formula MJD $50\,576.9 + 6.06E$. The

two ephemerides yield for the 6.06-day period a phase discrepancy of about 1.5 days for a 762-day difference in the initial times. It is clear that a small correction of the true period ($\simeq 1.5/(762/6.06) = 0.012$ days) will match the phase. Hence, the phase curve will remain virtually unchanged if we plot it with a 6.05-day period, and the phases of the times of maxima for the two cycles of observations will exactly coincide. Accordingly, the light curves of both cycles are consistent in terms of both their spectra and phases, providing important evidence for the reality and constancy of the six-day modulation.

Second, we have performed a wavelet analysis of the derived light curves. We applied Morlet wavelet functions for the dynamic analysis and again found a significant six-day harmonic. It is most conspicuous in the second part of the 1999 cycle.

3. MODEL FOR THE SIX-DAY PERIODICITY

As we have noted, the phase coincidence of the local maxima and minima, or, in other words, the good correlation between the light curves at different frequencies, suggests that the modulation is associated with a frequency-independent effect. Frequency dependence is expected in extensions of the classical models of Shklovskiĭ [32] and van der Laan [33], in which the radiation-transfer conditions change with time or synchrotron-radiation or Compton-scattering losses are important. Therefore, the most obvious way to explain the observed effect is to invoke the known geometry of the object.

Let us consider a purely geometric problem. There is a binary jet, filled with clouds of relativistic electrons with a one-day lifetime. The number of electrons does not change from day to day, nor do the conditions for absorption of emission generated in the constant magnetic field. Under these circumstances, it is clear that the flux should remain constant if the source geometry does not vary; however, for relativistic motion of material in a jet, we must take into account the fact that the frequencies of the emitted and received energy differ due to time compression in the moving coordinate frame.

The Doppler factors, namely, the ratios of the observed frequency to the emitted frequency (ν_0), for an approaching and receding clump (plasmon) are

$$\delta_{r/a} = \frac{\nu_{r/a}}{\nu_o} = \gamma^{-1}(1 \pm \beta\, cos\, \theta)^{-1},$$

where $\gamma = \left(1-\beta^2\right)^{-1/2}$ is the Lorentz factor, $\beta = v_j/c$, v_j is the jet velocity, and θ is the angle between the jet and the line of sight. We then used the formulas for the relative fluxes of two oppositely directed jet outflows.

The ratios of the observed flux density to the emitted flux density S_o for a pair of optically thin, isotropically radiating jet outflows are

$$\frac{S_a}{S_o} = \delta_a^{k-\alpha}, \quad \frac{S_r}{S_o} = \delta_r^{k-\alpha},$$

where α is the emission spectral index ($S_\nu \propto \nu^\alpha$), k is a parameter taking into account the geometry of the injected material ($k = 2$ for a continuous jet outflow, and $k = 3$ for a jet consisting of discrete plasmons). The sum of the fluxes from the two jet outflows will yield the total flux of SS 433 in its quiescent state. Substituting the ephemerides of the kinematic model and the six-day modulation of the nodding motions into this last formula, we obtain a clear periodicity in the integrated flux,

$$\beta = v_j/c(\pm \sin\theta \sin i \cos\psi \pm \cos\theta \cos i),$$
$$\Delta\beta = (\gamma - 1 - A_{58})\cos(2\pi(\mathrm{JD} - \mathrm{JD}_{58})/T_{58})$$
$$+ (\gamma - 1 - A_{63})\cos(2\pi(\mathrm{JD} - \mathrm{JD}_{63})/T_{63}),$$

where JD is the Julian day of the observations, $\psi(t) = \psi_0 + 2\pi\,(\mathrm{JD} - \mathrm{JD}_0)\,/T_p$, $\gamma = 1.035645$, $\psi_0 = 123\overset{\circ}{.}3$, $\mathrm{JD}_0 = 2\,443\,588.03$, $\theta = 19\overset{\circ}{.}8$, $i = 78\overset{\circ}{.}82$, $A_{58} = 0.00382$, $A_{63} = 0.00655$, $T_{58} = 5.838$ days, and $T_{63} = 6.29$ days.

Figure 2 shows a model light curve for such Doppler boosting with $k = 3$ and ephemerides from the work of Vermeulen [31] (we have doubled the amplitude of the nodding motions to make the modulation of the six-day time harmonic more obvious).

Our analysis shows that the relativistic modulation can explain fairly well at least the fact that the modulation depends on the phase of the precessional period. Indeed, in their spectral analysis of light curves at quiescent phases, Fiedler *et al.* [11] found no harmonic that was constant throughout all such intervals, though the 0.165-day^{-1} harmonic is clearly visible in their spectra [11, Figs. 5 and 6]. We have performed a simple analysis of the phase of the 162.5-day period and, indeed, found that the six-day modulation of the quiescent light curves is maximum precisely at epochs when the approaching jet is maximally inclined toward the observer, and nearly vanishes when the jets are in the plane of the sky.

The presence of several similar but distinct frequencies, visible in the power spectra or wavelet transform, may reflect a single modulation frequency that is Doppler compressed to different extents in different segments of the jet. It is clear that long data series cannot be used for integrated estimates, since the modulation in the spectra can disappear at some epochs. In general, the truth may be somewhere in the middle. Not only the geometry and kinematics of the source but also probable periodic processes that arise as shock waves propagate in a relativistic jet, when new portions of relativistic electrons are

produced, ensure modulation. In this case, as soon as a sinusoidal modulation in the flux of material is imparted to the jet, the conditions in the shock wave change, resulting in a modulation of the quiescent radio flux.

4. CONCLUSIONS

Based on observational data covering about 250 days, we have for the first time unambiguously established the existence of a six-day periodicity at a level of about 10–15% in the quiescent radio flux of SS 433, whose spectrum is $S_\nu = 1.2\nu^{-0.6}$, where S_ν is in Jy and ν is in GHz. This periodicity is clearly visible both in power spectra in two independently reduced observational cycles separated by 750 days and in phase curves derived using the period found. In both cases, the shape of the phase curves is retained in both the phase and amplitude of the modulation.

This modulation is undoubtedly related to the interaction between the 13.1-day orbital and 162.5-day precessional periods of the SS 433 system, when the nutation motions result in appreciable nodding of the jets. The discovered effect is reminiscent of modulation recently discovered in the radio emission of Cyg X-1 [34, 35]. Another case of orbital modulation has been known for a long time, for the binary system LSI +61°303 [36], though, in this case, the periodicity in the radio flux is explained by the large eccentricity of the orbit.

As a first step, we have proposed an explanation of such frequency-independent modulation in SS 433 based on Doppler boosting of the jet flux, due to the six-day periodicity of the jet nodding during the basic precessional rotation. In this case, the quiescent flux is the sum of the fluxes from individual short-lived segments of the jet. The entire 1999 cycle falls precisely at the ephemeris expected to maximize this effect.

The jet filling factor and lifetime of each individual clump can change the modulation pattern appreciably, blurring or enhancing it in different time intervals [8]. In intervals when the jets are in the plane of the sky ($\theta = 90°$), the effect vanishes, while at epochs of the greatest inclination of the jets to the line of sight the effect becomes maximum. It would be interesting to search for such modulation in the radio emission of other sources with relativistic jet outflows [37]. Similar modulation has already been detected in quasars and AGN [38, 39]. In this way, we can explain the transient character of the six-day harmonic in the power spectra for different quiescent segments of light curves measured on the Green Bank interferometer [11].

ACKNOWLEDGMENTS

The project to monitor X-ray binary systems was supported by the Russian Foundation for Basic Research (project code 98-02-17577). The authors are grateful to the staff of the NRAO (Green Bank, USA) for providing the series of observations of SS 433, to our colleagues P.G. Tsybulev and O.V. Verkhodanov for the spectral estimation software, and to the Head of the Continuum Radiometers Laboratory N.N. Nizhel'skiĭ and the RATAN-600 staff for their role in helping insure excellent performance of the radio telescope.

REFERENCES

1. C. B. Stephenson and N. Sanduleak, Astrophys. J., Suppl. Ser. **33**, 459 (1977).
2. D. H. Clark and P. Murdin, Nature **276**, 44 (1978).
3. R. M. Hjellming and K. J. Johnson, Astrophys. J. **328**, 600 (1988).
4. B. Margon, Annu. Rev. Astron. Astrophys. **22**, 507 (1984).
5. Yu. N. Pariĭskiĭ and D. V. Korol'kov, Itogi Nauki Tekh., Ser. Astron. **31**, 73 (1983).
6. R. C. Vermeulen, V. Icke, R. T. Schilizzi, *et al.,* Nature **328**, 309 (1987).
7. R. C. Vermeulen, R. T. Schillizzi, R. E. Spencer, *et al.,* Astron. Astrophys. **270**, 170 (1993).
8. R. E. Spencer, Mon. Not. R. Astron. Soc. **209**, 869 (1984).
9. S. I. Neizvestnyĭ, S. A. Pustil'nik, and V. G. Efremov, Pis'ma Astron. Zh. **6**, 700 (1980) [Sov. Astron. Lett. **6**, 368 (1980)].
10. K. J. Johnston, B. J. Geldzahler, J. H. Spencer, *et al.,* Astron. J. **89**, 509 (1984).
11. R. L. Fiedler, K. J. Johnston, J. H. Spencer, *et al.,* Astron. J. **94**, 1244 (1987).
12. R. C. Vermeulen, W. B. McAdam, S. A. Trushkin, *et al.,* Astron. Astrophys. **279**, 189 (1993).
13. N. N. Bursov and S. A. Trushkin, Pis'ma Astron. Zh. **21**, 163 (1995) [Astron. Lett. **21**, 145 (1995)].
14. S. A. Trushkin and N. N. Bursov, Astrophys. Lett. Commun. (2001) (in press).
15. S. A. Trushkin, E. K. Majorova, and N. N. Bursov, Astrophys. Space Sci. (2001) (in press).
16. R. P. Fender, S. J. B. Burnell, and E. B. Waltman, Vistas Astron. **41**, 3 (1997).
17. I. F. Mirabel and L. F. Rodríguez, Ann. Rev. Astron. Astrophys. **37**, 409 (1999); astro-ph/9902062.
18. J. W. M. Baars, R. Genzel, I. I. K. Pauliny-Toth, and A. Witzel, Astron. Astrophys. **61**, 99 (1977).
19. M. Ott, A. Witzel, A. Quirrenbach, *et al.,* Astron. Astrophys. **284**, 331 (1994).
20. W. H. Press, S. A. Teukolsky, W. T. Vetterling, and B. P. Flannery, *Numerical Recipes*, in *The Art of Scientific Computing* (Cambridge Univ. Press, Cambridge, 1992).
21. V. P. Goranskiĭ, V. F. Esipov, and A. M. Cherepashchuk, Astron. Zh. **75**, 240 (1998) [Astron. Rep. **42**, 209 (1998)].

22. V. P. Goranskiĭ, V. F. Esipov, and A. M. Cherepashchuk, Astron. Zh. **75**, 383 (1998) [Astron. Rep. **42**, 336 (1998)].
23. G. O. Abell and B. Margon, Nature **279**, 701 (1979).
24. F. Ciatti, T. Iijima, A. Mammano, and A. Vittone, Astron. Astrophys., Suppl. Ser. **52**, 443 (1983).
25. A. Mammano, R. Margoni, F. Ciatti, and S. Christiani, Astron. Astrophys. **119**, 153 (1983).
26. J. I. Katz, S. F. Anderson, B. Margon, and S. Grandi, Astrophys. J. **260**, 780 (1982).
27. G. H. Newsom and G. W. Collins, II, Astron. J. **86**, 1250 (1981).
28. G. H. Newsom and G. W. Collins, II, Astrophys. J. **262**, 714 (1982).
29. G. W. Collins, II, G. H. Newsom, and R. N. Boyd, Astrophys. J., Suppl. Ser. **76**, 417 (1981).
30. J. J. Matise and D. P. Whitemire, Astron. Astrophys. **106**, L9 (1982).
31. R. C. Vermeulen, Ph.D. Thesis (Univ. of Leiden the Netherlands, 1989), p. 1.
32. I. S. Shklovskiĭ, Astron. Zh. **37**, 222 (1960) [Sov. Astron. **4**, 243 (1960)].
33. H. van der Laan, Nature **211**, 1131 (1966).
34. G. G. Pooley, R. P. Fender, and C. Brocksopp, Mon. Not. R. Astron. Soc. **302**, L1 (1999).
35. L. Wen, W. Cui, A. M. Levine, and H. V. Bradt, Astrophys. J. **525**, 968 (1999).
36. A. R. Taylor and P. C. Gregory, Astrophys. J. **255**, 210 (1982).
37. S. A. Trushkin, Astron. Astrophys. Trans. **19**, 524 (2000).
38. J. I. Katz, Astrophys. J. **478**, 527 (1997).
39. P. A. Hughes, H. D. Aller, and M. F. Aller, Astrophys. J. **503**, 662 (1998).

Translated by G. Rudnitskiĭ

Astronomy Reports, Vol. 45, No. 10, 2001, pp. 816–823. Translated from Astronomicheskiĭ Zhurnal, Vol. 78, No. 10, 2001, pp. 934–941.

Generation of Large-Scale Magnetic Fields in Young Solar-Type Stars

L. L. Kitchatinov

Institute of Solar–Terrestrial Physics, Siberian Division, Russian Academy of Sciences, P.O. Box 4026, Irkutsk, 664033 Russia

Received December 19, 2000

Abstract—Differential-rotation and dynamo models are computed for a young, solar-mass star at the initial stage of the formation of its radiative core. It is argued that the global magnetic fields in the radiative zones of the contemporary Sun and similar stars are due to the action of a hydromagnetic dynamo at early evolutionary stages. Our computations suggest that this field should be nonaxisymmetric. Physical reasons for departures from axial symmetry are discussed in detail. It is suggested that nonaxisymmetric relic fields are responsible for the phenomenon of active longitudes. © *2001 MAIK "Nauka/Interperiodica".*

1. INTRODUCTION

We discuss here a dynamo model for a very young star that has not yet reached the main sequence. Specifically, we are interested in the state of the star upon completion of the time when it is fully convective, at the very beginning of the formation of its radiative zone. For a solar-mass star, this corresponds to an age of about 2 Myr [1]. Our interest in the global magnetic field at this age is mainly in connection with the following two circumstances.

First, in all likelihood, the so-called relic magnetic field of the contemporary Sun formed at that time. Helioseismology has shown that the deep solar interior rotates at nearly the same rate as the surface [2]. Young stars are known to rotate much faster than the Sun. As a star becomes older, its rotation decelerates due to angular-momentum losses via the stellar wind [3]. Clearly, in order for the interior and surface angular velocities to be equal, the central region must be coupled quite efficiently with the convective envelope, whose rotation becomes slower. The microscopic viscosity is very small in the radiative zone ($\sim 10^3$ cm^2/s) and cannot act as a coupling agent. Only the presence of an interior magnetic field in the radiative zone could provide the required coupling [4–6]. It is believed that this is a relic field; i.e, it has been preserved since the early evolution of the star. This is quite plausible, since the time scale for ohmic dissipation of global fields in the radiative zone is several billion years [7]. Nevertheless, the origin of the field in the radiative zone poses a problem. A forming star can capture an appreciable magnetic flux from its protostellar cloud [8]. Later, however, the star remains fully convective for several million years, which is about a factor of 10^4 longer than the eddy-diffusion time. It is clear that all traces of the primary field are absent by the beginning of the formation of the radiative zone. In a rotating, fully convective star, a hydromagnetic dynamo can operate [9, 10], as is confirmed by the observed magnetic activity of early stars [11, 12]. The growing radiative core will capture dynamo field from the convection zone [13, 14]. The capture is most efficient at the early stages of formation of the core, when it grows most rapidly [10]. Therefore, the geometry and amplitude of the relic field are controlled by the hydromagnetic dynamo when the growth of the radiative core begins.

Second, magnetic fields affect the accretion of material from protoplanetary disks. At distances out to the corotation radius, the material flows along magnetic field lines. Magnetic forces impart angular momentum to the disk, thereby controlling the rotation of the star (see, e.g., [15–17]). Disks surround 30 to 50% of stars with ages up to 3 Myr and masses close to a solar mass [18]. By an age of 10 Myr, indicators of the presence of disks are no longer observed [18, 19]. The formation of the radiative zone and the star–disk interaction coincide in time. When this interaction is considered, it is usually assumed that the magnetic field is symmetric about the rotational axis. Dynamo models [9, 10], however, predict asymmetric global fields for very young stars.

The differential-rotation and dynamo models considered here for a solar-mass star also imply nonaxisymmetric fields. We will discuss in detail physical reasons for deviations from axial symmetry. We will also attempt to explain the phenomenon of active longitudes observed on the Sun (see, e.g., [20–22]) and stars [23, 24] invoking a nonaxisymmetric relic field in the radiative zone.

1063-7729/01/4510-0816$21.00

Parameters of the newly born Sun at the onset of the formation of the radiative zone.

Age, Myr	$M/M_\odot$	$L/L_\odot$	$R/R_\odot$	x_i	ρ_e, g/cm^3	T_e, K
1.92	1	1.14	2.01	0.05	6.4×10^{-3}	1.25×10^5

2. MODELS

Differential rotation. To solve the dynamo problem, we must know the rotational state of the star. We used the differential-rotation model proposed by Kitchatinov and Rüdiger and described in detail in [25]. This model describes the distributions of differential rotation, meridional flow, and specific entropy within the convective envelope for given values of the source parameters—the mass M, luminosity L, stellar radius R, rotational period $P_{\rm rot}$, relative radius of the base of the convection zone $x_{\rm i} = r_{\rm i}/R$, ratio of the mixing length to the pressure scale height $\alpha_{\rm MLT} = \ell/H_{\rm p}$, and also the density $\rho_{\rm e}$ and temperature $T_{\rm e}$ at the outer boundary $x_{\rm e}$ of the computation domain. We used the quite conventional value $\alpha_{\rm MLT} = 1.7$ and assumed $x_{\rm e} = 0.95$. Thus, we excluded the thin, highly nonuniform surface layer from our consideration.

The other structural parameters of the star were found using the evolutionary model of Eggleton [26, 27] by computing the evolution of a solar-mass star with a chemical composition typical of Population I: $X = 0.70$, $Z = 0.02$. The initial state corresponded to a fully convective protostar at the beginning of the Hayashi stage, with a radius of $6R_\odot$. The computations were continued until an age of 1.92 Myr, the onset of the formation of the radiative zone. The source parameters thus obtained (A. Collier Cameron, private communication) are given in the table.

The rotational velocities of young T Tau stars are typically about 20 km/s [18, 28]. Model calculations for velocities ranging from 10 to 25 km/s gave very similar results.

Figure 1 shows the differential rotation for $P_{\rm rot} = 5$ days. The variation of the angular velocity at the surface is as small as $\simeq 0.2\%$. Such weak rotational nonuniformities are typical of cases when the Coriolis number

$$\Omega^* = 2\tau\Omega \qquad (1)$$

is large (τ is the convection-cell turnover time) [25, 29]; this seems to agree with observations [30–32]. We will see that, nevertheless, weakly differential rotation markedly affects the magnetic fields.

Dynamo. The large-scale magnetic field $\mathbf{B}$ obeys the mean-field induction equation (see, e.g., [33]):

$$\partial\mathbf{B}/\partial t = \mathrm{curl}\,(\mathbf{V}\times\mathbf{B} + \boldsymbol{\epsilon}), \qquad (2)$$

where the first and second terms on the right-hand side take into account large-scale and small-scale hydrodynamic flows, respectively. The velocity $\mathbf{V}$ corresponds to nonuniform rotation:

$$\mathbf{V} = \mathbf{e}_\phi r\,\sin\theta\,\Omega(r,\theta). \qquad (3)$$

Here, r, θ, ϕ are the usual spherical coordinates and $\mathbf{e}_\phi$ is a unit vector in the azimuthal direction. The mean EMF $\boldsymbol{\epsilon}$ in (2) results from correlated fluctuations in the magnetic field, $\mathbf{B}'$, and velocity, $\mathbf{u}'$:

$$\boldsymbol{\epsilon} = \overline{\mathbf{u}'\times\mathbf{B}'} = \boldsymbol{\epsilon}_{\rm diff} + \boldsymbol{\epsilon}_{\rm gen}, \qquad (4)$$

where the two terms on the right-hand side describe the contributions of eddy diffusion and the so-called alpha effect—the generation of magnetic fields by small-scale cyclonic motions [34].

Eddy diffusion in a rotating medium is anisotropic [35]:

$$\boldsymbol{\epsilon}_{\rm diff} = -\eta\,\mathrm{curl}\,\mathbf{B} - \eta_\parallel \mathbf{e}\times((\mathbf{e}\times\nabla)\,\mathbf{B}), \qquad (5)$$

where $\eta_\parallel$ is the excess diffusivity along the rotational axis over the diffusivity in directions normal to this axis, and $\mathbf{e} = \boldsymbol{\Omega}/\Omega$ is a unit vector along the rotational axis. The eddy diffusivities

$$\eta = \eta_T\phi(\Omega^*), \quad \eta_\parallel = \eta_T\phi_\parallel(\Omega^*) \qquad (6)$$

depend on the angular velocity through the so-called quenching functions $\phi(\Omega^*)$ and $\phi_\parallel(\Omega^*)$ of the Coriolis number (1) [35]:

$$\phi(\Omega^*) = \frac{3}{4\Omega^{*2}}\left(1 + \frac{\Omega^{*2}-1}{\Omega^*}\mathrm{arctan}\Omega^*\right), \qquad (7)$$

$$\phi_\parallel(\Omega^*) = \frac{3}{4\Omega^{*2}}\left(-3 + \frac{\Omega^{*2}+3}{\Omega^*}\mathrm{arctan}\Omega^*\right).$$

The quantity η_T in (6) is the eddy diffusivity for a nonrotating medium.

The part of the mean EMF (4) that is responsible for magnetic-field generation is determined by the tensor $\boldsymbol{\alpha}$:

$$\boldsymbol{\epsilon}_{\rm gen} = \boldsymbol{\alpha}\circ\mathbf{B}. \qquad (8)$$

We will use the representation of $\boldsymbol{\alpha}$ obtained in [36] for a density-stratified rotating fluid

$$\alpha_{ij} = -\eta_T(\mathbf{e}\times\mathbf{G})(\delta_{ij}\mathcal{A}_1(\Omega^*) + e_ie_j\mathcal{A}_4(\Omega^*)) - \eta_T(e_iG_j + e_jG_i)\mathcal{A}_2(\Omega^*). \qquad (9)$$

Here, $\mathbf{G} = \nabla\ln(\rho)$ is the relative density gradient and the functions $\mathcal{A}_n$ of the Coriolis number (1) read

$$\mathcal{A}_1(\Omega^*) = \frac{3}{2\Omega^{*3}} \times\left(\Omega^{*2} + 6 - \frac{6+3\Omega^{*2}-\Omega^{*4}}{\Omega^*}\mathrm{arctan}\Omega^*\right), \qquad (10)$$

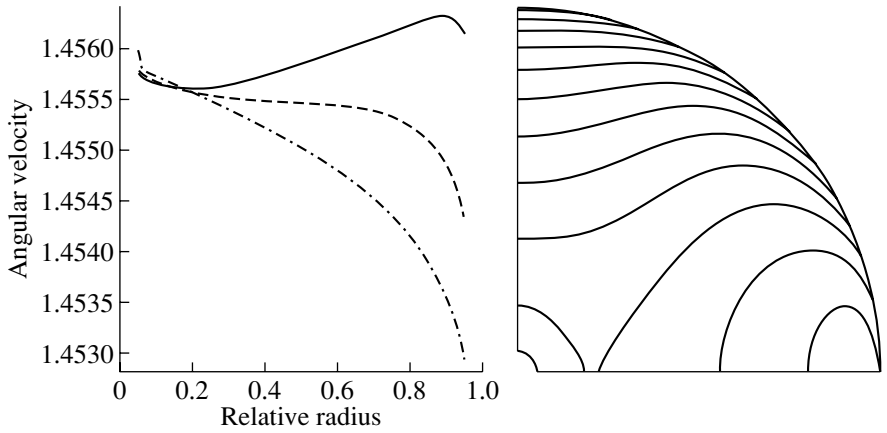

Fig. 1. Rotation law for a $1M\odot$ star with an age of 1.92 Myr predicted by our model. Left: radial dependences of the angular velocity for the equator (solid curve), latitude 45° (dashed curve), and the polar zone (dot-dashed curve); right: contours of equal velocity; $P_{\rm rot}$=5 days.

$$\mathcal{A}_2(\Omega^*) = -\frac{4}{\Omega^*}\phi_{\|}(\Omega^*),$$

$$\mathcal{A}_3(\Omega^*) = \frac{3}{2\Omega^{*3}}$$

$$\times\left(\Omega^{*2}-30-\frac{2\Omega^{*4}}{1+\Omega^{*2}}+\frac{30+9\Omega^{*2}-\Omega^{*4}}{\Omega^*}\arctan\Omega^*\right),$$

where $\phi_{\|}(\Omega^*)$ is defined by (8).

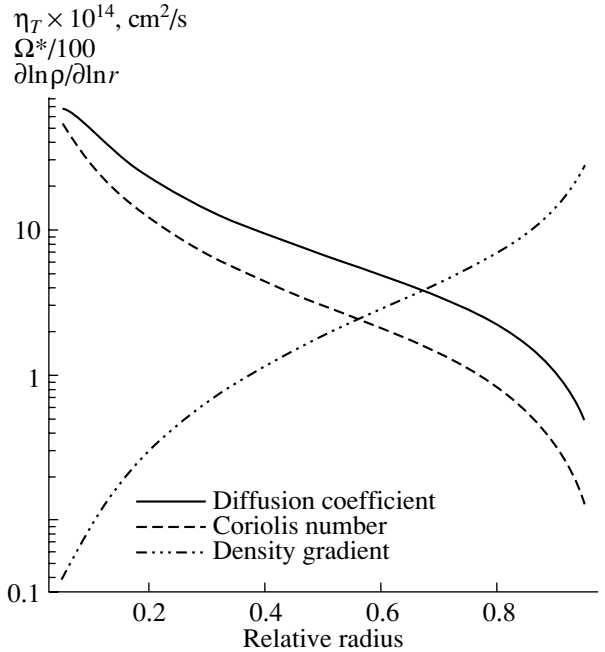

Fig. 2. The diffusion coefficient η_T (11) in units of 10^{14} cm^2/s, Coriolis number (1) divided by 100 ($\Omega^*/100$), and relative density gradient $-rG=-\partial\ln\rho/\partial\ln r$ as functions of radius, according to the differential-rotation model for $P_{\rm rot}=5$ days.

The diffusion coefficient for a nonrotating medium can be estimated from the well-known relationship of mixing-length theory

$$\eta_T = -\frac{\tau\ell^2 g}{12c_{\rm p}}\frac{\partial S}{\partial r}. \qquad (11)$$

Here, S is the specific entropy supplied by the model for the differential rotation. This model also provides the distributions of the Coriolis number (1) and density gradient, shown in Fig. 2. Thus, the available information is sufficient to solve the dynamo problem.

We ignore here the feedback of the magnetic field on the fluid motion, and solve a linear, although generally three-dimensional (nonaxisymmetric), dynamo problem. In this problem, field components having different types of symmetry about the equatorial plane and rotational axis do not affect one another and can be treated independently. We will use the conventional (see, e.g., [37]) notation Sm and Am for the types of symmetry: S and A correspond to fields symmetric and antisymmetric in terms of mirror reflection about the equatorial plane, and m is the azimuthal wave number. Thus, for nonaxisymmetric fields, $m\neq0$, while $m=0$ for an axisymmetric field. The simplest field patterns of different symmetry types are shown in Fig. 3.

The dimensionless dynamo equations contain the two control parameters

$$C_\Omega = \frac{\Delta\Omega R^2}{\eta},\quad C_\alpha = \frac{\alpha_{\phi\phi}R}{\eta}, \qquad (12)$$

where $\Delta\Omega$ is the angular-velocity difference between the equator and poles; the component $\alpha_{\phi\phi}$ of the tensor (9) and the diffusion coefficient η are taken for the middle of the convective envelope, a distance

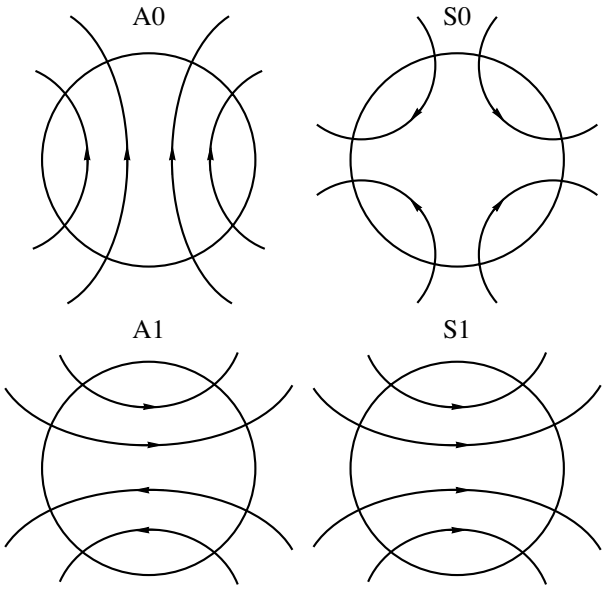

Fig. 3. Magnetic fields with different types of symmetry about the equator and rotational axis.

$r = (r_\mathrm{i} + r_\mathrm{e})/2$ from the center. The quantity C_Ω is determined by the rotational state of the star, and C_α is the only free parameter of our model. Recall that magnetic fields are generated if the dynamo number C_α (12) exceeds some critical value. For smaller C_α, the field decays with time. The threshold value of C_α depends on the symmetry of the field. We will compute the threshold values of the dynamo number for different types of symmetry for the following reason. In the nonlinear regime, the alpha effect is quenched by the feedback of the magnetic field on the motions generating this field. This reduces the effective value of C_α to the threshold value, and the nonlinear solution is usually close to that symmetry for which the threshold dynamo number is minimum in the linear theory [38, 39]. In other words, the solution to the linear problem that corresponds to the lowest threshold value of C_α represents the fundamental, or preferably generated, mode of the magnetic field.

We specified superconducting interfacial and vacuum boundary conditions at the base and surface of the convective envelope, respectively. The strong magnetic fields of young, rapidly rotating stars can be assumed to easily escape through the stellar surface via the Parker instability [40], so that open vacuum boundary conditions can be used. We solved the eigenvalue problem for the dynamo equations using the inverse-iteration method.

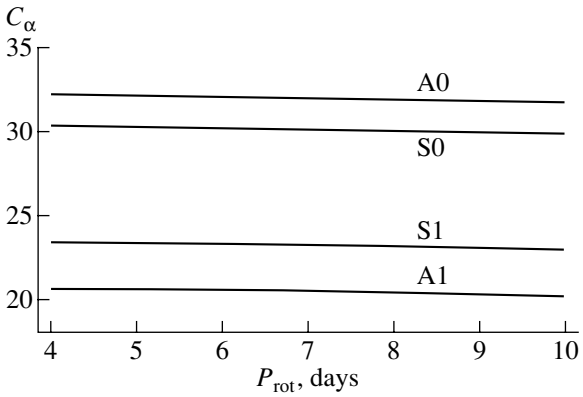

Fig. 4. Critical values of the dynamo number C_α for the generation of fields with various types of global symmetry as functions of the rotational period.

3. RESULTS AND DISCUSSION

Fundamental mode. The rotational periods typical of T Tau stars are about one week. We carried out computations for periods ranging from four to ten days. The threshold dynamo numbers C_α for magnetic fields with various types of global symmetry are given in Fig. 4. We can see that these numbers depend on weakly only the rotational velocity.

The lowest excitation threshold corresponds to the nonaxisymmetric mode A1. The amplitude of the field can be estimated by assuming that the magnetic-energy density coincides with the kinetic energy of the convective flows generating the magnetic field to order of magnitude. This yields a field strength of 2–3 kG.

As usual, the nonaxisymmetric global field is stationary in a certain rotating frame of reference, which generally differs from a frame corotating with the fluid. The field distribution does not vary in amplitude, but undergoes an azimuthal drift, making a complete revolution in approximately the diffusion time (~ 100 yr) in the corotating reference frame.

Visual representation of three-dimensional fields encounters difficulties. Some impression of the flow structure can be gained using the Chandrasekhar decomposition [41] of the magnetic field in a spherical geometry into toroidal and poloidal components:

$$\mathbf{B} = \mathbf{B}_\mathrm{t} + \mathbf{B}_\mathrm{p} \qquad (13)$$
$$= \mathbf{r} \times \nabla T + \mathrm{curl}\,(\mathbf{r} \times \nabla P)\,.$$

Any toroidal field line lies on a spherical surface with some radius r. The poloidal field is maintained by toroidal currents. Figure 5 illustrates toroidal field lines on the surface $r \simeq 0.7R$ and contours of the radial component of the poloidal field on the same surface for the fundamental nonaxisymmetric mode.

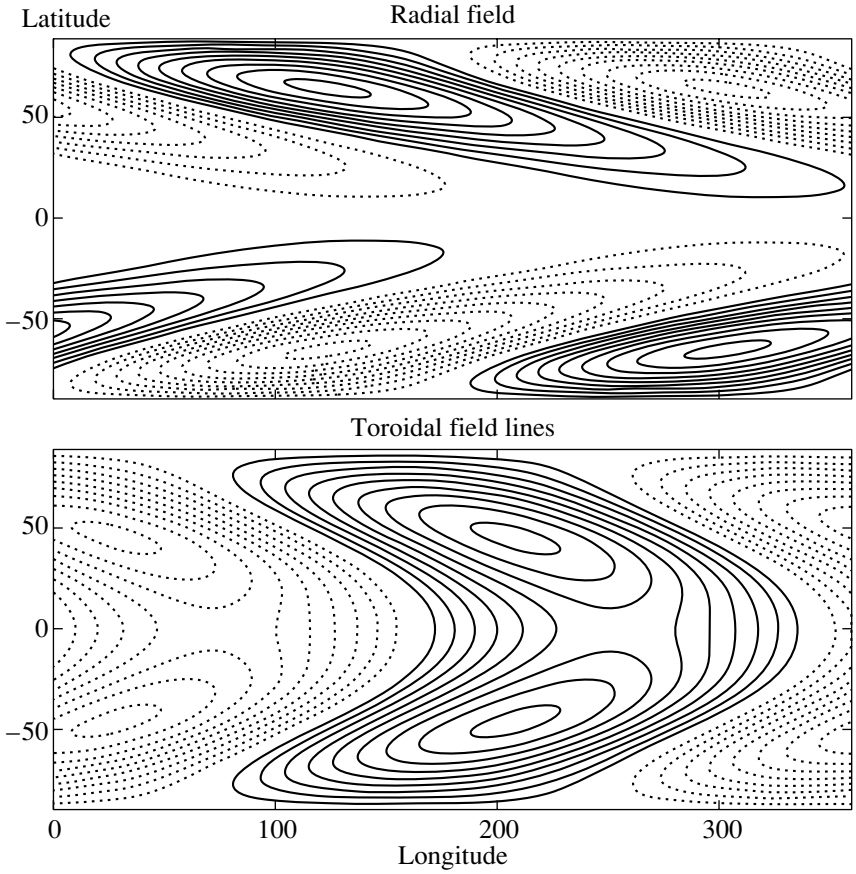

Fig. 5. Contours of the radial component of the field (top) and toroidal field lines (bottom) on the spherical surface $r \simeq 0.7R$ for the neutrally stable mode A1; $P_{\rm rot} = 5$ days. Solid (dotted) contours correspond to positive (negative) values for the radial field and clockwise (counterclockwise) circulation for the toroidal field.

Küker and Rüdiger [9] also found that a nonaxisymmetric global field can be generated in a fully convective star with mass $1.5M_\odot$. However, this field was of S1 symmetry type. This does not contradict our results. If differential rotation is neglected, as in [9], our model also predicts S1 symmetry. We can see from Fig. 4 that the threshold dynamo numbers for S1 and A1 are similar. Which is smaller depends on the details of the model, in particular, on the rotation law. The type of equatorial symmetry of the field can hardly be predicted based on dynamo models. The mode S1 field is shown in Fig. 6.

The situation is different for the case of axial symmetry. The threshold dynamo numbers presented in Fig. 4 for axisymmetric modes are much higher than those for nonaxisymmetric ones. The dynamo solutions suggest that nonaxisymmetric global fields are generated at the onset of the formation of the radiative zone in stars with masses close to a solar mass. This is important for all further analyses, and it is appropriate to elucidate physical reasons for deviations from axial symmetry.

Why are nonaxisymmetric fields generated? There are two main reasons: (i) slight nonuniformity of the rotation and (ii) anisotropy of the convective mixing for high Coriolis numbers (1).

Differential rotation is known to be involved in the generation of axisymmetric fields, stretching the toroidal field from the poloidal field. However, even in the axisymmetric case, differential rotation is not necessary for the operation of a dynamo, although it enhances the dynamo effect. The generation of a (global) field can be provided only by small-scale convective motions. This mechanism is referred to as the α^2 dynamo [33]. For nonaxisymmetric fields, differential rotation hinders the dynamo. Strong nonuniformity of the rotation rapidly transforms the azimuthal nonuniformity of the field into small-scale radial and latitudinal inhomogeneities [37], increasing diffusive losses. Such twisting of the nonaxisymmetric field can be seen in Figs. 5 and 6, although the rotation is weakly differential (see Fig. 1).

The efficiency of differential rotation is characterized by the quantity C_Ω (12). For $P_{\rm rot} = 5$ days, $C_\Omega = 240$, approximately a factor of five smaller than for the

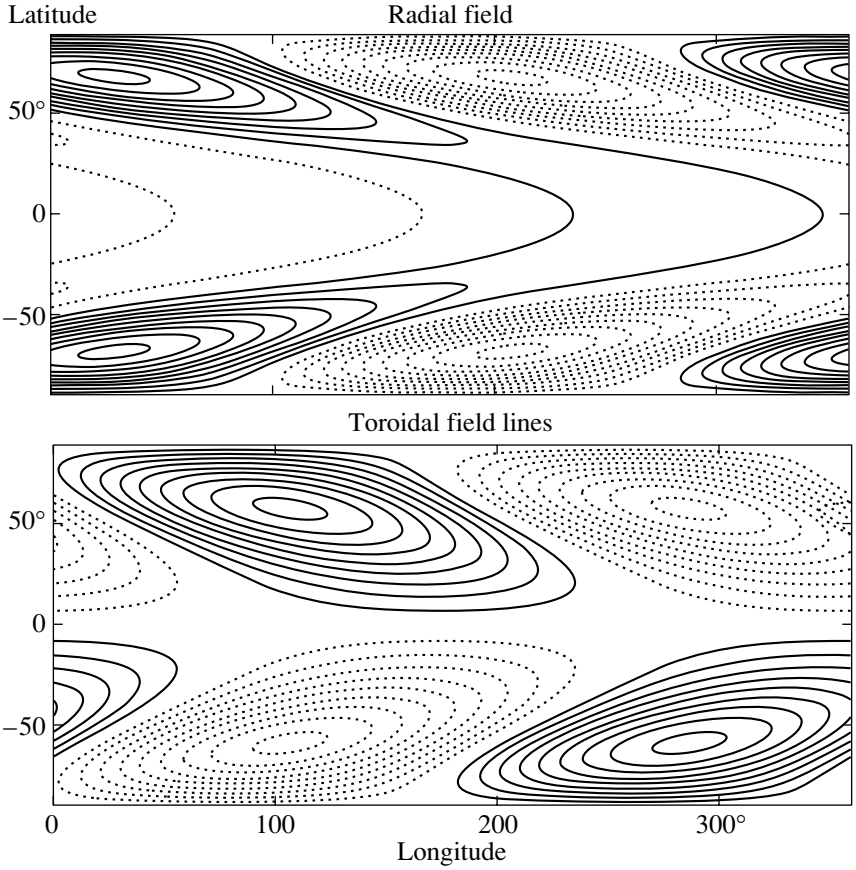

Fig. 6. Same as Fig. 5 for mode S1.

contemporary Sun. Note that these C_Ω values were based on the differential rotation at the surface, where $\Delta\Omega$ is maximum (Fig. 1). However, our model may underestimate the differential rotation compared with the rate indicated by observations (by about a factor of two in the case of the extremely fast rotation of AB Dor [25, 30]). For this reason, we repeated some calculations with the differential rotation increased by a factor of three. Nonaxisymmetric magnetic fields still dominated. Slight rotational nonuniformity offers possibilities for the generation of nonaxisymmetric fields.

The excitation of precisely such fields is preferred because of the anisotropy of the convection. We can see from Fig. 2 that the Coriolis numbers are large in the case under study. The tensor $\boldsymbol{\alpha}$ (9) for $\Omega^* \gg 1$ is anisotropic:

$$\alpha_{ij} = \frac{3}{4}\pi\eta_T G\,(\delta_{ij} - e_i e_j)\,\cos\theta. \qquad (14)$$

Here, formulas (10) are taken into account, retaining lowest order terms in Ω^{*-1}. In view of (8), we can see from (14) that there is no α effect for the field parallel to the rotational axis. This is a direct consequence of the well-known tendency of convective flows to approach a two-dimensional state in the presence of rapid rotation, $\Omega^* \gg 1$. In this case, the flow is almost uniform in the direction of the rotational axis; i.e., convective cells form rolls stretched along this axis. It is obvious that if the magnetic field is also parallel to the rotational axis the two-dimensional flow can only rearrange field lines, not deform them. Deformation of field lines is necessary for the α effect [34, 40], which is, therefore, absent in the case of $\mathbf{B} \parallel \boldsymbol{\Omega}$. However, a finite α effect is present for fields inclined to the rotational axis, which reaches a maximum for fields normal to this axis. Note also that the tensor (14) depends on the latitude as $\cos\theta$; therefore, the α effect is maximum at the poles.

Thus, the α effect for the generation of magnetic field via convective motions is also maximum at the rotational axis for fields normal to this axis. Only nonaxisymmetric fields with $m = 1$ have a component normal to the rotational axis at this axis (see Fig. 3). In other words, only nonaxisymmetric fields can make use of the α effect in the region where it is maximum. This is why the generation of such fields is preferred.

To verify these qualitative considerations, we carried out computations for an isotropic α effect [with

$\mathcal{A}_2$ and $\mathcal{A}_4$ set equal to zero in (9)]. In this case, axisymmetric fields become dominant.

Active longitudes. As already noted, the developing radiative zone captures the dynamo field most efficiently in the initial stages of its growth; i.e., at the time to which our model computations refer. Therefore, the interior fossil field of the radiative zone will not be axisymmetric. Estimation of its amplitude requires nonlinear computations. A very simple nonlinear model yielded values $\lesssim 1$ G [10]. This relatively small amplitude can be explained by variability of the dynamo field in time, due to the azimuthal drift. Although such a field is smaller than the global poloidal field of the Sun (1–2 G), it can have observable manifestations.

The relic field frozen in the rigidly rotating radiative zone can penetrate into the convective envelope, where differential rotation will generate an azimuthal field from it. The azimuthal field will likewise not be axisymmetric. In the longitude range where its direction coincides with that of the toroidal dynamo field, magnetic activity will be enhanced. This effect may give rise to active solar longitudes.

The solar dynamo field is close to symmetry type A0 [42]. As noted above, dynamo models do not enable clear-cut discrimination between symmetries S1 and A1 for the relic field (Fig. 3). We can easily imagine that if the relic field has A1 symmetry only one active longitude will dominate and be equally pronounced in the northern and southern hemispheres; in the case of an S1 field, two regions of enhanced activity separated by 180° in longitude and antisymmetric about the equator will appear. There is evidence that the situation for solar active longitudes is close to this latter one [21, 43–45]. In this case, the relic field resembles a dipole field with its axis in the equatorial plane (symmetry type S1).

Note that departure of the dipole-field axis from the equatorial plane, which is quite possible, will result in an alternation of activity cycles with relatively high and low amplitudes [46].

Active longitudes are also observed on stars. In some cases, the so-called flip-flop phenomenon has been detected [23, 24]. Solar-type activity cycles are present. During a given half-cycle, one active longitude is dominant; in the next half-cycle, the active longitude changes position by 180°, returning to the initial position after completion of the cycle. This pattern can be interpreted as a combination of either a relic S1 field with an oscillatory S0 dynamo field or a relic A1 field with an oscillatory A0 field.

For what other reasons may departures from axial symmetry be important? The interior field of the radiative zone causes it to rotate rigidly, which proves to be important in the context of stellar angular-momentum losses [5, 6] and for the structure of the so-called tachocline—a thin layer under the convection zone where a transition from differential to rigid rotation takes place [7, 47]. As noted in the Introduction, the global magnetic fields of young stars largely determine the interaction of these stars with their protoplanetary disks [15–17]. In all these applications, axial symmetry of the field was invariably assumed. However, in at least one case, the tachocline problem, taking into account departures from axial symmetry may be important. For a symmetric field, the motion of the material is purely rotational, and the angular momentum is redistributed in latitude exclusively via magnetic stresses. The interaction of the rotation with a nonaxisymmetric field will produce global nonaxisymmetric flows (vortices). In this case, Reynolds stresses contribute to the angular-momentum transfer, which qualitatively changes the situation. Note that the possible existence of global vortices below the convection zone has also not been taken into account in helioseismological reconstructions of the interior rotation of the Sun.

ACKNOWLEDGMENTS

I am grateful to A. Collier Cameron, St. Andrews, for the availability of his computations of the interior structure of stars. This work was supported by the Russian Foundation for Basic Research (project no. 99-02-16088).

REFERENCES

1. R. Kippenhahn and A. Weigert, *Stellar Structure and Evolution* (Springer-Verlag, Berlin, 1994).
2. J. Schou, H. M. Antia, S. Basu, *et al.,* Astrophys. J. **509**, 456 (1998).
3. A. Skumanich, Astrophys. J. **171**, 565 (1972).
4. H. Spruit, in *The Internal Solar Angular Velocity,* Ed. by B. Durney and S. Sofia (D. Reidel, Dordrecht, 1987), p. 185.
5. P. Charbonneau and K. B. McGregor, Astrophys. J. **343**, 526 (1992).
6. P. Charbonneau and K. B. McGregor, Astrophys. J. **417**, 762 (1993).
7. L. L. Kichatinov and G. Rüdiger, Pis'ma Astron. Zh. **22**, 312 (1996) [Astron. Lett. **22**, 279 (1996)].
8. L. Mestel, Q. J. R. Astron. Soc. **6**, 265 (1965).
9. M. Küker and G. Rüdiger, Astron. Astrophys. **346**, 922 (1999).
10. L. L. Kitchatinov, M. Jardine, and A. C. Cameron, Astron. Astrophys. (2001) (in press).
11. R. L. Gilliland, Astrophys. J. **300**, 339 (1986).
12. G. Basri, G. W. Marcy, and J. A. Valenti, Astrophys. J. **390**, 622 (1992).
13. E. N. Parker, Geophys. Astrophys. Fluid Dyn. **18**, 175 (1981).

14. A. E. Dudorov, V. N. Krivodubskiĭ, T. V. Ruzmaĭkina, and A. A. Ruzmaĭkin, Astron. Zh. **66**, 809 (1989) [Sov. Astron. **33**, 420 (1989)].
15. M. Camenzind, in *Reviews in Modern Astronomy 3,* Ed. by G. Klare (Springer-Verlag, Berlin, 1990), p. 234.
16. J. Bouvier, S. Cabrit, M. Fernandes, *et al.,* Astron. Astrophys. **272**, 176 (1993).
17. A. C. Cameron and C. G. Campbell, Astron. Astrophys. **274**, 309 (1993).
18. B. Bodenheimer, Annu. Rev. Astron. Astrophys. **33**, 199 (1995).
19. S. V. W. Beckwith, A. I. Sargent, R. Chini, and R. Güsten, Astron. J. **99**, 924 (1990).
20. Yu. I. Vitinskiĭ, Soln. Dannye **2**, 113 (1982).
21. L. Jetsu, S. Pohjolainen, J. Pelt, and I. Tuominen, Astron. Astrophys. **318**, 293 (1997).
22. E. E. Benevolenskaya, J. T. Hoeksema, A. G. Kosovichev, and P. H. Scherer, Astrophys. J. Lett. **517**, L163 (1999).
23. S. V. Berdyugina and I. Tuominen, Astron. Astrophys. **336**, 25 (1998).
24. H. Korhonen, S. V. Berdyugina, T. Hackman, *et al.,* Astron. Astrophys. **346**, 101 (1999).
25. L. L. Kitchatinov and G. Rüdiger, Astron. Astrophys. **344**, 911 (1999).
26. P. P. Eggleton, Mon. Not. R. Astron. Soc. **151**, 351 (1971).
27. P. P. Eggleton, Mon. Not. R. Astron. Soc. **156**, 361 (1972).
28. L. W. Hartmann and R. W. Noyes, Ann. Rev. Astron. Astrophys. **25**, 271 (1987).
29. L. L. Kichatinov and G. Rüdiger, Pis'ma Astron. Zh. **23**, 838 (1997) [Astron. Lett. **23**, 731 (1997)].
30. J.-F. Donati and A. C. Cameron, Mon. Not. R. Astron. Soc. **291**, 1 (1997).
31. J. Barnes, A. C. Cameron, D. J. James, and J.-F. Donati, Mon. Not. R. Astron. Soc. **314**, 162 (2000).
32. J.-F. Donati, M. Mendel, B. D. Carter, *et al.,* Mon. Not. R. Astron. Soc. **316**, 699 (2000).
33. S. I. Vaĭnshteĭn, Ya. B. Zel'dovich, and A. A. Ruzmaĭkin, *The Turbulent Dynamo in Astrophysics* [in Russian] (Nauka, Moscow, 1980).
34. E. N. Parker, Astrophys. J. **122**, 293 (1955).
35. L. L. Kitchatinov, V. V. Pipin, and G. Rüdiger, Astrophys. J. **315**, 157 (1994).
36. G. Rüdiger and L. L. Kitchatinov, Astron. Astrophys. **269**, 581 (1993).
37. F. Krause and K. Radler, *Mean Field Magnetohydrodynamics and Dynamo* (Akademic, Berlin, 1980; Mir, Moscow, 1984).
38. F. Krause and R. Meinel, Geophys. Astrophys. Fluid Dyn. **43**, 95 (1988).
39. A. Brandenburg, F. Krause, R. Meinel, *et al.,* Astron. Astrophys. **213**, 411 (1989).
40. E. N. Parker, *Cosmical Magnetic Fields: Their Origin and Their Activity* (Clarendon, Oxford, 1979; Mir, Moscow, 1982).
41. S. Chandrasekhar, in *Hydrodynamic and Hydromagnetic Stability* (Clarendon, Oxford, 1961), p. 622.
42. J. O. Stenflo, Astrophys. Space Sci. **144**, 321 (1988).
43. Yu. I. Vitinskiĭ, Kinematika Fiz. Nebesnykh Tel **13**, 76 (1997).
44. Yu. I. Vitinskiĭ, in *Modern Problems of Solar Cyclicity* [in Russian] (GAO RAN, St. Petersburg, 1997), p. 33.
45. A. V. Mordvinov and R. C. Willson, Pis'ma Astron. Zh. (2001) (in press) [Astron. Lett. (2001) (in press)].
46. M. I. Pudovkin and E. E. Benevolenskaya, Pis'ma Astron. Zh. **8**, 506 (1982) [Sov. Astron. Lett. **8**, 273 (1982)].
47. K. B. MacGregor and P. Charbonneau, Astrophys. J. **519**, 911 (1999).

Translated by A. Getling

Astronomy Reports, Vol. 45, No. 10, 2001, pp. 824–833. Translated from Astronomicheskiĭ Zhurnal, Vol. 78, No. 10, 2001, pp. 942–952.

Parameters of the Turbulent Magnetic Field in the Solar Photosphere: Power Spectrum of the Line-of-Sight Field

V. I. Abramenko[1], V. B. Yurchyshyn[1,2], H. Wang[2], and P. R. Goode[2]

[1] *Crimean Astrophysical Observatory, National Academy of Sciences of Ukraine, p/o Nauchnyĭ, Crimea, 334413 Ukraine*

[2] *Big Bear Solar Observatory, Big Bear City, CA 92314, USA*

Received January 3, 2001

Abstract—Ground-based (Big Bear Solar Observatory) and extra-atmospheric (SOHO/MDI) measurements of the photospheric line-of-sight magnetic field of one active and two quiet regions are used to calculate power spectra of the field, taking into account the characteristic function for the diffraction limit of the telescope resolution. At high frequencies, the physically meaningful linear interval in the spectrum extends to a wave number of $k = 4.6$ Mm^{-1} (spatial scale $l = 1.4$ Mm) for the quiet regions and $k = 3.35$ Mm^{-1} ($l = 1.9$ Mm) for the active region. A high-frequency spectral break at $k \geq 3$ Mm^{-1} is associated with the characteristic telescope function; the position of the break and the spectral slope beyond the break do not reflect the turbulent state of the field. As the field recording improves, the break shifts toward higher frequencies. The spectral indices in the physically meaningful linear interval are substantially different for the active and quiet regions: in the active region (NOAA 8375), the spectrum behaves as $E(k) \sim k^{-1.7}$ (very close to the Kolmogorov index, $-5/3$) in the interval $0.78 \leq k \leq 3.35$ Mm^{-1}, while in the quiet regions $E(k) \sim k^{-1.3}$ for $0.77 \leq k \leq 4.57$ Mm^{-1}. This difference can be explained by the additional effect of a small-scale turbulent dynamo in the unperturbed photosphere. In this case, this mechanism can generate at least 6% of the magnetic energy of the photospheric line-of-sight field in quiet regions. © *2001 MAIK "Nauka/Interperiodica".*

1. INTRODUCTION

According to solar dynamo theory, the azimuthal solar magnetic field is generated at the base of the convection zone [1] and is then transferred to the surface via the action of various forces [2]. Thus, the conditions for field generation and field transport through the convection zone are equally important for our understanding of the general pattern of solar (and stellar) magnetism.

Numerical simulations [3, 4] and observations of the solar and stellar photospheres [5, 6] suggest that the magnetic fields in highly conducting media such as convection zones are concentrated in tubes. As shown theoretically [7], the conditions for magnetic-field transport through the convection zone are different for thin and thick tubes: the transport of thin tubes ($d \ll l$) is mainly controlled by the kinematics of the turbulent plasma flow, while the transport of thick tubes is determined by buoyancy forces, curvature, and the Coriolis force. Solar dynamo theory successfully describes the generation of the large-scale fields present in active regions (thick tubes) and their distribution over the solar surface, but fails to describe the field-generation mechanism for quiet regions, where thin tubes dominate. Numerical simulations and theoretical arguments [7, 8] suggest quite convincingly that a small-scale dynamo mechanism related to turbulent flows in the convection zone can generate magnetic fields in the quiet photosphere. If the mechanisms for field generation and transport are different for active and quiet regions, the corresponding parameters of the turbulence should also differ.

Two complementary approaches to the derivation of turbulence parameters from observational data are possible. The classic approach is based on Kolmogorov theory (K41) [9], and includes calculation of both the power spectrum $E(k) \sim k^{\mu}$, $\mu < 0$, and the structure functions

$$S_q(r) = \langle |\mathbf{u}(\mathbf{x}) - \mathbf{u}(\mathbf{x}+\mathbf{r})|^q \rangle \sim r^{\zeta(q)}, \qquad (1)$$

where $q = 1, 2, 3, ...$, [10, 11], as well as comparison of the obtained power-law indices (scaling) with those predicted by K41 theory for fully developed turbulence in an incompressible, uniform, locally isotropic fluid, $\zeta(q) = q/3$. This theory was generalized by Iroshnikov [12] and Kraichnan [13] (IK theory) in an

MHD approximation that assumes that the magnetic field and velocity field obey statistical laws with the same parameters. In IK theory, $\zeta(q) = q/4$. However, turbulent flows do not always strictly agree with Kolmogorov postulates, and the law

$$S_q(r) \sim r^{qh} \quad (2)$$

with $h = \text{const}$ may be violated. To describe such flows, a refined Kolmogorov theory was developed (see, e.g., [10, 11] and references therein), in which h is not necessarily 1/3 or 1/4 but can assume values that continuously fill a certain range. The physical meaning of this generalization becomes clear in the second approach to studying turbulence, which is based on fractal analysis. Mandelbrot's [14] merit was in demonstrating the applicability of fractal analyses to turbulent structures. The existence of multiple possible h values for a turbulent structure means that the structure is not uniform (i.e., it is intermittent) and is made up of a number of subsets (fractals) coexisting in space; each subset has its own scaling law (2) determined by the corresponding value of h [11]. Such a turbulent structure has the property of intermittency, equivalent to multifractality in fractal analysis theory.

The current study consists of two separately published parts, and continues our investigation of the parameters of turbulence in the solar photosphere started in [15], based on the first, classical approach. We use both ground- and space-based observations with high spatial resolution. We analyze power spectra of the line-of-sight magnetic field in the first part of the study and the transverse structure functions of the magnetic field in the second part.

Calculation of the power spectrum of the solar surface magnetic field poses some problems, which must be taken into account in one way or another when interpreting the spectrum. First, only two-dimensional (rather than spatially three-dimensional) spectra can currently be calculated, since observations do not provide magnetic-field distributions along the solar radius comparable in resolution and extent to the distributions in the plane tangent to the solar surface. Second, instrumental noise, turbulence in the Earth's atmosphere (in the case of ground-based observations), and the diffraction limit for the telescope resolution affect the shape of the spectrum.

Power spectra of the line-of-sight magnetic field have been calculated in numerous studies [16–19]. Using magnetograms with a resolution of 2.5″, Nakagawa and Prist [16] obtained spectra with a smooth change in their slopes near wave number $k^* = 0.63$ Mm^{-1} (which corresponds to a spatial scale of 10 Mm) in both an active and an quiet region. At $k < k^*$, before the break, the spectrum was approximated as $E(k) \sim k^{-1}$ in the active region and $E(k) \sim k^{-0.3}$ in the quiet region. Later, Lee *et al.* [19] obtained a power spectrum of the line-of-sight field in an quiet solar region from ground-based observations at the Big Bear Solar Observatory (BBSO) with a spatial resolution of 0.6″. These also revealed a break in the spectrum, but at $k^* = 3.0$ Mm^{-1}, which corresponds to a spatial scale of 2.1 Mm. The behavior of the spectrum was approximated as $E(k) \sim k^{-1}$ before the break and $E(k) \sim k^{-3.7}$ after the break. The availability of extra-atmospheric magnetic-field measurements made on the SOHO station enabled comparative analyses of power spectra for specific regions on the Sun with and without the presence of the terrestrial atmosphere. In this way, atmospheric effects on the shape of the spectrum can be studied, and the spectral parameters can be determined more accurately for both active and quiet regions.

2. OBSERVATIONAL DATA FOR THE LINE-OF-SIGHT MAGNETIC FIELD

We analyzed line-of-sight solar magnetic fields measured at the Big Bear Solar Observatory and on the SOHO satellite with MDI for an active region and the quiet photosphere. AR NOAA 8375 was observed on November 4, 1998, when this active region was at the central meridian. Figure 1a represents a magnetogram of the active region obtained at 17:25 UT with the VMG magnetograph of the BBSO in the Ca I 6103 Å line with a CCD resolution 0.76″ × 0.60″. The resolution limit for the telescope imposed by the Earth's atmosphere is about 2″, which corresponds to a wave number of $k_r = 4.33$ Mm^{-1}.

The MDI magnetogram obtained at 16:32 UT in the Ni I 6767 Å line with a CCD resolution of 0.6″ × 0.6″ is shown in Fig. 1b. The diffraction limit for the resolution of the MDI telescope is 1.25″, which corresponds to a wave number of $k_r = 6.88$ Mm^{-1}. The BBSO magnetogram was carefully aligned with the MDI magnetogram and interpolated to the grid of the latter.

We also considered magnetograms for two areas of the quiet photosphere. The first—QS1, an area 390″ × 300″ in size near the disk center, away from active regions, flocculi, and filaments—was recorded with the BBSO/VMG on September 20, 1998 under good, stable seeing conditions. The magnetogram for this area is shown in Fig. 2a. The second quiet area, QS2 (Fig. 2b), formed a fragment of the field of view of the MDI magnetogram in which AR 8375 was recorded. This is an area of weak field 350″ × 150″ in size to the southwest of the leading spot. The Hα images obtained on that day at the BBSO show

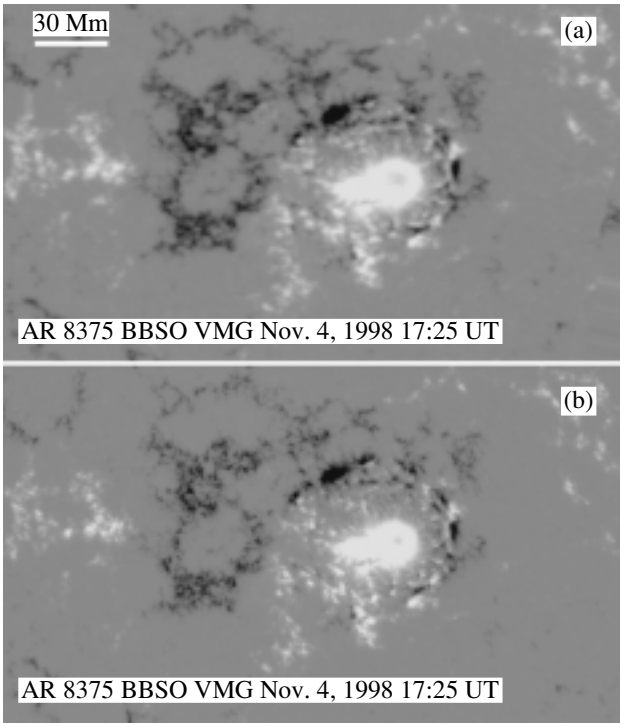

Fig. 1. Magnetograms of the line-of-sight magnetic field of active region NOAA 8375. Cells where the field exceeds 75 mT are shown in white for N polarity and in black for S polarity. (a) Magnetogram obtained with the VMG in BBSO ground-based measurements; (b) extra-atmospheric SOHO/MDI measurements. North is at the top, and west is to the right.

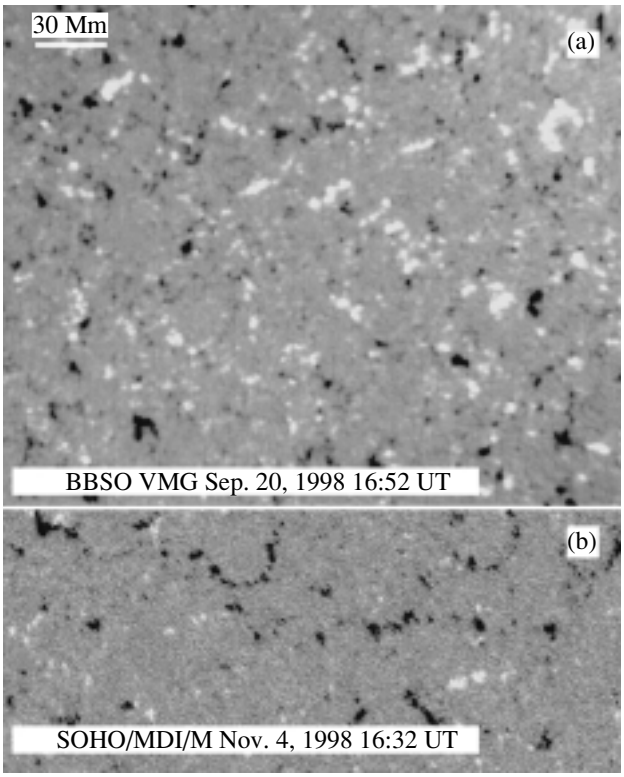

Fig. 2. Magnetograms of the line-of-sight magnetic field in two quiet areas. Cells where the field exceeds 5 mT are shown in white for N polarity and in black for S polarity. (a) Magnetogram of quiet region QS1 near the disk center obtained with the VMG in BBSO ground-based measurements; (b) magnetogram of quiet photospheric region QS2 to the southwest of the leading spot of AR 8375, from extra-atmospheric SOHO/MDI measurements. North is at the top, and west is to the right.

that only a small fraction of this area was occupied by flocculi.

3. ANALYSIS OF POWER SPECTRA

A detailed description of the procedure used to calculate the power spectra is given in [15]. By applying the mean-value theorem to the integral form of the two-dimensional spectrum [10], we were able to obtain a formula (see expression (8) in [15]) for the computation of a one-dimensional spectrum $E(k)$ with small errors in the powers, since a large number of points are averaged in the annulus between $\mathbf{k}$ and $\mathbf{k}+\mathbf{dk}$.

We measured the cell sizes of the magnetogram grid in megameters, so that the relationship between the wave number k in Mm^{-1} and the linear scale l in Mm is $l = 2\pi/k$. Since the magnetogram areas were different, we normalized all spectra by dividing them by the magnetogram area. Figure 3 shows spectra of the active region NOAA 8373 calculated from the BBSO and MDI magnetograms. In the wave-number range $0.16 < k < 1.4$ Mm^{-1}, the spectra are very similar and can be approximated by the law $E(k) \sim k^{-1.7}$. The difference between them is that the segment with slope $\mu = -1.7$ can be traced over a longer interval (toward shorter wavelengths) in the MDI spectrum than in the BBSO spectrum—to $k = 2.1$ Mm^{-1}. Both spectra depart downward from a line with slope -1.7 beginning at a wave number k^* (the position of the short-dashed line in Fig. 3), which is about a factor of three smaller than the wave number corresponding to the telescope resolution limit. In the BBSO spectrum (Fig. 3a), the break is appreciable at $k^* = 1.43$ Mm^{-1}, which corresponds to the ratio $k_r/k^* = 4.33/1.43 = 3.03$, while this ratio for the MDI spectrum is $k_r/k^* = 6.88/2.1 = 3.28$. In both cases, we are dealing with the same active region, equal telescope resolutions, and very similar heights of formation of the radiation in the photosphere. Therefore, there are good reasons to believe that the difference between the spectra results from the effects of the Earth's atmosphere on the BBSO measurements.

The subsequent steps in correcting the spectra, described in detail in [15], are reflected in Fig. 3. In

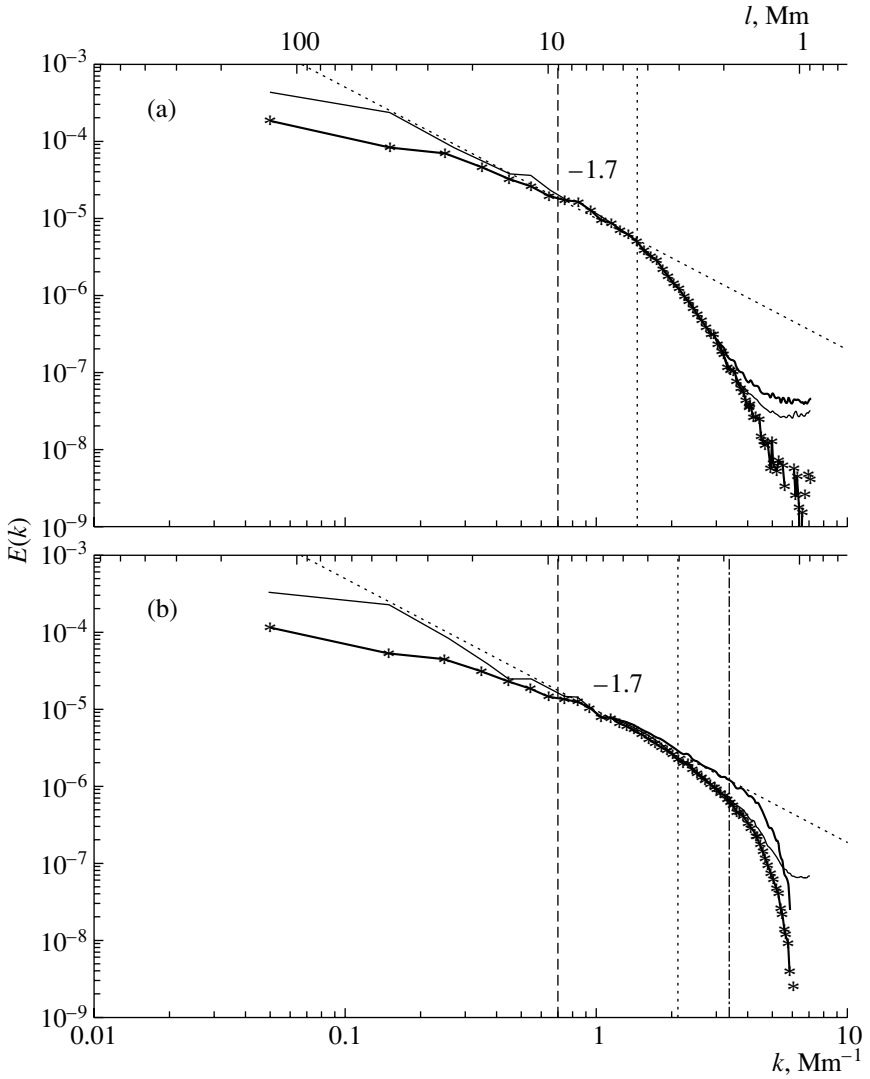

Fig. 3. (a) Spectra of AR 8375 obtained from the BBSO magnetogram: the light solid curve is the original spectrum, the heavy solid curve is the spectrum after blocking the spot, and the crosses represent the spectrum without the spot and with the noise subtracted [denoted E(AR/BBSO)]. (b) Spectra of AR 8375 obtained from the MDI magnetogram: the light solid curve is the original spectrum, and the crosses represent the spectrum without the spot and with the noise subtracted [denoted E(AR/MDI)]; the heavy solid curve is the E(AR/MDI) spectrum corrected for the effects of the diffraction limit of the telescope resolution [denoted E(AR/MDI/C)]. In both plots, the long-dashed line denotes the upper bound of the linear interval in which the spot no longer has any effect and the slope is still −1.7, the short-dashed line indicates the lower bound of this interval in the original spectra, and the dash-dot line corresponds to the lower bound of this interval in the corrected spectrum E(AR/MDI/C). The vertical axis plots the logarithm of the normalized power spectrum in units of 2×10^{15} J/m.

both magnetograms, the power on scales $l > 9$ Mm ($k < 0.7$ Mm^{-1}) was underestimated due to blocking of the zone of the large leading spot, while the spectrum on smaller scales was unaffected. Taking into account the instrumental noise was important only at very short wavelengths, $k > 3.8$ Mm^{-1} for the BBSO magnetogram and $k > 4.7$ Mm^{-1} for the MDI magnetogram. We introduce the notation E(AR/BBSO) and E(AR/MDI) for these noise-free spectra of the spot-free active region obtained from the BBSO and MDI data, respectively.

For the extra-atmospheric (MDI) field measurements, we calculated the characteristic function of the MDI telescope $G^2(k)$ (the system's response to a pulse with unit amplitude [21]) using the Rayleigh criterion for the diffraction limit of the telescope resolution [15] and employed it to obtain a corrected spectrum of the active region ($E^{(c)}(k)$), which we denote E(AR/MDI/C):

$$E^{(c)}(k) = E(k)G^{-2}(k). \quad (3)$$

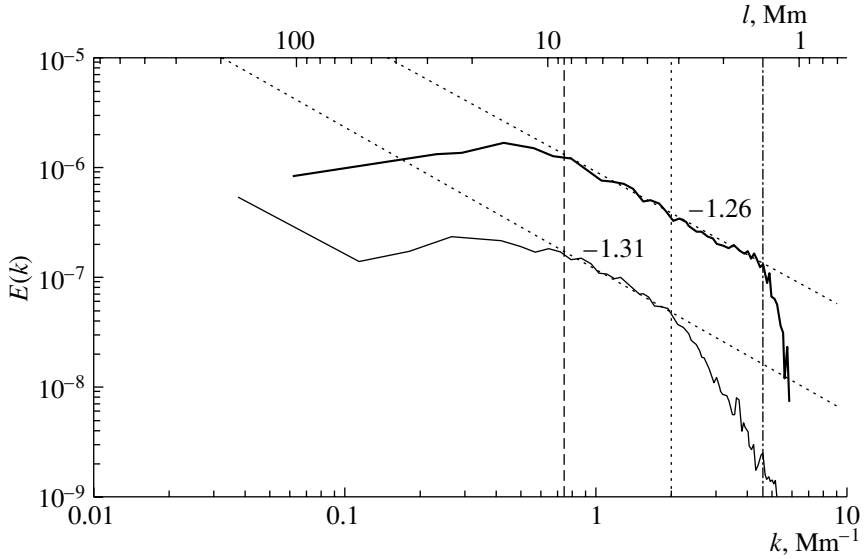

Fig. 4. Spectrum E(QS1/BBSO) of quiet region QS1 (light solid curve) from ground-based measurements and spectrum E(QS2/MDI/C) of quiet region QS2 from extra-atmospheric measurements (heavy solid curve). The long-dashed line indicates the upper bound of the linear interval. The dotted line marks the lower bound of the linear interval in the E(QS1/BBSO) spectrum and the dot-dash line the lower bound in the E(QS2/MDI/C) spectrum. The axes are the same as in Fig. 3.

In this spectrum, the linear section with slope $\mu = -1.7$ extends to $k = 3.35$ Mm^{-1} (Fig. 3b), which corresponds to $G^2(k) \approx 0.32$. Thus, our correction for the diffraction limit of the telescope resolution on the noise-free spectrum of the active region based on formula (3) has somewhat broadened the linear section (from 2.1 to 3.35). However, beyond $k = 3.35$ Mm^{-1}, the spectrum still falls below the line $\mu = -1.7$, probably due to the fact that the noise-free spectrum $E(k)$ approaches zero faster than the function $G^2(k)$ as k increases [see formula (3)]. The ratio k_r/k^* for the spectrum E(AR/MDI/C) is 2.05.

Figure 4 shows the spectra of the quiet regions QS1 and QS2. In both, we have taken into account the effects of noise, and the spectrum for QS2 (obtained from the MDI data) has been corrected using (3) and the frequency characteristic $G^2(k)$ of the MDI telescope. This spectrum is denoted E(QS2/MDI/C) and shown by the heavy curve in Fig. 4. We can see that in the quiet areas the frequency characteristic $G^2(k)$ extends the spectrum with a constant slope further than into the active region, to $k = 4.57$ Mm^{-1}, where the function $G^2(k)$ itself falls to 0.12. The ratio k_r/k^* is 1.5. The rapid decline in power beyond the break at $k \approx 4.57$ Mm^{-1} also depends on the ratio of the rates of decline with increasing k for $G^2(k)$ and for the noise-free spectrum.

For a comparative analysis, we first took three active-region spectra (listed in order of increasing quality): the noise-free spectrum derived from ground-based observations, E(AR/BBSO), the noise-free spectrum derived from extra-atmospheric observations, E(AR/MDI), and the noise-free, extra-atmospheric spectrum corrected for the diffraction limit of the telescope resolution, E(AR/MDI/C). Second, we took two spectra of quiet areas: the noise-free spectrum of region QS1 derived from ground-based observations, E(QS1/BBSO), and the noise-free spectrum of region QS2 derived from extra-atmospheric observations and corrected for the diffraction limit of the telescope resolution, E(QS2/MDI/C). In each spectrum, we visually chose three intervals—low-frequency, medium-frequency, and high-frequency—such that their bounds corresponded to changes in the spectrum slope. If the density of spectral points is sufficiently high, the bounds of the intervals can be chosen in various ways. After making several such estimates, we computed the spectral slope μ and its standard deviation for each interval. The results are schematically presented in Fig. 5 and given in the table, where columns 2 and 3 correspond to the interval bounds l_1 and l_2 on a linear scale, columns 4 and 5 correspond to the same bounds in wave numbers, k_1 and k_2, and column 6 gives the spectral slope μ.

The spectra of the active region in the low- and medium-frequency intervals have very similar slopes, $\mu = -0.69 \ldots -0.74$ and $\mu = -1.67 \ldots -1.74$, respectively. The latter value is very close to the

Linear intervals and spectral indices μ; l_1 and k_1 correspond to the low-frequency bound of the interval, and l_2 and k_2 to its high-frequency bound

Spectrum	l_1, Mm	l_2, Mm	k_1, Mm^{-1}	k_2, Mm^{-1}	μ
Low-frequency interval					
E(AR/MDI/C)	127.5 ± 2.7	13.4 ± 3.6	0.049 ± 0.005	0.49 ± 0.13	-0.69 ± 0.03
E(AR/MDI)	127.5 ± 2.7	13.4 ± 3.6	0.049 ± 0.005	0.49 ± 0.13	-0.69 ± 0.03
E(AR/BBSO)	127.5 ± 2.7	13.4 ± 3.6	0.049 ± 0.005	0.49 ± 0.13	-0.74 ± 0.08
E(QS2/MDI/C)	101.6 ± 3.1	14.5 ± 1.1	0.062 ± 0.006	0.43 ± 0.05	0.32 ± 0.02
E(QS1/BBSO)	54.9 ± 3.3	18.9 ± 4.3	0.114 ± 0.008	0.34 ± 0.08	0.49 ± 0.10
Medium-frequency interval					
E(AR/MDI/C)	8.0 ± 0.6	1.89 ± 0.20	0.78 ± 0.07	3.35 ± 0.36	-1.74 ± 0.06
E(AR/MDI)	8.1 ± 0.5	2.99 ± 0.19	0.77 ± 0.05	2.10 ± 0.13	-1.67 ± 0.04
E(AR/BBSO)	11.0 ± 2.5	4.40 ± 0.25	0.59 ± 0.13	1.43 ± 0.08	-1.72 ± 0.15
E(QS2/MDI/C)	8.2 ± 0.7	1.38 ± 0.05	0.77 ± 0.06	4.57 ± 0.16	-1.26 ± 0.02
E(QS1/BBSO)	8.8 ± 1.2	3.17 ± 0.07	0.72 ± 0.11	1.98 ± 0.04	-1.31 ± 0.07
High-frequency interval					
E(AR/MDI/C)	1.48 ± 0.02	1.17 ± 0.02	4.25 ± 0.05	5.37 ± 0.10	-6.37 ± 0.13
E(AR/MDI)	2.87 ± 0.17	1.36 ± 0.10	2.20 ± 0.13	4.62 ± 0.34	-3.00 ± 0.15
E(AR/BBSO)	3.60 ± 0.19	1.65 ± 0.17	1.74 ± 0.09	3.84 ± 0.37	-4.35 ± 0.08
E(QS2/MDI/C)	1.37 ± 0.02	1.10 ± 0.03	4.57 ± 0.07	5.68 ± 0.16	-8.12 ± 0.54
E(QS1/BBSO)	2.77 ± 0.12	1.74 ± 0.31	2.27 ± 0.09	3.70 ± 0.68	-3.88 ± 0.11

Kolmogorov index for a turbulent spectrum $E(k) \sim k^{-5/3}$. We conclude that the power spectrum of the line-of-sight magnetic field in the active region has an index very close to the Kolmogorov value, at least for scales from 8 to 2 Mm. In view of the shape of the spectrum before blocking of the spot (Fig. 3), we cannot rule out a Kolmogorov structure for the spectrum of the active region on scales from 40 to 2 Mm.

In the third, high-frequency interval, the three spectra for the active region behave differently, and the k value corresponding to the spectral break increases with the quality of the data. Beyond the break, the three spectra have different slopes.

The situation is qualitatively the same in the spectra of quiet areas: the slopes are similar in the low- and medium-frequency intervals but different in the high-frequency interval. The high-frequency break also moves to the right as the quality of the data improves. The difference from the active-region spectra is that the slopes are different.

In quiet areas, no regular structures seem to be present on scales $l > 10$ Mm (Fig. 2), which would be manifest as a positive spectral slope in the low-frequency interval. Therefore, the turbulent spectrum sets in on scales $l < 8$ Mm. As we saw, the active-region spectrum for $l < 9$ Mm can be assumed to be free of the influence of the large-scale spot; i.e., it is definitely turbulent. Thus, the middle portions of the schematic in Fig. 5 and of the table provide information on the parameters of the turbulent spectra in active and quiet regions. We can see that they differ substantially: whereas the spectral index for the active region is close to the Kolmogorov value $-5/3$, its value for the quiet areas is about -1.3, which corresponds to neither a Kolmogorov nor a Kraichnan ($-3/2$) index. We note that the difference exceeds the errors in the computed values μ (see the table).

As shown above, the position of the spectral break between the medium- and high-frequency intervals (Fig. 5) and the spectral slope beyond the break are completely determined by the effects of the frequency characteristic of the recording system on the spectrum. Apparently, they do not reflect the physical state of the magnetic field. An analysis of the schematic in Fig. 5 supports this conclusion. In the spectra of both the active region and quiet areas, the higher the data quality (the broader the frequency characteristic of the recording system), the further the turbulent spectrum extends toward high frequencies,

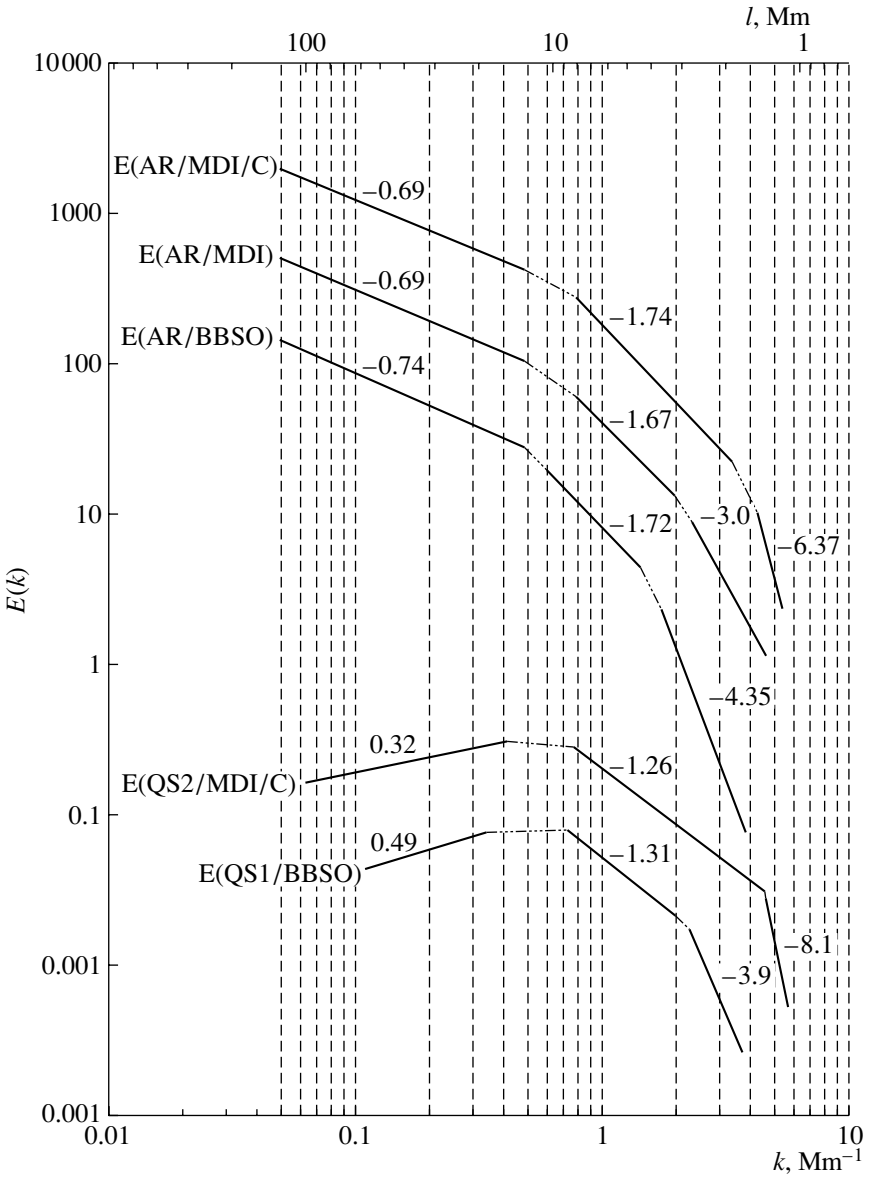

Fig. 5. Schematic representation of the spectra. The axes are the same as in Fig. 3. The spectra are arbitrarily shifted in the vertical direction. The vertical axis is scaled in relative units. The horizontal positions of the breaks are preserved.

with its slope preserved until the break and increasing beyond the break. This is in complete agreement with the results of a spectral analysis of linear systems [21]. According to our estimates, this power-spectrum break occurs at frequencies about a factor of three lower than the frequency corresponding to the resolution limit of the telescope in the original (raw) spectrum and a factor of 1.5–2 lower in the spectrum corrected for the frequency characteristic.

4. DISCUSSION

In recent years, power spectra of photospheric fields—Doppler velocity fields [22, 23], velocity and brightness fields [23, 24], and line-of-sight magnetic fields [16, 19]—have been actively studied. Quantitative analyses of the spectral slopes reveal the presence of a spectral break at wave numbers $k \approx 0.6$ Mm^{-1} [16] or $k \approx 1$ Mm^{-1} [24]; the most recent, high-spatial-resolution ground-based observations more and more frequently yield $k \approx 3$ Mm^{-1} [19, 22, 23, 25]. The wave number $k = 3$ Mm^{-1} corresponds to a linear scale of $l \approx 2.1$ Mm, or $3''$, which coincides with the size of the largest granules. For this reason, the presence of a break in the spectrum at $k \approx 3$ Mm^{-1} is often interpreted as the manifestation of a specific granular-scale turbulent regime [19, 22,

26] and, in analyses of magnetic-field spectra [19], as evidence for an imprint of the granular structure in the magnetic field. When a slope of $-5/3$ is found beyond the break [22, 25], the presence of well-developed Kolmogorov turbulence for the granules is assumed, and if the slope exceeds 5/3, this is taken to indicate an important role of dissipation mechanisms on granular scales (in particular, magnetic-field dissipation [19]).

Our findings testify that the presence of such spectral breaks result from the inevitable loss of information during the recording of the field measurements. The scale of $3''$ ($k = 2.9$ Mm^{-1}) is not distinguished in our spectra, and if observations are made beyond the terrestrial atmosphere, the spectrum extends with the same slope to $k = 3.35$ Mm^{-1} in an active region and to $k = 4.57$ Mm^{-1} in a quiet area. However, ground-based observations with very good spatial resolution of order $1''$ (which corresponds to a limiting-resolution frequency of 8.7 Mm^{-1}) and without spectral corrections based on the characteristic function (as in [22, 23, 25]) should, according to our estimates, demonstrate a high-frequency break due to the limited passband of the characteristic function, at a frequency about a factor of three lower than the limiting-resolution frequency; i.e., at $k \approx 8.7/3 = 2.9$ Mm^{-1}. This was actually observed in [22, 23, 25]. At the very high resolution $k = 4.9$ Mm^{-1} ($1.8''$) and after careful correction of the spectrum using the atmospheric characteristic function, Lee *et al.* [19] detected a break at a frequency a factor of 1.6 lower than the limiting resolution, in full agreement with our conclusions concerning the expected position of the break in corrected spectra.

The instrumental origin of the high-frequency spectral break and turndown has long been known to astronomers studying the distributions of frequencies at which flares of a given energy occur on stars [27]. The energy spectra of flares have three well-defined sections—a flat, low-frequency section due to the lack of flares of such high energies on the given star, an linear medium-frequency section with some non-zero spectral index (the physically meaningful section), and a sharp break with a turndown at high frequencies, due to the existence of a detection limit for extremely weak flares. We see that this situation is completely analogous to that considered here in terms of the presence of three spectral intervals and their physical meaning. Since the high-frequency break in the power spectra has an instrumental origin, there are some grounds to suppose that the spectra in both the active and quiet regions extend toward short wavelengths with constant slopes. If so, this implies that as the scale is reduced (at least, to $l = 1.4$ Mm, $k = 4.57$ Mm^{-1}) the magnetic eddy-viscosity forces are not yet manifest. We investigated this possibility by extending the spectra to their intersection (Fig. 6), which occurred at a scale of order $l \approx 40$ km. It is interesting that precisely this order of magnitude is noted in the context of the minimum sizes of magnetic tubes in the photosphere [28–30].

The conspicuous difference in the spectral indices between the active and quiet regions supports the idea that the mechanisms for field generation and transport are different in active and quiet regions of the Sun (see Introduction). The spectrum in the quiet areas, which is flatter than $E(k) \sim k^{-5/3}$, can be interpreted as a manifestation of an additional mechanism of magnetic-energy generation in the quiet photosphere due to the action of a small-scale turbulent dynamo [7, 8]. Indeed, in the framework of the Kolmogorov theory of developed turbulence [9], energy is supplied to the system on scales L of the order of the size of the system itself and cascades to smaller-scale structures without any additional energy input on scales much smaller than L. If we assume that the additional magnetic-field generation mechanism associated with the small-scale turbulent dynamo operates in the quiet photosphere on scales $l < 8$ Mm ($k > 0.77$ Mm^{-1}), then, according to [10], the extra magnetic energy produced by this mechanism will be redistributed over the spectrum (in principle, in both directions), resulting in a spectrum more gently sloped than a Kolmogorov spectrum.

Based on the corrected extra-atmospheric spectrum of quiet region QS2 (spectrum E(QS2/MDI/C in Fig. 6), we estimated a lower limit for the relative share of energy produced by the small-scale dynamo, assuming that the spectral range $k < 0.77$ Mm^{-1} is not affected by this mechanism. The total energy of the process in the linear range can be estimated as the area S of the trapezoid enclosed by the bounds of this linear range $k = 0.77$ Mm^{-1} and $k = 4.57$ Mm^{-1} on the two sides, the zero level from below, and the straight line with a slope of -1.26, which best fits the spectrum, from above. The energy of the Kolmogorov cascade from scales $l > 8$ Mm in the same range is represented by the area S_k of the trapezium bounded from above by the straight line with a slope of $-5/3$. The quantity $(S - S_k)/S$ can be considered as the share of the additional magnetic energy generated in the quiet photosphere by the small-scale dynamo mechanism. According to our estimate, it amounts to 6.4% of the total magnetic-field energy in the range considered (the shaded area in Fig. 6). Since the position of the high-frequency bound $k = 4.57$ Mm^{-1} of the linear spectral range (Fig. 6) can move to the right with improvement of the resolution of space telescopes, this estimate should be regarded as a lower limit. Theoretical calculations for small-scale

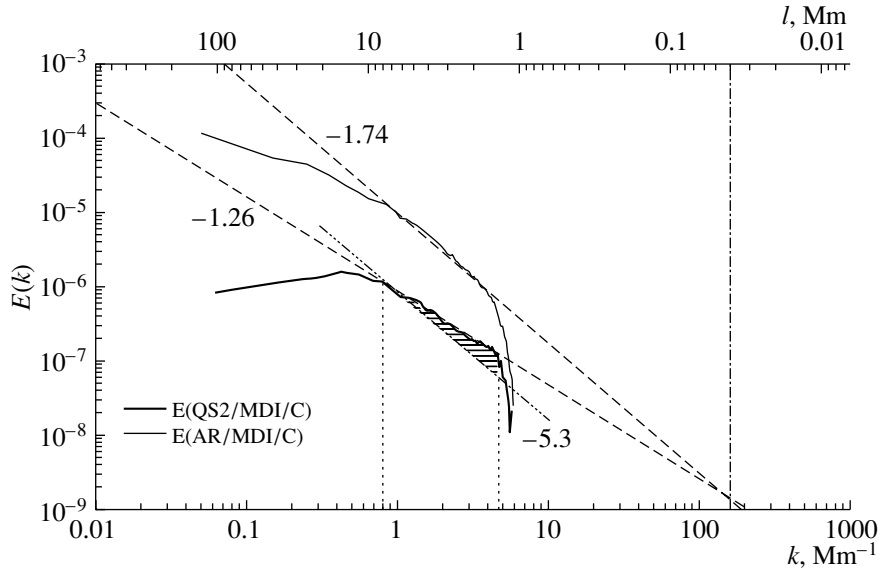

Fig. 6. Normalized corrected spectra of the active and quiet regions according to the extra-atmospheric observations. The spectrum E(AR/MDI/C) is shown by the light solid curve, and the spectrum E(QS2/MDI/C) by the heavy solid curve. The dashed lines representing the best linear fit to the spectra in the inertial ranges are extended to their intersection, at a scale $l \approx 40$ km (the vertical dot-dash line). The shaded area between the line with the Kolmogorov slope $-5/3$ and the line with observed slope -1.26 in the inertial range (bounded by the vertical dotted lines) corresponds to a lower limit for the share of magnetic energy generated by the small-scale turbulent dynamo in the quiet photosphere. The axes are the same as in Fig. 3.

turbulent dynamo [8] show that up to 20% of the total magnetic energy can be produced by this mechanism.

The active-region spectrum is very close to a Kolmogorov spectrum. MDI observation of this active region in the Ni I 6767 Å line extending over 44 h demonstrated small pores constantly separating from the main spot and being carried by turbulent streams to the periphery. This pattern is in qualitative agreement with Kolmogorov's hypothesis that the energy cascade should be directed from larger structures to smaller ones in a turbulent medium. It is not ruled out that the spot is part of the turbulent cascade and that our blocking of the spot (see Section 3) and subsequent analysis of spot-free spectra were unnecessary. In this case, the turbulence in the active region can be attributed to scales from 40 Mm to at least 1.9 Mm. Unfortunately, our estimation of the power-spectrum index for the magnetic fields in active regions is based on data for only one (although very typical) active region. Nevertheless, the Kolmogorov nature of the magnetic-field turbulence in active regions was also deduced in [31] from the distributions of the energies of magnetic elements according to size. Statistical analyses should make use of data for numerous regions, both active and quiet.

5. CONCLUSIONS

The basic results of our investigation of the power spectra of the line-of-sight magnetic field calculated from ground-based (BBSO) and extra-atmospheric (SOHO/MDI) observations of both an active and quiet regions are as follows.

(1) We obtained reliable power spectra of the line-of-sight magnetic field, which extend toward high frequencies to wave number $k = 4.57$ Mm^{-1} ($l = 1.4$ Mm) in the quiet region and $k = 3.35$ Mm^{-1} ($l = 1.9$ Mm) in the active region.

(2) The power spectra in the quiet and active regions differ appreciably. In the active region, the spectrum at 8–1.9 Mm behaves as $E(k) \sim k^{-1.7}$, which is very close to a Kolmogorov spectrum for homogeneous, isotropic turbulence with an index of $-5/3$. In the quiet regions, the spectrum is more gently sloped, with an index of -1.3 at 8–1.4 Mm.

(3) The spectra of the same active region (as well as those of two different quiet areas) obtained in ground- and space-based measurements are in good agreement in the inertial range; however, the high-frequency bound of this range should be determined separately for each type of observation.

(4) Changes in the spectral slope at high frequencies (the high-frequency spectral break, which coincides in position with the high-frequency bound of the physically meaningful inertial range) are determined by the resolution and quality of the data recording; namely, by the influence on the spectrum of the characteristic function for the data-recording system and the noise-correction techniques. As the

field recording quality improves, the break shifts toward higher frequencies. Such a break is present at wave numbers about a factor of three smaller than the wave number corresponding to the limiting resolution (specified by the diffraction limit of the telescope resolution in extra-atmospheric observations or the atmospheric turbulence in ground-based observations). In the corrected spectra, i.e., after noise subtraction and division by the square of the characteristic function, the break moves to frequencies a factor of 1.5–2 lower than the limiting-resolution frequency. However, none of the corrections make it possible to consider the spectrum trustworthy and physically meaningful up to the limiting-resolution frequency; the last high-frequency break and the spectral slope beyond it are not related to the physical state of the magnetic field. It is probable that this conclusion is relevant not only for magnetic spectra.

ACKNOWLEDGMENTS

We are indebted to Prof. J.W. Lee for a highly useful critical discussion of this work, to Prof. A.G. Kosovichev for the availability of the SOHO/MDI data, and to Dr. É.A. Baranovskiĭ, Dr. D.N. Rachkovskiĭ, and K.V. Parchevskiĭ for very useful discussions of some mathematical aspects of this study. This work was supported by the Ministry of Education and Science of Ukraine and by grants from NSF-ATM (97-14796) and NASA (NAG5-4919).

REFERENCES

1. S. I. Vaĭnshteĭn, Ya. B. Zel'dovich, and A. A. Ruzmaĭkin, *Turbulent Dynamo in Astrophysics* (Nauka, Moscow, 1980).
2. E. Parker, *Cosmical Magnetic Fields, Their Origin and Their Activity* (Clarendon, Oxford, 1979).
3. M. Meneguzzi, U. Frisch, and A. Pouquet, Phys. Rev. Lett. **47**, 1060 (1981).
4. M. Meneguzzi and A. Pouquet, J. Fluid Mech. **205**, 297 (1989).
5. J. O. Stenflo, Astron. Astrophys. Rev. **1**, 3 (1989).
6. S. Saar, in *The Sun and Cool Stars: Activity, Magnetism, Dynamos (IAU Coll. 130),* Ed. by I. Tuominen, D. Moss, and G. Rudiger (Springer-Verlag, Berlin, 1991), p. 389.
7. K. Petrovay and G. Szakaly, Astron. Astrophys. **274**, 543 (1993).
8. F. Cattaneo, Astrophys. J. Lett. **515**, L39 (1999).
9. A. N. Kolmogorov, Usp. Fiz. Nauk **93** (3), 476 (1967) [Sov. Phys. Usp. **10**, 734 (1968)].
10. A. S. Monin and A. M. Yaglom, *Statistical Fluid Mechanics* (Nauka, Moscow, 1967; MIT, Cambridge, 1975), Vol. 2.
11. U. Frisch, *Turbulence. The Legacy of A. N. Kolmogorov* (Cambridge Univ. Press, Cambridge, 1995).
12. R. S. Iroshnikov, Astron. Zh. **40**, 742 (1963) [Sov. Astron. **7**, 566 (1963)].
13. R. H. Kraichnan, Phys. Fluids **8**, 1385 (1965).
14. B. B. Mandelbrot, *The Fractal Geometry of Nature* (New York, 1983).
15. V. Abramenko, V. Yurchyshyn, H. Wang, and P. R. Goode, Sol. Phys. (2001) (in press).
16. Y. Nakagawa and E. R. Prist, Astrophys. J. **179**, 949 (1973).
17. Y. Nakagawa and R. H. Levine, Astrophys. J. **190**, 441 (1974).
18. E. Knobloch and R. Rosner, Astrophys. J. **247**, 300 (1981).
19. J. W. Lee, J. C. Chae, H. S. Yun, and H. Zirin, Sol. Phys. **171**, 269 (1997).
20. G. M. Jenkins and D. G. Watts, *Spectral Analysis and Its Applications* (Holden-Day, San Francisco, 1968; Mir, Moscow, 1972), Vol. 2.
21. Ya. I. Khurgin and V. P. Yakovlev, *Compact Functions in Physics and Technical Fields* [in Russian] (Nauka, Moscow, 1971).
22. R. Muller, *Solar and Stellar Granulation,* Ed. by R. Rutten and G. Severino (Kluwer, Dordrecht, 1989), NATO ASI Ser., Ser. C **263**, 101 (1989).
23. G. Consolini, E. Berrilli, E. Pietropaolo, *et al.,* in *Proceedings of the 9th European Meeting on Solar Physics: Magnetic Fields and Solar Processes, Florence, 1999,* Eur. Space Agency SP-448, **1**, 209 (1999).
24. D. Y. Chou, B. J. LaBonte, D. C. Braun, and T. L. Duvall, Jr., Astrophys. J. **372**, 314 (1991).
25. O. Espagnet, R. Muller, Th. Roudier, and N. Mein, Astron. Astrophys. **271**, 589 (1993).
26. Th. Roudier, R. Muller, P. Mein, *et al.,* Astron. Astrophys. **248**, 245 (1991).
27. R. E. Gershberg, Astrofizika **22**, 531 (1985).
28. B. Schmieder, M. Rovira, G. M. Simnett, *et al.,* Astron. Astrophys. **308**, 957 (1996).
29. E. N. Parker and A. Thyagaraia, Sol. Phys. **189**, 45 (1999).
30. H. Lin and T. Rimmele, Astrophys. J. **514**, 448 (1999).
31. S. I. Gopasyuk, Kinematika Fiz. Nebesnykh Tel **16** (2), 138 (2000).

Translated by A. Getling

Astronomy Reports, Vol. 45, No. 10, 2001, pp. 834–840. Translated from Astronomicheskiĭ Zhurnal, Vol. 78, No. 10, 2001, pp. 953–960.

The Three-Dimensional Structure of the Solar Corona

S. L. Koutchmy[1], V. L. Merzlyakov[2], and M. M. Molodenskiĭ[2]

[1]*Institute of Astrophysics, Paris, France*
[2]*Institute of Terrestrial Magnetism, the Ionosphere, and Radio Wave Propagation, Russian Academy of Sciences, Troitsk, Moscow oblast, 142190, Russia*

Received January 29, 2001

Abstract—The surface where the radial component of the solar magnetic field changes sign is computed for a minimum corona. It is shown that (1) the projection of the folds of this surface onto the plane of the sky is consistent with the helmet structures observed during the eclipse of June 30, 1954; (2) there are type 1 and type 2 helmets, according to the well-known classification of coronal structures; (3) some elements of this sign-change surface of the radial field can be classified as so-called envelopes. The results obtained suggest that more complex coronal structures can be described in a similar way. An MHD model of polar plumes is considered. © *2001 MAIK "Nauka/Interperiodica".*

1. INTRODUCTION

Until recently, only general features of the shape of the solar corona could be described. Structures of the quiescent, active, and intermediate corona have been distinguished. Predictions of the shape of the corona using synoptic maps of the Sun and taking into account the phase of the solar cycle (as a rule, at the nearest eclipse) describe a more or less tousled corona with streamers originating from active regions. However, almost every eclipse has presented surprises.

Recently, the situation has changed, though not appreciably for the better. We are still far from a full comprehension of coronal structures; however, complete pictures of the corona are now always available. Forecasting coronal structures is not necessary, since there is free access to SOHO, LASCO-2, or LASCO-3 observations. More and more, studies have been reduced to listing various types of data, which are growing exponentially in number. Almost no attempts to analyze such data in a unified way have been undertaken. In the present work, we attempt a unified analysis of observational data for coronal structures.

We believe that all the main structures observed in the solar corona (type 1 and type 2 helmets, the structures called envelopes by Bugoslavskaya [1], and polar plumes) appear via the projection of a heliospheric layer, i.e., the $B_r = 0$ surface, onto the plane of the sky. This is valid for the structure of the total corona of June 30, 1954 as a minimum corona, as well as for individual elements of some other cases.

A model of the $B_r = 0$ surface was constructed for November 3, 1994 using data derived from synoptic maps [2, 3]. The computations were in agreement with the real structure of the corona. However, these computations used an approximation that is usually assumed to be valid only for distances $r > 2.5R_\odot$, where the magnetic field lines are stretched in the radial direction by the solar wind. In the present work, we perform an accurate computation of the $B_r = 0$ surface using a potential approximation for the field.

It is well known [4] that the solar corona consists of an isotropic component, which is described by hydrostatic equilibrium (with a scale height of $kT/mg \sim 150\,000$), and structure, which is described by the MHD equations. To a first approximation, structures of the solar corona are equilibrium plasma configurations in magnetic and gravitational fields. Increased plasma densities are observed near surfaces where the radial component of the magnetic field changes sign, $B_r = 0$; this is well established for quiescent filaments but less so for coronal structures. In this connection, we cite [5], in which the positions of the bases of helmets (discontinuities in the plasma density) are shown to coincide with filaments situated on a $B_r = 0$ surface. This became an important observational basis for modeling the $B_r = 0$ surface to study various structures in the solar atmosphere [6].

In addition, the Lorentz force is the sole force that can compensate the weight of dense plasma in the solar gravitational field. If $B_r \neq 0$ at some point of the corona, the Lorentz force has a tangential component for any direction of the current. In other words, the

1063-7729/01/4510-0834$21.00

gravitational force can be compensated by the $\frac{1}{c}[jB]$ force only on a $B_r = 0$ surface. The structure, density, temperature, and other parameters of this layer are considered in [7, 8].

Our work presents the $B_r = 0$ surface calculated in a potential approximation for the magnetic field, and compares this surface with the structure of the corona observed on June 30, 1954.

2. POTENTIAL APPROXIMATION FOR THE MAGNETIC FIELD

The magnetic field above the photosphere is usually represented as a sum of spherical harmonics. A potential approximation provides a good representation of the field in this case [9]. In this approximation, the measured magnetic field at the photosphere and certain assumptions about the field at distances $r = 2{-}3R_\odot$ [10] or requirements about how the field falls of as $r \to \infty$ serve as boundary conditions. There are also solutions of the general MHD equations that correspond to the motion of plasma in magnetic and gravitational fields, and describe configurations generated by the solar wind [11].

For the field component B_r, we use an expansion representing a harmonic potential:

$$B_r = \sum_n^N \sum_\mu a_n^\mu \left(\frac{R_\odot}{r}\right)^{n+2} P_n\left(\cos\gamma_n^\mu\right), \quad (1)$$

where P_n are Legendre polynomials of degree n, $\cos\gamma_n^\mu = \cos\theta_n^\mu \cos\theta + \sin\theta_n^\mu \sin\theta \cos(\varphi - \varphi_n^\mu)$, and γ_n^μ is the angle between the directions θ, φ and $\theta_n^\mu, \varphi_n^\mu$ (i.e., the angle between the θ and φ directions in the initial frame and in a frame rotated with respect to the original frame). In the Appendix, we present relations between the coefficients a_n^μ and the usual expansion coefficients A_{nk}, B_{nk}.

To study extended coronal structures similar to helmets, we must primarily understand some configuration of the large-scale magnetic field that enables the use of a small number ($N \le 5{-}6$) of first harmonics in (1). Such large-scale magnetic fields are manifest in the photosphere as regions separated by long-lived filaments and filament channels. The locations of these filaments correspond to neutral lines $B_r = 0$ in the photosphere [12, 13]. Therefore, we can use filaments to determine the parameters of (1) in the absence of magnetograph measurements.

3. THE SHAPE OF THE $B_r = 0$ SURFACE AND THE CORONA OF JUNE 30, 1954

It is probable that the eclipse of June 30, 1954 corresponds to the lowest solar activity over the past several decades. The mean monthly Wolf number in May and June 1954 was lower than unity, indicating a very deep activity minimum. In some sense, the corona of this period provides an ideal minimum coronal structure. For this reason, there have been numerous studies of this corona, which is especially convenient for theoretical analyses as a classical example of simple coronal structure.

As a rule, epochs of solar minima are characterized by three zones of reversals of the polarity of the large-scale magnetic field [14], which indicates a dominant role of the first two odd harmonics of the expansion (1). On June 30, 1954, there were two separatrices of the magnetic field at $\pm 40^\circ$ and a third neutral line between them, with this line approaching 30° in both hemispheres [15]. The strong curvature of the third neutral line could indicate a significant contribution of odd harmonics in (1). Therefore, to construct the $B_r = 0$ surface, we will use both even and odd harmonics of the first four terms in expansion (1).

Figure 1a presents a structural schematic of the corona of June 30, 1954 [16], in which the main structural elements are helmets stretched along the solar equator at the east and west limbs. The locations of these helmets are fairly symmetric with respect to the solar axis, and their radial extent is $\approx 2.2\,R_\odot$. Such a size is possible if the ratio of coefficients of odd harmonics is $(a_3^\mu/a_1^\mu)^{1/2} \approx 2.2$. In addition, the directional angles of these harmonics θ_3^μ, $\theta_1^\mu \le 5^\circ$ are determined by the tilt of the helmet axes toward the equator and the symmetry of neutral lines at middle latitudes.

The splitting the apex of the west helmet structure (Fig. 1a) was provided by two odd harmonics of (1), with their directional angles close to the equatorial plane. We chose the pairs of parameters a_2^μ, θ_2^μ and a_4^μ, θ_4^μ by matching the splitting point of the west helmet with the observed point at $\approx 1.6R_\odot$. The final parameter selection for these even harmonics was based on obtaining the best agreement between the calculated and observed neutral lines [15].

Our selection of parameters in (1) shows that we can obtain satisfactory results taking into account only a single component of each harmonic (the case $\mu = 1$). Figure 1b shows the calculated $B_r = 0$ surface for the following parameters, which provide the best agreement with the observations:

$$a_1^1 = 1.0, \quad \theta_1^1 = \ 3^\circ, \quad \varphi_1^1 = 225^\circ, \quad (2)$$
$$a_2^1 = -0.02, \quad \theta_2^1 = 75^\circ, \quad \varphi_2^1 = 290^\circ,$$

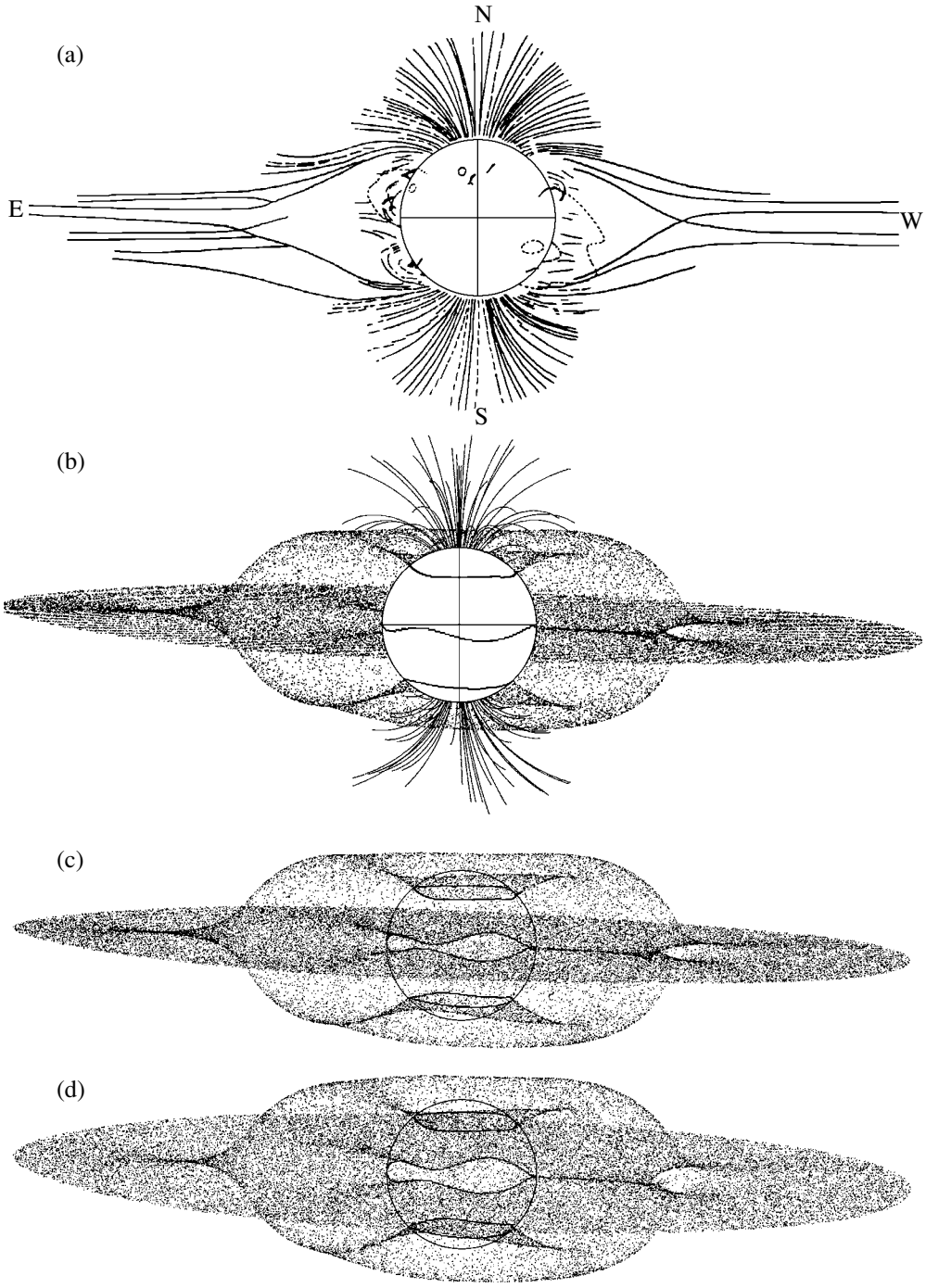

Fig. 1. Structural schematic of the corona of June 30, 1954: (a) the $B_r = 0$ surface, (b) magnetic field lines of polar regions, and a stereogram of the $B_r = 0$ surfaces with the angles between the line of sight and the solar rotational axis being (c) 87° and (d) 84°.

$$a_3^1 = 5.5, \quad \theta_3^1 = 5^\circ, \quad \varphi_3^1 = 205^\circ,$$
$$a_4^1 = -1.0, \quad \theta_4^1 = 80^\circ, \quad \varphi_4^1 = 200^\circ.$$

We assumed the longitude of the central meridian to be 180° and the inclination of the solar axis to be +2.8° at the moment of eclipse.

Figures 1c and 1d correspond to the $B_r = 0$ surface, with the angles between the solar rotational axis and the plane of the sky being 3° and 6°, respectively. These two figures form a stereo pair. Three curves on the sphere $r = R_\odot$ show boundaries between radial magnetic fields of opposite signs. A superposition of

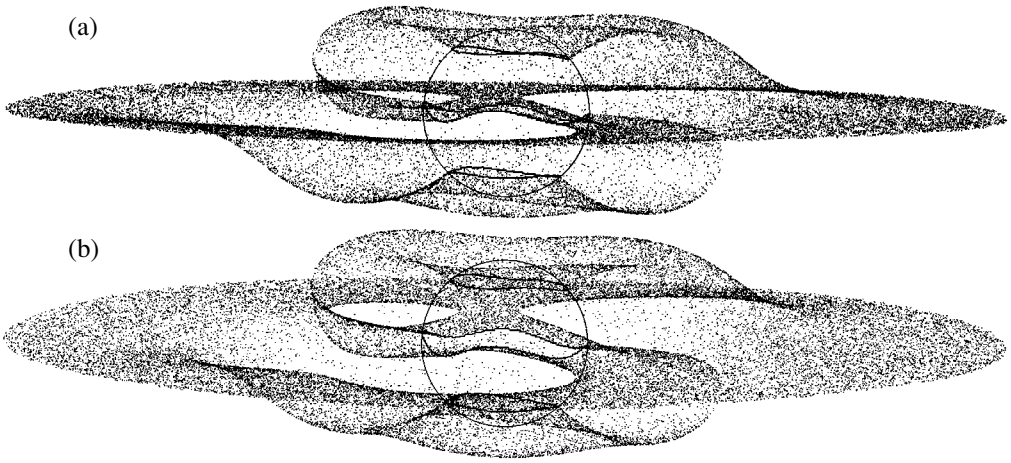

Fig. 2. The same surface ($B_r = 0$) as that in Fig. 1, but for another azimuthal angle (see text) and for an inclination of the axis from the line of sight by (a) 84° and (b) 80°.

Figs. 1c and 1d represents the helmet structures as Whitney gathers of the $B_r = 0$ surface. Note that such atmospheric structures were first identified with folds and Whitney gathers in [6, 17].

We can visualize the form of the $B_r = 0$ surface by examining its projections in various directions. Figure 2 is obtained when the line of sight is rotated by 110° in longitude. Figures 2a and 2b form a stereo pair for the two angles between the rotational axis and the plane of the sky 6° and 10°. Figure 2 provides a clear representation of the shape of the $B_r = 0$ surface. It cuts off two polar regions with outer lines of polarity reversals, and runs along the central line. When unfolded, this surface exhibits two cupolae. Such cupolae were first studied in [1] using observations obtained in 1941. They were named envelopes. During the eclipse of August 11, 1999, in his study of the inner and outer corona ($F = 3$ m and $d = 20$ cm, with radial filter), Koutchy observed structure of the same type near the northwest limb (Fig. 3).

Our computations show that the smooth $B_r = 0$ surface exhibits folds (and gathers) in some regions and projections, and cupola envelopes in others. In the configuration studied, various types of helmets originate from such folds. However, all remain within the scope of the classification first suggested in [1] (see also [18], describing two types of helmets). Figure 2 presents type-2 helmets, with sharp apices, while type-1 helmets, with broad apices made up of a pair of gathers, appear at other projection directions.

Note that we decided not to plot the usual coordinate lines on the three-dimensional image of the $B_r = 0$ surface, since they make the image cluttered and hide both the general structure and significant details of the surface. Plotting randomly spread points whose projections onto the plane of the sky differ by 3°–7° proved to be the best approach. Such angle differences are large enough to create stereo effects. We performed our calculations for distances $R_\odot \le r \le 6R_\odot$ and a uniform grid with steps of 0.2° in latitude, 0.1° in longitude, and $0.01R_\odot$ in radius.

Let us note two circumstances. The first is that, for the dense equilibrium plasma of the heliospheric layer, the condition $B_r = 0$ is necessary but not sufficient. The formation of a layer of dense plasma everywhere around the $B_r = 0$ surface is not guaranteed. At the same time, observations of quiescent filaments show that such a layer does form, at least at chromospheric densities and temperatures ($n \sim 10^{11}\, cm^{-3}$, $T = 10^4$ K). In our opinion, the results presented here reveal a similar situation for the corona ($n \sim 10^8\, cm^{-3}$, $T = 10^6$ K): virtually the entire $B_r = 0$ surface carries the heliospheric layer, and individual elements of the surface are observed as streamers, helmets, and envelopes. The second circumstance is that this surface is rather complicated even for a small number of spherical harmonics in the potential expansion ($n = 4$). Therefore, it is not meaningful to discuss the number of $B_r = 0$ surfaces: expression (1) immediately describes a certain class of structures, which must be compared with observations as a whole.

4. POLAR PLUMES

In models for equilibrium configurations of a plasma in magnetic and gravitational fields, there are at least two possibilities for the existence of fine plasma structures in the polar regions of the Sun. The first is an equilibrium for plasma carrying current along the original magnetic field lines of the polar regions; the second is a small-scale distortion of

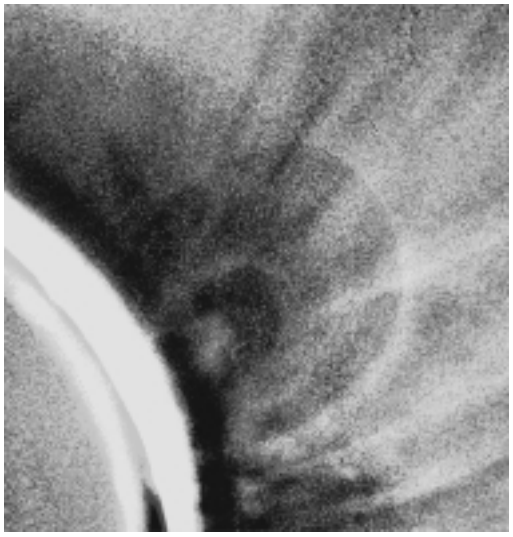

Fig. 3. The coronal structure of the type of envelope observed near the northwest limb during the eclipse of August 11, 1999.

the $B_r = 0$ surface, which initially has the form of a conical (funnel-shaped) surface.

Let us consider the first possibility for a simple model for the magnetic field. Let there be a magnetic field

$$\mathbf{B} = \{0, B_z(r), B_\varphi(r)\}, \quad \Phi = gz, \tag{3}$$

in a uniform gravitational field, where r, φ, z are cylindrical coordinates and Φ is the gravitational potential. In this reference frame, the force balance equation becomes [19]

$$\nabla\left(p + \frac{B_z^2}{8\pi}\right) + \frac{1}{4\pi}\left(\frac{B_\varphi}{r}\right)\nabla(rB_\varphi) + \rho\nabla\Phi = 0\,. \tag{4}$$

For the case of cylindrical symmetry, (3) yields

$$\mathrm{curl}\mathbf{B} = -\mathbf{e}_\varphi\frac{\partial B_z}{\partial r} + \frac{\mathbf{e}_z}{r}\frac{\partial}{\partial r}(rB_\varphi)\,,$$

and

$$-\frac{1}{4\pi}[\mathrm{curl}\mathbf{B}\mathbf{B}] = \frac{\mathbf{e}_r}{4\pi}\left(\frac{1}{r}B_\varphi\frac{\partial}{\partial r}(rB_\varphi) + B_z\frac{\partial B_z}{\partial r}\right).$$

Hence, there is only the $\mathbf{e}_r$ component of the magnetic pressure, which takes the form

$$\frac{\partial}{\partial r}\left(\frac{B_z^2}{8\pi} + \frac{1}{4\pi}\int\limits_\infty^r \frac{\left[(rB_\varphi)^2\right]'}{2}\frac{dr}{r^2}\right)\,.$$

We assume that

$$\Pi(r) = \frac{B_z^2}{8\pi} + \frac{1}{4\pi}\int B_\varphi(rB_\varphi)'\frac{dr}{r}. \tag{5}$$

We can use (5) as an integral transformation relating the density distribution in polar plumes to B_φ (or the J_z current). We denote the pressure component related to B_φ

$$f(r) = \frac{1}{4\pi}\int\limits_\infty^r B_\varphi(rB_\varphi)'\frac{dr}{r}. \tag{6}$$

We rewrite (6) in the form

$$B_\varphi = \left(\frac{2}{r^2}\int f'r^2dr\right)^{1/2}. \tag{7}$$

Expression (7) shows that every $f(r)$ corresponds to some distribution of B_φ (taking into account that $rB_\varphi = \frac{2}{c}J_z$ and $J_z = \int\limits_0^r j_z r dr$, an equilibrium current distribution can be constructed for any $f(r)$).

Let us restrict our consideration to a narrower problem. We construct an equilibrium configuration with total current $J_z(r)_{r\to\infty} = 0$. We assume

$$B_\varphi = \frac{bx}{(1+x^2)^2}, \quad x = \frac{r}{r_o}, \tag{8}$$

where b and r_o are the characteristic field and transverse scale of the plumes. The integral (6) can be written in the form

$$\int\limits_\infty^r \left[(B_\varphi r)^2\right]'\frac{dr}{r^2} = B_\varphi^2 + 2\int\limits_\infty^r \frac{B_\varphi^2}{r}dr. \tag{9}$$

Then (taking the additive constant to be zero), we find

$$\int\limits_\infty^r \frac{B_\varphi^2}{r}dr = b^2\int\limits_\infty^x \frac{x}{(1+x^2)^4}dx = -\frac{b^2}{6}\frac{1}{(1+x^2)^3}. \tag{10}$$

Thus, taking into account (9) and (10), we obtain for the integral (6):

$$\frac{1}{4\pi}\int\limits_\infty^r B_\varphi(rB_\varphi)'\frac{dr}{r} = \frac{b^2}{8\pi} \times \left\{\frac{x^2}{(1+x^2)^4} - \frac{1}{3}\frac{1}{(1+x^2)^3}\right\}. \tag{11}$$

The expression in curly braces in (11) is a function $f(r)$ that is equal to -0.33 at $x = 0$ and grows when $x > 0$; the minimum full width at half maximum is $\Delta x = 0.33$. The function $f(r)$ becomes zero at $x = 0.67$. It is natural to adopt this point as an average boundary of the polar plumes: $r_b/r_o = 0.67$. Assuming $r_b = 10^9$ cm, we obtain $r_o = 1.5 \times 10^9$ cm.

We can easily find the value of r where the current density j_z reverses. Assuming $\frac{d}{dr}(rB_\varphi) = 0$, we find $x = 1$; i.e., $r = r_o$. For $r > r_o$, the sign of j_z is opposite to the sign of the current flowing in the central region $0 \le r < r_o$. Note that the regions of constant

sign of the magnetic pressure $0 < r < r_b$ (6) and of the current j_z ($0 \le r < r_o$) do not coincide.

Finally, assuming that in the polar regions $n = 10^8$ cm^{-3}, $T = 10^6$ K, $nkT = 10^{-2}$, $B = 2$ G, and $\frac{B^2}{8\pi} = 16 \times 10^{-2}$, we obtain $\beta \ll 1$. This means that the magnetic pressure plays an important role in the distribution of the polar-plume material, including that portion of the pressure that is related to B_φ.

The above analysis of the force balance suggests that polar plumes are concentrations of dense plasma stretched along magnetic field lines. Figure 1b adds polar magnetic-field lines to the surface folds (and gathers) for the model of the corona of June 30, 1954. Our calculations use the flux function ψ (see Appendix). The number of magnetic-field lines on these surfaces corresponds to the distribution found in [20], with its maximum and boundary being at latitudes 75° and 60°, respectively.

5. CONCLUSIONS

Our computation of a simple coronal configuration corresponding to a minimum of solar activity has overall been successful. First, it provides a unified description for equilibrium plasma configurations. Second, it can describe the main structures of equatorial regions: two types of helmets and envelopes appear quite naturally.

The polar plumes represent equilibrium plasma configurations in the magnetic and gravitational fields. The magnetic field of the current flowing along the lines of force is responsible for the concentration of plasma near these lines. The current flowing at the center of an individual polar plume is compensated by the current flowing along its surface. Thus, the total current is zero. We have also shown that our model permits configurations with structures observed as relatively dark regions.

Finally, we note the following. One could use similar physical assumptions (equilibrium plasma in magnetic and gravitational fields) to model the shapes of prominences. However, we believe this problem would be hopelessly difficult, since the field sources are situated beneath the photosphere and the field structure is rather complicated in the vicinity of the photosphere. The situation is quite different in the corona: at solar minima, the field can be represented by a small number of spherical harmonics, as is demonstrated by a comparison of our model calculations with the structures observed.

6. ACKNOWLEDGMENTS

This work was supported by the Russian Foundation for Basic Research (project code 99-02-16360).

APPENDIX

1. A standard computation of the potential (or its normal derivative $B_r = -\dfrac{\partial U}{\partial r}$) from its values on a spherical boundary is based on calculating the coefficients (see, for example, [21]):

$$A_{nk} = \frac{(2n+1)(n-k)!}{2\pi(n+k)!} \times \int_0^{2\pi}\int_0^{\pi} f(\theta,\varphi) P_n^k(\cos\theta)\cos k\varphi \sin\theta d\theta d\varphi, \quad \text{(A1)}$$

$$B_{nk} = \frac{(2n+1)(n-k)!}{2\pi(n+k)!} \times \int_0^{2\pi}\int_0^{\pi} f(\theta,\varphi) P_n^k(\cos\theta)\sin k\varphi \sin\theta d\theta d\varphi,$$

$$A_{1o} = \frac{1}{4\pi}\int_0^{2\pi}\int_0^{\pi} f(\theta,\varphi)\sin\theta d\theta d\varphi,$$

where $f(\theta,\varphi)$ is the function prescribed on the boundary and P_n^k are the associated Legendre polynomials of degree n and order k, which are used to represent the potential and, consequently, its derivative B_r:

$$U(r,\theta,\varphi) = \sum_{n=1}^{\infty} \frac{R_\odot^{n+2}}{r^{n+1}(n+1)} Y_n(\theta,\varphi) \quad \text{(A2)}$$

$$= \sum_{n=1}^{\infty}\sum_{k=0}^{n} \frac{R_\odot^{n+2}}{r^{n+1}(n+1)} \times (A_{nk}\cos k\varphi + B_{nk}\sin k\varphi) P_n^k(\cos\theta),$$

$$B_r(r,\theta,\varphi) = \sum_{n=1}^{\infty} \frac{R_\odot^{n+2}}{r^{n+2}} Y_n(\theta,\varphi).$$

In our calculations, it is more convenient to use ordinary Legendre polynomials in a coordinate frame rotated by some angle with respect to the original frame.

The sum of terms

$$\frac{1}{r^{\nu+2}} a_\nu^\mu P_\nu(\cos\gamma_\nu^\mu) \quad \text{(A3)}$$

(where a_ν^μ are arbitrary coefficients, P_ν are Legendre polynomials, and $\cos\gamma_\nu^\mu = \cos\theta\cos\theta_\nu^\mu + \sin\theta\sin\theta_\nu^\mu \times cos\,(\varphi - \varphi_\nu^\mu)$) also represents the solution (A2). Indeed, according to the adding theorem

$$P_n(\cos\gamma_\nu^\mu) = P_n(\cos\theta)P_n(\cos\theta_\nu^\mu) \quad \text{(A4)}$$

$$+\ 2\sum_{m=1}^{n} \frac{(n-m)!}{(n+m)!} P_n^m(\cos\theta)P_n^m \times (\cos\theta_\nu^\mu)\,(\cos m\varphi\cos m\varphi_\nu^\mu + \sin m\varphi\sin m\varphi_\nu^\mu)\,.$$

Using the orthogonality of P_n^m, (A2) yields $\nu = n$, $m = k$. Then, assuming $R_\odot = 1$, we obtain the relationship between the coefficients (A1) and (A3):

$$\sum_\mu a_n^\mu \times 2\frac{(n-k)!}{(n+k)!}P_n^k(\cos\theta_n^\mu)\cos k\varphi_n^\mu = A_{nk}\,, \tag{A5}$$

and a similar relationship for the terms B_{nk} proportional to $\sin m\varphi$ [see (A4)].

Expression (A5) relates a_n^μ to A_{nk}, that is, the weights of harmonics of number n in the direction θ_n^μ, φ_n^μ to the ordinary spherical expansion coefficients for the function prescribed on the sphere $r = R_\odot$. In particular, (A5) shows that the number of coefficients a_n^μ (i.e., the number of directions θ_n^μ, φ_n^μ) is equal to the number of coefficients A_{no}, A_{nk}, and B_{nk} — $2n + 1$. We can use (A5) as a set of k equations for the coefficients a_n^μ.

2. The configurations studied here for a minimum corona are similar to axially symmetric structures. To describe axially symmetric fields, it is convenient to introduce functions of the poloidal ψ and, if necessary, toroidal χ fluxes. Here, since we assume $B_\varphi \equiv 0$, $\chi = 0$, and

$$\psi = A_\varphi r\sin\theta. \tag{A6}$$

In the potential approximation for the field, we obtain

$$\psi = \sum_{n=1}^{\infty}\frac{c_n}{r^n}(1-x^2)^{1/2}P_n^1(x), \tag{A7}$$

where c_n are arbitrary coefficients, $x = \cos\theta$, and P_n^1 are the associated Legendre polynomials. Here, the equation for magnetic surfaces takes the simple form

$$\psi = \text{const}. \tag{A8}$$

As noted above, polar plumes can represent plasma concentrations arising around local currents flowing along the lines of force of the total magnetic field of the Sun. The form of these lines of force must also be calculated, which, for the axially symmetric case, is done using (A7) and (A8). The parameters (2) of the expansion obtained for the corona of June 30, 1954 enable us to use (A8) due to the dominant role of the dipole and quadrupole components of the expansion (1) and the coincidence (2) of their axes. We have assumed here that the symmetry axis is inclined 4° from the solar axis, and determined the relationship between the coefficients a_n^1 in (2) and the c_n in (A7) based on the expressions for the radial component of the magnetic field (1) and the relation $B_r = -\dfrac{1}{r^2}\dfrac{\partial\psi}{\partial x}$.

REFERENCES

1. E. Ya. Bugoslavskaya, Tr. Gos. Astron. Inst., Mosk. Gos. Univ. **19**, 187 (1950).
2. M. M. Molodenskiĭ, L. I. Starkova, S. Koutchmy, and A. V. Ershov, Astron. Zh. **73**, 934 (1996) [Astron. Rep. **40**, 848 (1996)].
3. S. Koutchmy, M. M. Molodenskiĭ, L. I. Starkova, *et al.,* Pis'ma Astron. Zh. **23**, 939 (1997) [Astron. Lett. **23**, 818 (1997)].
4. S. Koutchmy, J. B. Zirker, R. S. Steinolfson, and J. D. Zhugzda, in *Solar Interior and Atmosphere,* Ed. by A. N. Cox, W. C. Livingston, and M. S. Matthews (Univ. of Arizona Press, Tucson, 1991), p. 1044.
5. S. Koutchmy, Astron. Astrophys. **13**, 79 (1971).
6. A. A. Vedenov, V. A. Koutvitsky, S. Koutchmy, *et al.,* Astron. Zh. **77**, 134 (2000) [Astron. Rep. **44**, 112 (2000)].
7. M. M. Molodensky, L. I. Starkova, S. Koutchmy, and A. V. Ershov, in *Solar Drivers of Interplanetary and Terrestrial Disturbances,* Ed. by K. S. Balasubramaniam, S. L. Keil, and R. N. Smart, Astron. Soc. Pac. Conf. Ser. **95**, 385 (1996).
8. S. Koutchmy, M. M. Molodenskiĭ, O. Matsuura, and E. Picazzio, Pis'ma Astron. Zh. **25**, 308 (1999) [Astron. Lett. **25**, 258 (1999)].
9. R. H. Levine and M. D. Altschuler, Sol. Phys. **36**, 345 (1974).
10. J. T. Hoeksema, J. M. Wilcox, and P. H. Scherrer, J. Geophys. Res. **87**, 10 331 (1982).
11. J. A. Linker, Z. Mikić, D. A. Biesecker, *et al.,* J. Geophys. Res. **104**, 9809 (1999).
12. T. L. Duvall, Jr., J. M. Wilcox, L. Svalgaard, *et al.,* Sol. Phys. **55**, 63 (1977).
13. V. I. Makarov and M. N. Stoyanova, Soln. Dannye, No. 11, 94 (1982).
14. V. I. Makarov and M. V. Kushnir, Soln. Dannye, No. 7, 64 (1987).
15. V. P. Mikhailutsa, Sol. Phys. **151**, 371 (1994).
16. S. K. Vsekhsvyatskiĭ and G. M. Nikol'skiĭ, Astron. Zh. **32**, 354 (1955).
17. J.-C. Vial and M. M. Molodenskiĭ, Astron. Zh. **70**, 1092 (1993) [Astron. Rep. **37**, 551 (1993)].
18. I. S. Shklovskiĭ, in *Physics of the Solar Corona* (Fizmatgiz, Moscow, 1962; Pergamon, Oxford, 1965), p. 20.
19. V. A. Kutvitskiĭ and L. S. Solov'ev, Pis'ma Astron. Zh. **21**, 51 (1995) [Astron. Lett. **21**, 46 (1995)].
20. K. Saito, Publ. Astron. Soc. Jpn. **17**, 1 (1965).
21. B. M. Budak, A. A. Samarskiĭ, and A. N. Tikhonov, in *Collection of Problems on Mathematical Physics* (Nauka, Moscow, 1980; Pergamon, Oxford, 1964), p. 423.

Translated by V. Badin